Study of Metal-Insulator Transition in Strongly Correlated Vanadium Dioxide Thin Films

---

A Dissertation presented to

the Graduate Faculty of the School of Arts and Sciences

University of Virginia

---

in Candidacy for the Degree of

Doctor of Philosophy (Department of Physics)

By

Salinporn Kittiwatanakul

August 2014

TABLE OF CONTENTS

ACKNOWLEDGEMENT

This dissertation is dedicated to my beloved grandpa who passed away last year.

The dissertation could have not been completed without the help from many people. First of all, I would like to thank Jiwei Lu and Stuart Wolf for giving me the opportunity to work in the lab, and also for the excellent guidance and mentoring throughout my graduate school. Next I would like to express my appreciation to all of my research group members, including Nam Dao, Hongxue Liu, Yonghang Pei, David Kirkwood, Melissa Commisso Dolph, Wei Chen, Wenbin Fan, Wenjin Yin, Ryan Comes, Yishen Cui, Mandy Gu, Yuhan Wang, Linqiang Luo, Tom Anuniwat, and Keren Freedy. I really appreciate those who have passed on knowledge, tips, and tricks, and also those who have helped me with day-to-day experiment, especially those who have helped pushing the buttons to rescue LANS whenever there was power outage. Thank you for creating such a great working environment, thank you for all the chats—research or non-research related—we had in the office, labs, and conference hotels. I am lucky to know them professionally and personally, they are truly great friends.

My appreciation also expands to many people in nanoSTAR, physics, and MSE, including Tonya Reynolds, Beth Beal, Jeff Fox, Tommy Eanes, David Glover, and many more. I am grateful to have such a great collaborators, such as Mengkun Liu, Elsa Abreu, and Jude Laverock, they have been very good colleagues and friends to me. Moreover, I am thankful for the scholarship program of Development and Promotion of Science and Technology Talents Project (DPST), Royal Government of Thailand scholarships, the

Physics Olympiad program, and the Promotion of Academic Olympiad and Development of Science Education Foundation under the patronage of Her Royal Highness Princess Galyani Vadhana Krom Luang Naradhiwas Rajanagarindra (POSN). Thank you all the professors who taught me and supported me throughout the program, even though my interest was ping pong and not so much physics back then. Without the scholarship, I would have studied in a Thai university and would have missed a big opportunity in meeting and knowing new people from many parts of the world who are pursuing their dream in the United States. Being here is not only for my academic goal but it is also an eye and mind opener. It is also a big part of who I am today.

All the support through Facebook from my friends at UVa, Cornell, high schools, elementary schools, and many others around the world really cheered me up during my tough time. Thank you Dr. Nammon who was like a sister, a role model and my very good inspiration in many things. Thank you my friends in the UVa Thai community for all the support and understanding, Kiad, X, Tuck, Top, and the other 20-ish members. In addition, I would like to thank Tom for all the supports and discussions to make me a better PhD candidate. I really appreciate all the help and support both physically and mentally, thank you for all the delicious food you cooked, they were great sources of energy for my writing and analyzing processes. Lastly, I would like to say thank you to my family, mom, dad, and my little sister Jern who has supported me throughout the path and let me choose my own future. I could not have finished the dissertation without love and support from all of you. THANK YOU!

ABSTRACT

Vanadium dioxide (VO_2) has attracted considerable interest during the past six decades because of a first order phase transition that occurs at 340 K, together with the possibility of modifying the transition temperature. This transition is accompanied by abrupt changes in the electrical conductivity, optical transmittance, and reflectance in the infrared region, which can be of benefit in many applications of sensing and switching. Utilizing the reactive bias target ion beam deposition (RBTIBD) growth technique, the growth and characterization of pure-VO_2 and doped-VO_2 thin films on various substrates was investigated.

The electronic and structural characterizations of vanadium dioxide thin films deposited under various growth conditions, i.e. substrate temperature and O_2 flow rate, were investigated. As the O_2 flow rate increased, the [010] lattice parameter for monoclinic VO_2 was reduced and coincidently distinctive changes in the metal-semiconductor transition (MST) and transport behaviors were observed despite the identical valence state of vanadium confirmed by X-ray absorption and photoemission spectroscopy. The effect of the oxygen partial pressure on the monoclinic structure and electronic structure of thin films, and consequently the MST is discussed.

The effect of macro-strain arising from substrate clamping on MST and transport anisotropy was investigated in epitaxial VO_2 films grown on various orientations of TiO_2 single crystal substrates. One remarkable result is that highly strained epitaxial thin films were rutile in the insulating state as well as in the metallic state. These highly strained films undergo an electronic phase transition without the concomitant Peierls transition. It also shows that a very large tensile strain along the *c*-axis of rutile VO_2 resulted in a phase transition temperature of ~ 433 K, much higher than those in previous reports. The conductivity mapping of thin films also reveal the origin of transport anisotropy arising from the strain from substrate clamping. Extremely large conductivity anisotropy was discovered on VO_2/TiO_2 (100) thin film.

RBTIBD was used to explore the chemical doping (Al^{3+} and Mn^{4+}) of VO_2 thin films deposited on *c*-plane sapphire. Two approaches of doping technique were employed. The lower bias pulse frequency results in better crystallinity, enhancing the resistive change and the sharpness of the MST, while the high frequency doping degrades film crystallinity and suppresses the MST. Both type of dopants were found to improve the MST, whereas the MST of films doped with Al^{3+} is more improved than those doped with Mn^{4+}. Doping with Mn^{4+} does not raise the transition temperature while doping with Al^{3+} slightly increases the transition temperature, as the Al concentration increases. Evidence of hole doping from Al^{3+} was also found in Hall effect for the first time.

FIGURE CAPTIONS

TABLE CAPTIONS

CHAPTER 1. Introduction

1.1 Motivation

Many transition metal oxides exhibit a metal-insulator transition (MIT) or a metal-semiconductor transition (MST), which are useful for ultrafast and ultra low power nanoelectronic sensors, electric and optical switches, and memory devices. However a critical issue yet to be overcome for wide applications is the transition temperature (T_{MST}) of those materials for use near room temperature, and there are only very few materials that have a transition temperature near or above 300 K, *i.e.* VO_2 (340K), NbO_2 (1080 K) [1], Ti_2O_3 (410 K), and V_2O_3 (150 K) [2]. Vanadium oxides have attracted considerable interest during the past six decades because of the phase transition that several of these oxides exhibit. In particular, the fact that vanadium dioxide (VO_2) exhibits a first order phase transition at 340 K [3], together with the possibility of modifying T_{MST}, makes this material attract the most interest among those transition metal oxides. The transition is accompanied by abrupt changes in the electrical conductivity, optical transmittance, and reflectance in the infrared region, which can be of benefit in many applications of sensing and switching. The advantages of the MST in VO_2 are very broad: the large changes in reflectance in different regions of spectra can be used in smart windows and shutters, and the sensitivity to small perturbations such as stress, heat, and light, can be used in temperature sensors and bolometers. Furthermore, the fast response and bi-stability near room temperature can be use in switches and phase change memory. VO_2 is also a potential candidate for “beyond CMOS” logic switches, due to its exceptional power handling with much lower power dissipation.

Recently a lot of attention has been focused on the properties of $VO_{2,}$ especially on the mechanism of its MST which is still not fully understood. In the past, researchers have debated whether the transition is driven by the lattice [4,5] (Peierls model) or by electron correlation effects [6,7] (Mott-Hubbard model). Most recently, it has been generally agreed that the mechanism of the MST in bulk VO_2 is considered to be a collaborative Mott-Peierls transition, however recent evidence described in this thesis demonstrates that there is an electronic transition in VO_2 under large strains.

Thanks to the improvements in the quality of VO_2 thin films, there has been a growing emphasis on exploring logic and memory device applications of this intriguing phenomenon. Recent efforts on a Mott field effect transistor (MottFET) have demonstrated that VO_2 can be employed as the channel in a MottFET, and the applied external gate voltage switches the channel resistance between the insulating OFF state and the metallic ON state [8-10]. There are still several challenges for these so-called “Mott devices” [11], among which is a concern over the repeatability/reproducibility of the Mott transition because the properties of these materials are sensitive to oxygen vacancy concentration, strain, and other factors. Understanding the role of defects and developing a suitable growth technique to maintain reproducibility is thus required to realize the potential applications of Mott oxides.

1.2 Objectives

It has been shown that pure VO_2 films exhibited very different transport behavior, depending on the strain/stress, the defects, and the oxygen stoichiometry, hence it is crucial to study the effects of the deposition conditions on the quality of the film and its

MST in order elucidate the effect of film strain, the defects on the MST. As mentioned previously, the tunability of the MST of VO_2 is very useful in many applications, it is critical to modulate the transition temperature of VO_2 via various means.

In this dissertation, the effect of strain on the MST is systematically explored via the substrate clamping effect and chemical doping of VO_2 thin films. I studied the crystal structure, electronic band structure, carrier density and mobility, strain effect, anisotropy, and chemical doping of VO_2 thin films, all of which present insight into the electronic and structural nature of the MST in VO_2 thin films, particularly those which are epitaxially strained.

The objectives of this thesis include:

(1) Developing reproducible high quality VO_2 thin films deposited on various substrates via a novel Reactive Bias Target Ion Beam Deposition (RBTIBD) technique;

(2) Investigating the effect of chemical doping and the doping techniques;

(3) Understanding the correlations between film strain, defects, and transport behavior in epitaxial VO_2 thin films.

1.3 Dissertation Outline

This dissertation is organized around three different key topics: growth conditions, strain, and dopants.

Chapter 2 provides a brief introduction to metal-semiconductor transition (MST), and the background information and the state-of-art of vanadium dioxide (VO_2) and properties of its thin films.

Chapter 3 describes the deposition technique and characterization methods used in this work.

Chapter 4 describes the effect of growth conditions, O_2 flow rate, and substrate temperature on the reproducibility of the MST of VO_2 thin films. The valence state is discussed. Furthermore, the effect of the oxygen partial pressure on the monoclinic structure and electronic structure of VO_2 – and consequently the MST – is observed.

Chapter 5 describes the effect of strain from substrate clamping via electrical transport anisotropy and film thickness. Majority carrier density and mobility are discussed, in addition to structural and transport characterization of this material.

Chapter 6 discusses the doping techniques and the resulting MST after doping with other transition metal elements such as Mn^{4+} and Al^{3+}. The characterization of its structural and transport properties as functions of the dopant type and concentration is also described.

Chapter 7 summarizes major results and discoveries, and also suggests future strategies for further study.

CHAPTER 2. Background

In this chapter, a brief introduction to vanadium dioxide (VO_2) is provided and its state-of-the-art of its properties due to its metal-semiconductor transition (MST) are mentioned. The background information for VO_2 describes its crystal structure and electronic band structure; the underlying mechanism driving the MST (Mott model vs. Peierls model) are also discussed. The chapter also provides an overview of the optical and electrical properties of VO_2 near the MST and the tunability of the MST. The effect of strain on the MST and on the phase diagram of VO_2 is also discussed with some examples for different types of VO_2 materials (thin films, single crystals, nano-beams, etc.). Lastly, the challenges to the growth of VO_2 thin films on different single crystals substrates are revealed.

2.1 Vanadium dioxide (VO_2)

Vanadium dioxide (VO_2) undergoes a first order metal-semiconductor transition (MST) just above room temperature at 340 K. [3] Below the transition temperature (T_{MST}), bulk VO_2 is a monoclinic semiconductor with a narrow band gap of 0.6-0.7 eV. [12] Above the T_{MST}, it is a metal with rutile or tetragonal structure.

2.1.1 Crystal structure

The metallic phase of VO_2 has a body centered tetragonal or rutile lattice with space group $P4_2/mnm$. The lattice parameters of rutile VO_2 are $a_r = b_r = 4.5546$ Å and c_r

= 2.8528 Å. The V^{4+} ions are approximately located at the center of the O^{2-} octhahedra, and the octahedra at the center and corner are rotated by 90° around the c_r axis.

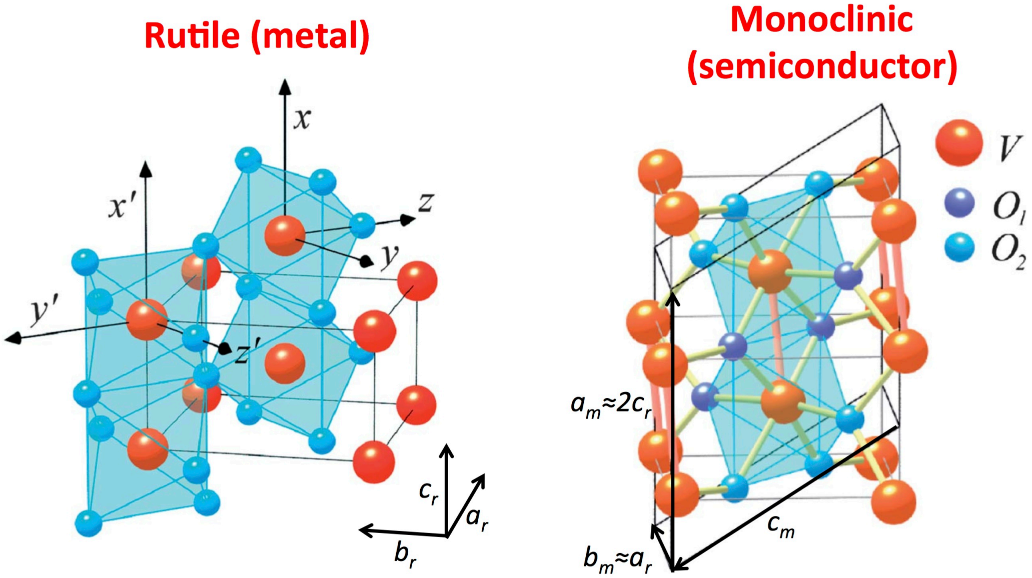

Figure 2.1 schematically shows the metallic tetragonal (rutile) structure and the semiconducting monoclinic structure of VO_2. [13]

The semiconducting phase has a monoclinic structure resulting from a distortion of the rutile structure with space group $P2_1/c$. Due to the distortion, V-V cations are created along the *a*-axis of monoclinic VO_2, where $a_m = 2c_r$. Instead of regular 2.85 Å V-V separation (c_t) in the rutile structure, the new structure V-V separations alternate between 2.62 and 3.16 Å. The lattice parameters of the VO_2 monoclinic unit cell are a_m = 5.7529 Å, b_m = 4.5378 Å, c_m = 5.3825 Å, and β = 122.6˚(the angle between a_m axis and c_m axis), respectively. [14]

2.1.2 Electronic band structure

The $3d^3s^2$ vanadium atoms have 4 electrons in the valence band, leaving one electron in the conduction band. In the metallic phase, as shown in figure 2.2 (left), the bands close to the Fermi level are the V3*d* bands, composed of a $d_{||}$ band oriented along the c_r axis, and by $3d_\pi$-hybridized bands, mixed with *p* orbitals of the O^{2-} atoms. In the semiconducting phase, in figure 2.2 (right), the $3d_{||}$band is split by the structural distortion (Peierls) and electronic correlations (Mott), while the $3d_\pi$ band is lifted above the Fermi level by the distortion of the V-O bonds. [15]

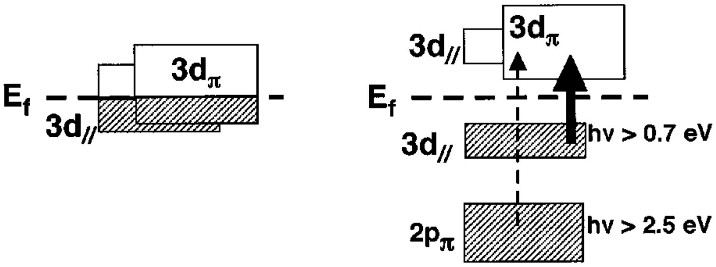

Figure 2.2 Schematic modification of the d-band structure of VO_2 on transition from metallic (left) to the semiconducting phase (right). [15]

The Goodenough model [16] can be used to describe the electronic structure of the two phases of VO_2. The deformation of the octahedral oxygen crystal field, resulting from the distortion of the V ions, causes the destabilization of the hybridized d_π band, raising the d_π band above the Fermi level. [17] In addition, this crystallographic distortion accompanies a doubling of the c_r axis to form the a_m axis, which results not only in the stabilization of $d_{||}$ bands but also in splitting the half-filled $d_{||}$into two separate bands. Finally, electron localization on the V-V pairs enhances Coulomb repulsion to approximately 2.0 eV [18], suggesting the important role of electronic correlations in the $d_{||}$ band splitting.

2.2 Introduction to the Metal-Semiconductor Transition (MST) in VO_2

Metal-semiconductor transitions (MST) are characterized by a change in the band structure, which is often accompanied by drastic changes in the electrical resistivity. The band structures of metals and semiconductors are shown in figure 2.3. In crystalline materials, the electron conductance in the band structure is described as follows: in a metal, one or more bands are only partially full, while in the non-metal material all bands are either full or empty. In metals, the Fermi level E_F lies inside one of the partially full bands. In semiconductors, the Fermi level is inside a band gap, which is small enough such that thermal or other excitations can bridge the gap, i.e. a small amount of doping can increase conductivity dramatically. The semiconductors can also be thermally populated with electrons or holes, thanks to relatively small band gaps.

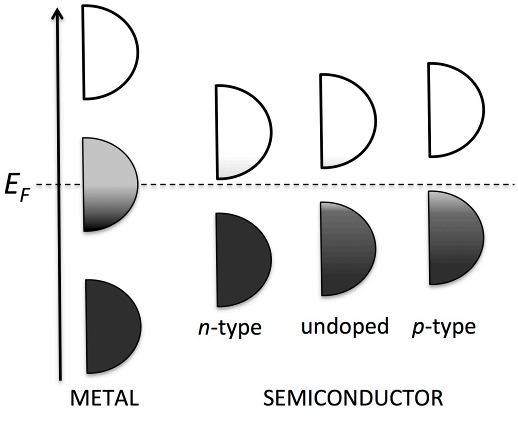

Figure 2.3 Band structure of metals and semiconductors showing doped and undoped types.

In the last decade, vanadium dioxide has become an exciting research area for both theoretical and experimental condensed matter physics and materials science due to its interesting metal-semiconductor transition which has proximity to room temperature. However, it was unclear whether the mechanism that drives the transition is driven by the lattice [4,5] (Peierls model) or by electron correlation effects [6,7] (Mott model); more recently, it has been generally agreed that the mechanism of the MST in bulk VO_2 is considered to be a collaborative Mott-Peierls transition [19], however it is still challenging identify the origin of this mechanism that drives the transition.

2.2.1 Driving mechanisms of the MST in VO_2

(a) Peierls model

An earlier attempt to explain the metal-semiconductor transition was approached by using a non-interacting electron model in order to understand the origin of band gaps in semiconductors. In the 1930s, Rudolf Peierls stated that a 1-D equally spaced chain of ions with one electron per ion is unstable [20,21]; hence the ion cores rearrange to make the distorted lattice more energetically favorable than the perfect crystal. The distortion will be energetically favorable when the energy saved from band gap opening is greater than the elastic energy used to rearrange the ions, which only occurs when the electrons are arranged close to the ground state; hence Peierls transitions should be seen at low temperature where the thermal excitation is minimized.

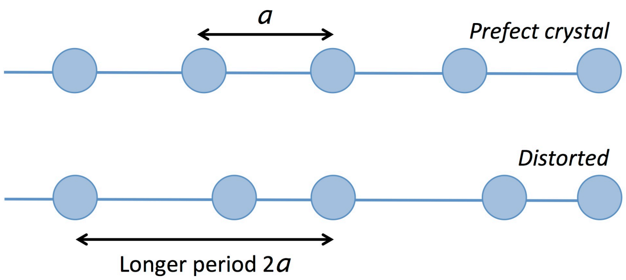

Figure 2.4 Distortion of the periodic lattice in 1-D crystal

The Peierls transition, sometimes called dimerization or Peierls distortion, is a distortion of the periodic lattice in a 1-D crystal where every other ion moves closer to one neighbor and further away from the other one as shown in figure 2.4. Using a simple model of the potential for an electron in a 1-D chain can explain how the distortion opens up a band gap, saving some energy.

To understand how a metal might turn in to semiconductor, the simplest model of 1-D conductor (perfectly arranged crystal) must be introduced:

$$H = H^0 + V = \frac{p^2}{2m} + V(x) \tag{2.1}$$

where H^0 is for non-interacting electrons on a line, and V is a periodic potential where $V(x+a) = V(x)$. [21] By applying Perturbation Theory, the periodic potential results in band gaps opening up at $|k| = \frac{\pi}{a}$, which means the lowest band for the model is from $k = -\frac{\pi}{a}$ to $\frac{\pi}{a}$. For monovalent atoms, electrons only half-fill the band, and this 1-D crystal would be metal.

As the crystal is distorted, the new period is *2a* instead of *a*, as shown in figure 2.4, introducing new band gaps at $|k| = \frac{\pi}{2a}$. For monovalent atoms, the electrons fill all the states to $|k| = \frac{\pi}{2a}$, and none beyond, making it semiconductor. This also means that all the electrons are in states whose energy is lowered.

However, the Peierls distortion model has failed to describe many behavior of VO_2. Hence Mott introduced a new model that considers electron correlation. [14,22]

(b) Mott model

A Mott transition originates from electron localization and the interplay of the Coulomb repulsion of interacting electrons. Consider a lattice model with a single electronic orbital on each site: without electron-electron interaction, a single band becomes full when two electrons occupy each site. However, two electrons sitting on the same site would feel a large Coulomb repulsion which would split the band in two: bonding (lower energy) and antibonding (higher energy). [22] The Hamiltonian shown in section (a) now requires an electron-electron Coulomb interaction term in addition to the lattice periodic potential *V(x)*. To understand the significance of strong correlation effects in band gaps opening, many theories and approaches have been made; one of the well known approaches is the Local-density approximation and its refinement. [23]

Mott argued that the transition would be abrupt; he considered a crystalline array of hydrogen-like atoms with lattice constant *a* that could be varied. He concluded that the transition would happen when free electron density *n* and the Bohr radius a_H satisfy

$$n^{1/3} a_H \simeq 0.2 \tag{2.2}$$

This formula was successfully applied to heavily doped semiconductors. [22]

The mechanism of the MST in VO_2 is described by Mott model, where the electron correlations are considered, as shown in figure 2.5, and described below:

(1) Due to electron correlation, the $d_{||}$ band split in two: bonding (lower) and antibonding (upper).

(2) As the d_{π} band shift up (the deformation of octahedral oxygen), the screening effect of $d_{||}$ electrons from d_{π} electrons is reduced.

(3) The reduced screening (electrons are harder to removed) will narrow the lower $d_{||}$ (bonding) band, increasing the gap between $d_{||}$ bands.

(4) Once the d_{π} band is completely lifted up above Fermi level (by deforming of octahedral oxygen), the lower $d_{||}$ is left below the Fermi level with narrow band, the insulating gap in VO_2 is determined to be (0.7 eV). Finally the electron localization on the V-V pairs enhances Coulomb repulsion, and lift the upper $d_{||}$ (antibonding) band to approximately 2.0 eV above the lower $d_{||}$ (bonding).

Since the deformation of octahedral oxygen is a result of V-V distortion, the MST in VO_2 single crystal is considered to be Mott-Peierls collaborative.

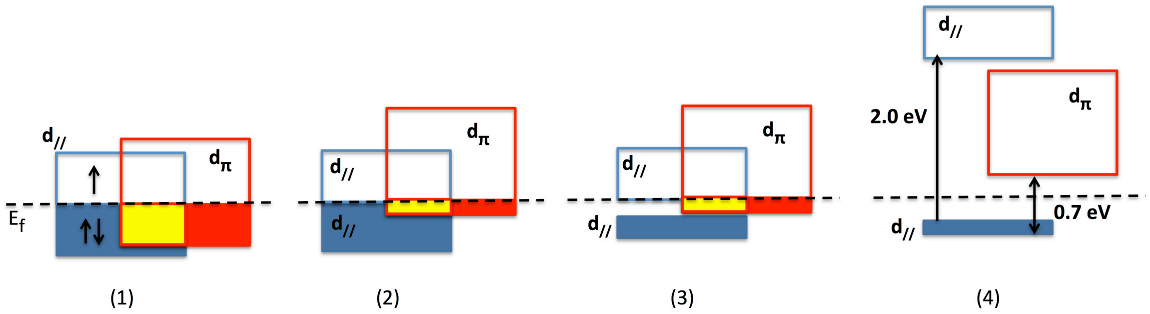

Figure 2.5 Band gap opening mechanism for Mott model.

(c) Identifying the origin of the mechanism of the MST

As mentioned in earlier sections, it is a big challenge to identify the true origin of the mechanism of the MST (Mott or Peierls), since as soon as one happens the other will follow spontaneously. Ultrafast response experiments with careful structure monitoring need to be performed in an attempt to distinguish the two. Both photoinduced and electrically induced experiments have become a big area of interest in the past decade. Recent experiments by Cavalleri *et al* [15] based on ultrafast spectroscopy and Raman spectroscopy provide evidence that atomic arrangement of the high-T tetragonal unit cell is needed for the formation of the metallic phase of VO_2 even if the correlated d band is highly hole doped. On the other hand, Kim *et al.* found evidence that the transition occurs in the monoclinic state and that the structural phase transition (SPT) to the rutile state occurs after; one of his experiments is based on Raman scattering during an electric field driven MST [24], and another is based on femtosecond pump probe and temperature dependent XRD measurements [25]. More recently the separation of MST and SPT was also confirmed by micrometer x-ray diffraction during an electric field driven MST, yielding the same results that VO_2 films show metallic conductivity while the tetragonal structure is absent. [26]

2.2.2 Properties of VO_2 near the MST and its modification

(a) MST in VO_2

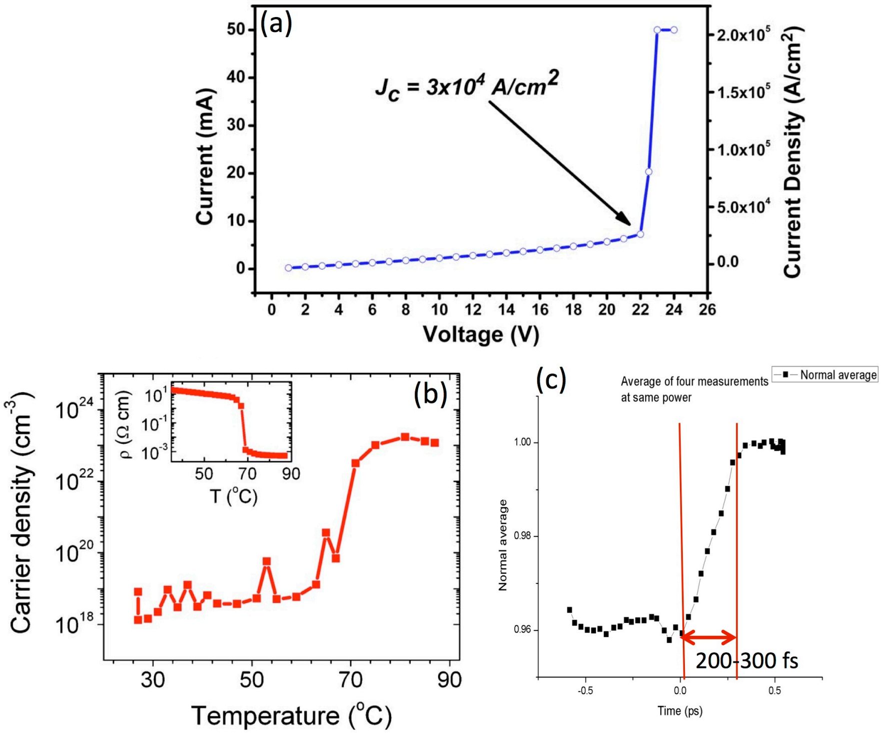

Figure 2.6 Examples of MST triggered by different sources: (a) electric field [27], (b) heat [28], (c) photoexcitataion (courtesy: R. A. Lukaszew).

Vanadium oxides have attracted considerable interest during the past five decades because of the phase transition that several of the oxides exhibit. [12,29] In particular, vanadium dioxide (VO_2) exhibits a metal semiconductor transition (MST) at 340 K. [3] This transition is accompanied by the abrupt change in the electrical conductivity, optical transmittance, and reflectance in the infrared region, as shown in figure 2.6-2.8. The conductivity change during the transition can be as large as 4-5 orders of magnitude in bulk VO_2. These properties of VO_2 can be used in advanced ultra fast and low power electronic devices such as sensors, switches, and memory devices. [30-32] The MST can also be triggered by different sources, i.e. heat, current/carrier injection, and photoexcitation as shown in figure 2.6. The transition induced by photoexcitation shows a very short switching time ~ 200 fs [33]. The time-resolved photo response in figure 2.6 also confirms the super fast switching behavior. Figure 2.7 shows the electrically induced transition of VO_2 devices, revealing robust and ultra-fast switching with a switching time τ ~ 2 ns [34]. The critical values to trigger the MST are summarized in table 2.1. In this dissertation, the work presented will focus on the thermally induced phase transition.

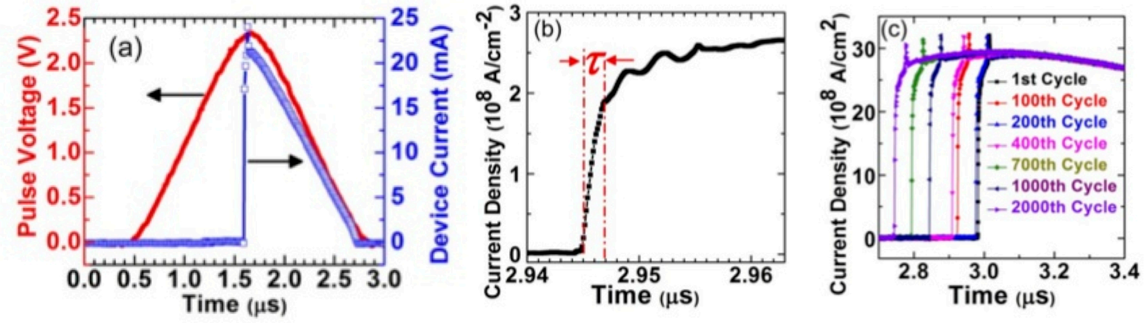

Figure 2.7 Time-resolved electric field induced transition of VO_2 device, (a) showing bias voltage and observed device current, (b) a zoom-in of time-resolved device current density, (c) repeated transition up to 2000th cycle. [34]

Table 2.1 Critical values for the transition to occur [3,24,27,33]

Triggered by	Critical value
Current injection	> 10^4 A/cm^2
Photoexcitation	> 250 μJ/cm^2
Heat	> 340 K

(b) Effect of various types of strain on VO_2 phase diagram and MST

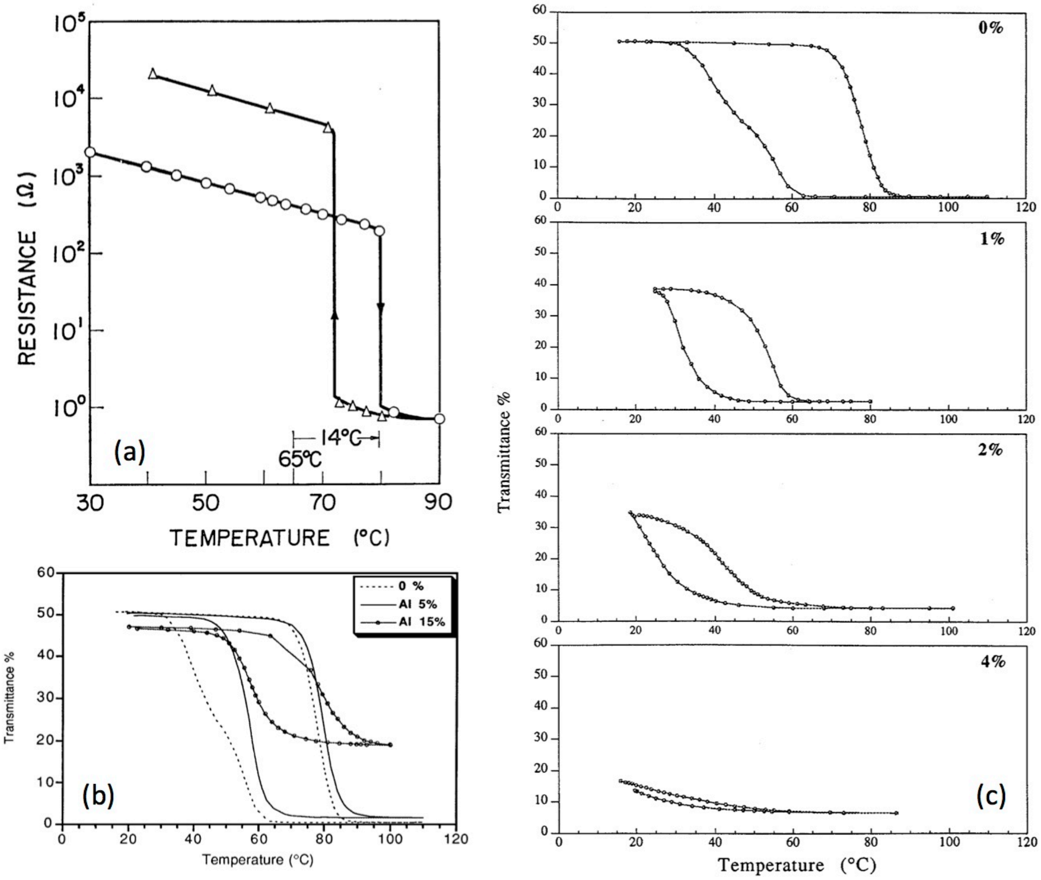

Figure 2.8 (a) Resistance as a function of temperature of VO_2 compared to 2.2% Ga doped VO_2 [35], (b) optical switching and hysteresis loop of VO_2 thin films doped with low-valent cations Al^{3+} , and (c) with high-valent cations W^{6+} [36].

Another factor that makes VO_2 more interesting, as mentioned previously, is the tunability of both its transition temperature and the magnitude of its resistivity ratio. It is crucial to understand the physics and mechanism of the transition to improve the ability to modulate the properties of this material, making it suitable for a wide range of applications. In the past, there have been many attempts to understand the collaborative transition model via applied strain and chemical doping that also reveal a modified transition of VO_2. It is found that the transition temperature decreases when the film is doped with high-valent cations such as Ti^{4+}, Re^{4+}, Ir^{4+}, Os^{4+}, Ru^{4+}, Nb^{5+}, Ta^{5+}, Mo^{6+}, and W^{6+}, and increases when doped with low-valent cations, *i.e.* Al^{3+}, Cr^{3+}, Fe^{3+}, Ga^{3+}, and Ge^{4+} [18,36]. However, as the transition temperature is shifted away from the bulk value (340 K), the transition gets suppressed, i.e. the ON/OFF ratio is reduced as shown in figure 2.8. To fully utilize the benefit of the tunability of this material, preserving the ON/OFF ratio or even enhancing the ratio is required.

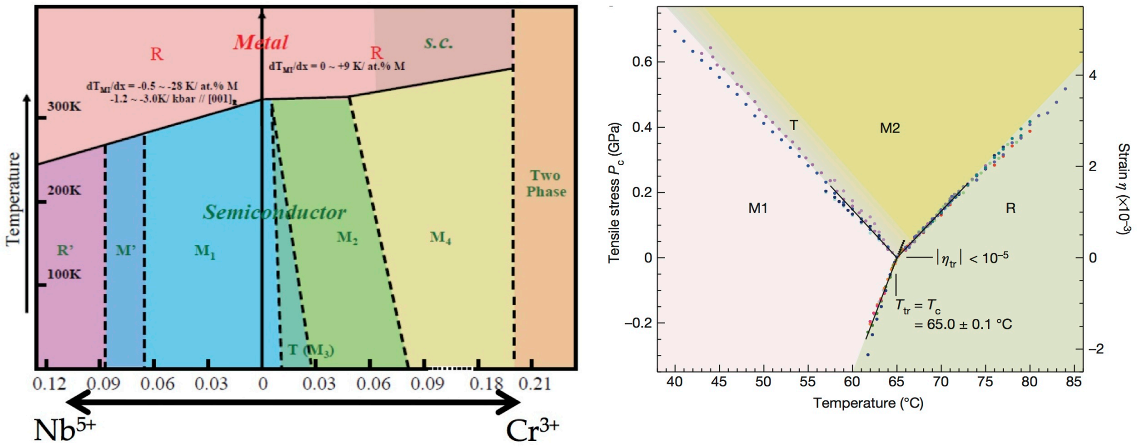

Figure 2.9 (Left) phase diagram of VO_2 for different concentration of dopants; doping ($V_{1x} M_x O_2$) leading to reduction ($M = Nb^{5+}$) or oxidation ($M = Cr^{3+}$) of V^{4+} is specified on the horizontal axis. Courtesy: M. Liu. (Right) deduced stress-temperature phase diagram of free-standing VO_2 nanobeams under uniaxial strain [37].

It has been generally agreed that the mechanism of the MST in bulk VO_2 is considered to be a collaborative Mott-Peierls transition, however the effect of strain on the phase transition is much more complicated. Various types of strains such as:

(1) macro-strains (mechanical strains, epitaxial strains etc.) and

(2) micro-strains (chemical substitutions, point defects in the lattice)

have been exploited to modify the phase transition. Recently, reports revealed that single crystal VO_2 nanobeams under uniaxial strain exhibited a complex blend of insulating phases including the *M1*, *M2* and triclinic (*T*) phases near the MST as shown in figure 2.9 (right). [37,38] Similarly, the micro-strain in the lattice induced by the chemical doping with Al also resulted in the meta-stable *M2* phase in free-standing VO_2 films near room temperature. [39] Figure 2.9 (left) shows a complex phase diagram of VO_2 for different concentrations of doping elements, where M_1 is the most distorted from the rutile structure.

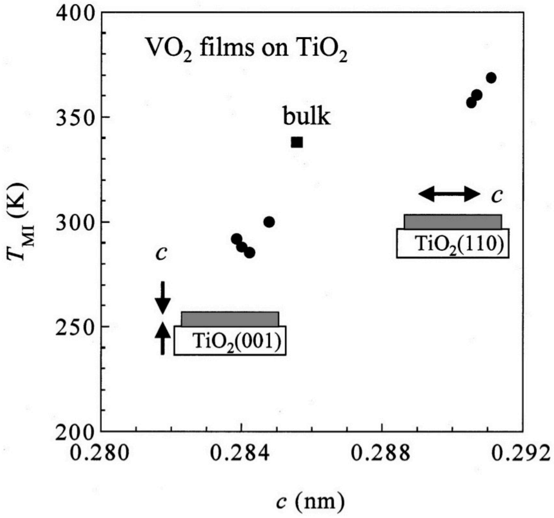

Figure 2.10 Transition temperature vs. lattice parameter *c* of VO_2 films deposited on TiO_2 (001) and TiO_2 (110) substrates. [40]

In contrast, epitaxial strain in thin film VO_2 arising from the crystal clamping with the substrate revealed quite a different picture of the phase transition. Despite the large lattice mismatch (~3.7 %) along the *c*-axis between the rutile TiO_2 and the VO_2 film, the experimental results by Muraoka *et al.* [40] showed a strong correlation between the transition temperature (T_{MST}) and the uniaxial strain along the *c*-axis of VO_2 (as shown in figure 2.10), and the correlation was opposite to that predicted by the Peierls (structural) mechanism. [41] Laverock *et al.* [42] have observed a Mott-like transition with a large tensile strain along the c_R axis in VO_2 using soft x-ray spectroscopy, demonstrating the absence of the large structural distortion near the phase transition which was previously observed in bulk and moderately strained VO_2. Epitaxial films under bi-axial strain also demonstrated a very pronounced anisotropy in optical and transport properties [43,44] as a result of the formation of unidirectional stripe states in which the semiconducting and metallic states coexisted. [45]

2.3 Growth of VO_2 thin film

2.3.1 Challenges of pure phase VO_2 thin film synthesis

The various benefits of VO_2 make this material very interesting; however the challenge in the past has been that the synthesis of this material is quite an obstacle. Due to the lack of advanced synthesis techniques, there was a big gap in the study of VO_2 since this material was first explored by Morin in the late 1950s [2]. There was a 20-30 year slow period where there were very few studies on this material, however, the topic became popular again in 1990s. The growth and the physical properties of vanadium dioxide thin films have been explored by various deposition techniques such as electron beam evaporation [46-48], re-active sputtering [48-53], sol-gel processes [54,55], chemical vapor deposition (CVD) [55], atomic layer deposition (ALD) [56], pulsed laser ablation [57,58], etc. Nonetheless, high purity VO_2 thin films were still hard to synthesize, since it is hard to prevent the formation of other vanadium oxides that would generally produce a mixed phase.

The valence state of vanadium ranges from V^{2+} to V^{5+}, hence single valence oxides (VO, V_2O_3, VO_2, V_2O_5) and mixed valence oxides (V_6O_{13}, V_3O_7, V_5O_9, etc.) can be easily formed by inducing oxygen defects. For example, a mixture of V^{3+} and V^{4+} forms a number of Magneli phases [59] which have the general formula V_nO_{2n-1}, where a mixture of V^{4+} and V^{5+} forms a number of Wadsley phases ($V_{2n}O_{5n-2}$) [60]. A number of these undergo the MST transition. These transitions are listed in table 2.2.

Table 2.2 Different vanadium oxides with the valence state of vanadium and the T_{MST} [59].

Material	Valence state of vanadium	T_{MST}
VO	2+	Metallic
V_2O_3	3+	168 K
V_3O_5	3+ and 4+	430 K
V_4O_7	3+ and 4+	250 K
V_5O_9	3+ and 4+	135 K
V_6O_{11}	3+ and 4+	170 K
V_7O_{13}	3+ and 4+	Metallic
V_8O_{15}	3+ and 4+	70 K
VO_2	4+	340 K
V_6O_{13}	4+ and 5+	145 K
V_3O_7	4+ and 5+	---
V_2O_5	5+	---

Growth conditions such as O_2 flow rate, substrate temperature, and process pressure can highly influence the phase and structure of the film. In the work presented here, reactive bias target ion beam deposition (RBTIBD) which will be described in chapter 3, was used to synthesize thin films on various substrates, where the effect of the deposition conditions on film quality will be discussed in chapter 4.

2.3.2 Epitaxy of VO_2 thin films on single crystal substrates

The substrates used in the study for this dissertation are single crystal substrates, which include *c*-plane Al_2O_3, (100) TiO_2, (001) TiO_2, and (011) TiO_2. The following information will give a brief review of the substrate crystal structures and an overview of the thin film crystal orientations deposited on these substrates.

(a) Aluminum oxide (Al_2O_3)

Sapphire or single crystal Al_2O_3 has a rhombohedral/hexagonal crystal structure that belongs to the space group of $R\overline{3}c$. The lattice parameters of the Al_2O_3 hexagonal unit cell are a = 4.758 Å and c = 12.992 Å. Due to the complex honeycomb-like crystal structure, there are many possible crystal orientation planes as shown in figure 2.11(a). In the study presented, *c*-plane sapphire (0006) substrates were used.

Due to different crystal structures of VO_2 and the hexagonal *c*-plane Al_2O_3 (later designated as as *c*-Al_2O_3), the VO_2 thin films deposited on *c*-Al_2O_3 have a monoclinic structure with three preferred in-plane orientations (rotated 120° from each other). The top-view crystal relationship of VO_2 and *c*-Al_2O_3 is shown in the bottom right of figure 2.11(a). The in-plane lattice spacing of bulk VO_2 is larger than that of Al_2O_3, hence an in-plane compressive strain is introduced for the films deposited on the *c*-Al_2O_3 substrate.

For the out-of-plane direction (perpendicular to the surface of substrate), XRD shows strong (020) *M*-VO_2 peak coupling to the (0006) Al_2O_3 peak (figure 2.11(a) top left), indicating oriented film growth along the [010] direction. The in-plane ϕ scans from 0° to 360° were performed on (110) *M*-VO_2 (monoclinic VO_2) and (2204) Al_2O_3, by fixing the tilt angle (ψ) and 2θ to the selected crystal planes. Each of the three preferred in-plane orientations of VO_2 gives 2 peaks in the in-plane ϕ scan due to symmetrically equivalent twin variants, yielding 6 peaks total; while Al_2O_3 gives three peaks due to the hexagonal symmetry (figure 2.11(a) bottom left). These crystal variants are single domain (010) *M*-VO_2 rotated 120° from each other, with pronounced twinning, which agree with a previous report [3]. The VO_2 thin films deposited on *c*-Al_2O_3 are single-crystal like in the out-of-plane direction, while in the in-plane direction (parallel to substrate surface), they are polycrystalline with three preferred orientations. This type of film growth is highly textured.

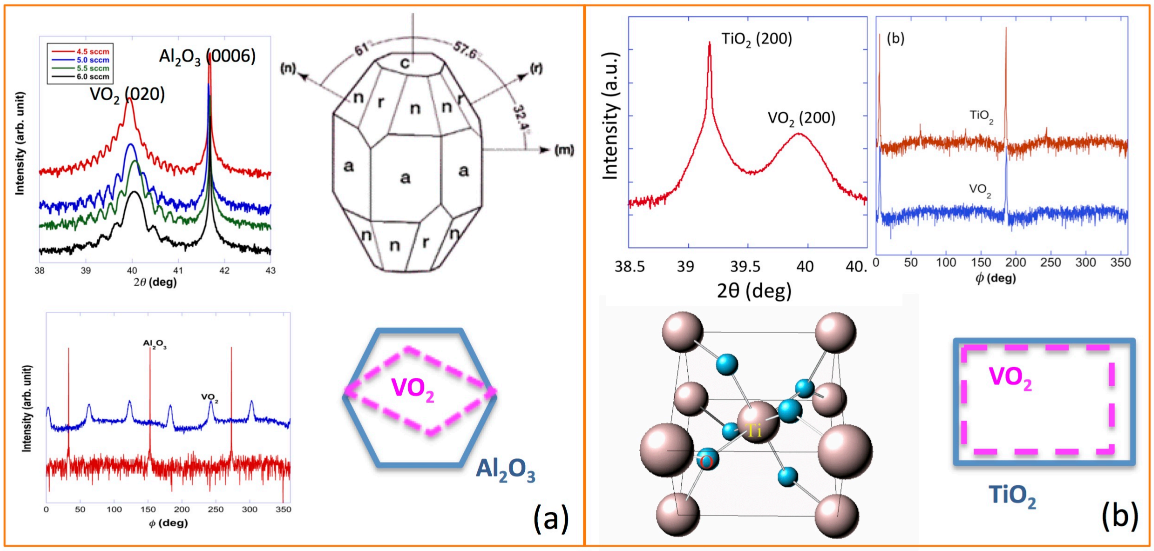

Figure 2.11 Crystal structure of single crystal substrates; and the examples of out-of-plane and in-plane XRD scans of VO_2 thin films deposited on various substrates: (a) Al_2O_3, (b) TiO_2

(b) Titanium dioxide (TiO_2)

The single crystal TiO_2 substrate used in the work presented here is rutile phase with the tetragonal space group $P4_2/mnm$ similar to that of *R*-VO_2 (rutile VO_2), where all the lattice parameters are listed in table 2.3. Due to the similar crystal structure as shown in figure 2.11(b), the VO_2 thin films deposited on TiO_2 substrates are clamped to the rutile structure: this effect is called “substrate-clamping effect”. Because of the similar structure, the VO_2 thin films are epitaxially grown on the TiO_2 as has been confirmed by in-plane azimuthal (ϕ) scans. Figure 2.11(b) top right shows the ϕ scan showing VO_2 and TiO_2 peaks for the (101) plane, which confirms the epitaxial growth of VO_2 thin films with a rutile crystal structure. Figure 2.11(b) top left is an example of the out-of-plane 2θ scans of VO_2 thin films deposited on (100) TiO_2. It shows the (200) peak of R-VO_2 coupling to the (200) peak of the TiO_2 substrate.

Table 2.3 Lattice parameters, in-plane spacing, and critical thickness of VO_2, TiO_2 (Å)

Material	***a***	***c***	***d_{011}***	***d_{110}***
R-VO_2	4.5546	2.8528	2.4177	3.2206
TiO_2	4.5936	2.9582	2.4871	3.2482
Mismatch (%)	0.86	3.69	2.87	0.86
H_c	2.6595	0.3861	0.4211	1.8806

The lattice parameters of bulk VO_2 are smaller than those of the TiO_2 substrate, hence this introduces an in-plane tensile strain due to this lattice mismatch as summarized in table 2.3. The lattice mismatch is calculated by the formula below:

$$latiice\ mismatch = \frac{d_s - d_f}{d_f} \tag{2.3}$$

where d_s is the lattice spacing of the substrate, and d_f is the lattice spacing (along the same direction) of the film. Based on the lattice mismatch, I have calculated the critical thickness (H_c) for VO_2 grown on various orientations of rutile TiO_2; using the energy minimization considerations [61,62], the critical thickness is reduced to a simple approximation expression:

$$H_c \cong \frac{a}{2f} \tag{2.4}$$

where a is the in-plane lattice parameter, and f is the in-plane lattice mismatch for each orientation of the TiO_2 substrates. Below the critical thickness, the epitaxial film is fully strained, thanks to the mismatch. Once the thickness exceeds the critical thickness, the misfit dislocations form spontaneously to relax the epitaxial strain. Hence the strain of the film shows a strong dependence on the film thickness.

CHAPTER 3. Experiments

This chapter introduces the main techniques used for the synthesis and characterization of VO_2 thin films. A novel deposition method called reactive bias target ion beam deposition (RBTIBD) is employed, and its characteristics are described. High-resolution x-ray diffraction (HRXRD) was used to study the crystal structure of VO_2: to determine the phase composition, and lattice parameters of thin films, and also to determine the epitaxial relationship between the film and the substrate. The thickness of the film was determined by x-ray reflectivity (XRR), and the roughness and the surface morphology were studied via Atomic Force Microscopy (AFM). The crystal structure of VO_2 thin films was also studied via temperature-dependent XRD and Raman spectroscopy. The valence state of VO_2 thin films was determined by soft X-ray spectroscopy through a collaboration with Kevin Smith’s group at Boston University. The transport behaviors are studied on two types of devices which are fabricated via photolithography.

3.1 Growth technique and deposition conditions

3.1.1 Reactive bias target ion beam deposition (RBTIBD)

Reactive bias target ion beam deposition (RBTIBD), a hybrid of ion beam deposition (IBD) and sputtering, was developed to address the limitations of IBD in the fabrication of sharp interfaces in multilayer structures for both metallic and oxide materials. [27,63,64] The schematic of the RBTIBD system is illustrated in figure 3.1. The RBTIBD system uses a low energy ion source that consists of a hollow cathode electron source (HCES) and an end-Hall ion source as an anode. The HCES emits electrons which then flow toward the anode (end-Hall ion source) and interact with the magnetic field near the anode causing ionization of the inert gas. The ionized gas is then accelerated using a separate voltage source. [65,66] Both the HCES and the ion source are each powered by a supply with a voltage range 0-100V and 0-12A that can produce a flux of low energy ionized inert gas (~5-50eV), but these ions do not have enough energy to sputter the target or any of the other construction materials inside the chamber such as chamber walls and target shielding. There are three gas lines connected into the chamber: two Ar gas lines, one through the cathode and another through the anode, and the third line provides a reactive gas (Ar/O_2 80/20 mixture) through the anode. All the gas mixtures used in the processing are ultra high purity (UHP) with 99.999% purity. The flow rates of all three lines are controlled by digital mass flow controllers (MFC). The flow ranges for the cathode Ar line and anode reactive gas line are 0-20 sccm, while the range for the anode Ar line is 0-100 sccm.

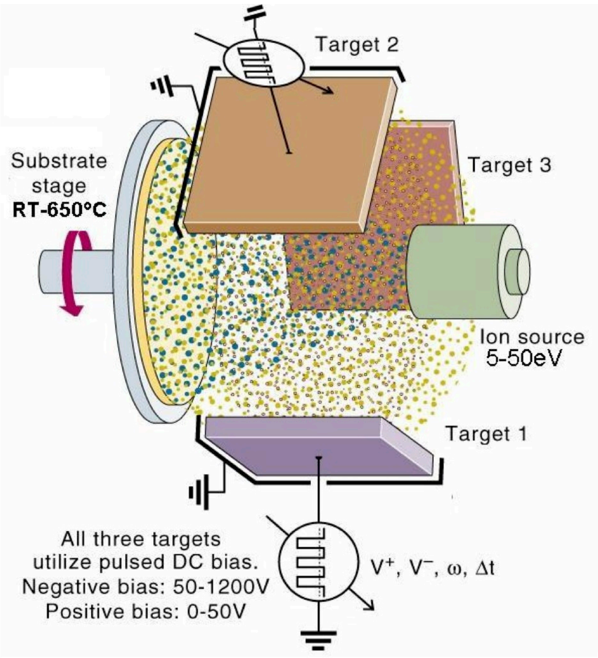

Figure 3.1 Schematic of the RBTIBD system

There are six 4-inch diameter metallic targets installed in the system. A Y-shaped target shutter covers three of the targets leaving the other three exposed at one time. The targets are positioned in a way such that they are parallel to the ion beam flux. All the targets are 99.99% pure metals, and are water-cooled during a deposition through a copper backing plate. The power supply for the negative bias has a range of 2kV and 1A, while the positive bias has a range of 60V and 5A. The frequency generator has a range of 1-75 kHz, while the positive pulse period is limited by 1/f.

The target bias is applied by a pulsed dc voltage source which alternates between a large negative bias and a small positive bias at a controlled frequency and pulse period. There are three pulse sources and three frequency generators, each connected to two targets such that one to three targets can be pulsed by dc bias at the same time at a separate frequency and pulse period, which is very beneficial when co-sputtering materials from separate targets.

Sputtering occurs only during the negative bias pulse period (1/f-positive pulse period), but not during the positive pulse period or zero bias. The large potential difference between the positively charged ions and the negatively charged target surface causes the ions to accelerate toward the target surface, creating a thin plasma sheath (~2 mm) and induces sputtering of the target material. Ar ions are inert and do not react with the target material, however, using O_2 which is reactive will cause an insulating dielectric to build-up on the target surface. This would lead to target poisoning, and reduce the sputtering yield drastically. By applying a small positive bias (~20 V), any dielectric material buildup on the target surface is effectively removed (discharged) by repulsive potential forces. During co-sputtering (doping), modulation of the positive pulse period at a low fixed frequency appears to yield better film qualities, in comparison with varying the pulse frequency for a fixed pulse period.

The substrate stage is vertically positioned and aligned with the ion source, rotating about that axis during the deposition for uniformity. The wafer carrier is made from tantalum (Ta), which has a high melting temperature, low thermal expansion coefficient, and non-ferrous properties. The Ta wafer carrier is 3 mm thick and has a 4-inch diameter. Ta pressure clamps and 0-80 Ti screws were used to mount single crystal substrates. Silver (Ag) paint was once used to mount the substrates but was found to be inefficient for film growth due to a non-uniform thermal gradient caused by non-uniform Ag particles in the solution. The resulting film surface was very rough and the film was not as highly crystalline as when the substrate is clipped. An infrared heating lamp is used to heat the wafer carrier. The thermal output of the heater is directly controlled by a variable voltage input, which is controlled by a digital to analog converter (DAC); the DAC value (ranging from 0-35000) is acquired at the software interface. Using a standard k-type thermocouple, the direct measurement of the surface temperature of the wafer carrier is calibrated every several months to DAC values used to control the input voltage; the temperature control range is 75 – 650 °C. The example of DAC calibration result is shown in figure 3.2.

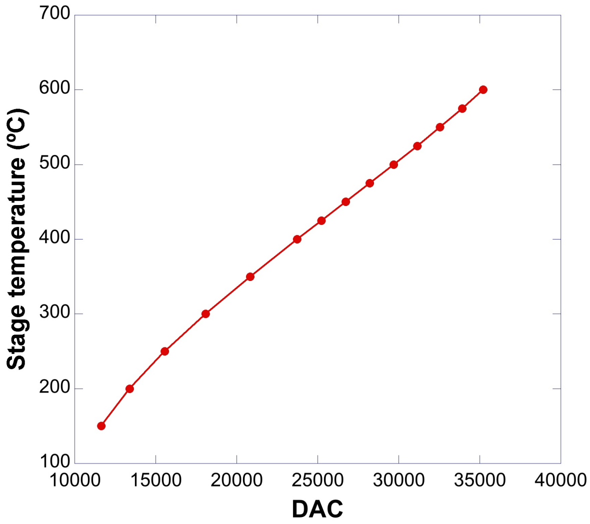

Figure 3.2 An example of DAC calibration for stage heater, using a standard k-type thermocouple.

The base pressure of the main chamber is ~2×10^{-8} Torr, obtained using a cryogenic pump. With a load lock mechanism, samples can be extracted and mounted without breaking the high vacuum in the main processing chamber. A mechanical rough pump is used to pump down the load lock chamber to 70-90 mTorr before opening the gate valve which connects the load lock to the main chamber.

3.1.2 Deposition process and key parameters

The procedure for cleaning the single crystal substrates includes an ultrasonic acetone bath followed by rinsing in isopropanol alcohol, drying with UHP N_2, and baking at 100 °C for 2 minutes. It is found that the substrate treatment is unnecessary if the substrate is directly out of the manufacturer's packaging and hasn't been cut or diced, since any tiny amount of chemical residue will result in contamination and very rough film surfaces. The substrates are then mounted on the wafer carrier using Ta clips and screws, then the wafer carrier is mounted on the stage in the load lock which is pumped down to 70-90 mTorr using a mechanical rough pump, and the gate valve then opens to the main chamber. The stage is then loaded into the main chamber which is pumped down until a base pressure of ~5 - 8 × 10^{-8} Torr is reached.

Once the desired base pressure is reached, the HCES is purged with 10 sccm Ar while the anode is purged with 50 sccm of Ar for 30 minutes. This is followed by a 30 minute degas procedure whereby the tungsten filament inside the HCES is heated up, outgassing contamination on its surface. At the same time that the degas process starts, the stage heater is ramped up to a calibrated DAC value corresponding to the desired substrate temperature (typically 450-550 °C) at a rate of 5000 DAC/minute to prevent abrupt jump in the voltage input. It takes about 45 minute for the wafer carrier to reach a stable surface temperature. After the degas process is complete, the ion source is turned on. Ar gas flowing through the anode is increased to 70 sccm. A voltage limit of 50 V and a current set point of 7.0 A are set for the cathode and after the cathode ignites the plasma, the anode voltage limit and current are set to 60 V and 6.5 A. The ion source is then stabilized within 5 minutes when the voltage on cathode and anode are about 4 V and 35 V respectively; this produces a beam current of 40 eV which is not enough to induce sputtering. The substrate is then pre-cleaned using the Ar ions by opening the stage shutter for 3 minutes with the stage rotating at 10 rpm.

To initiate the sputtering, the desired target's pulse frequency is set at 71.43 kHz with a 3 μs positive pulse period, while pulsed dc bias is applied with 900 V negative bias and 20 V positive bias. A plasma sheath forms at the target surface and sputtering is induced. The targets are first sputter-cleaned for 3 minutes; then the reactive gas, an

Ar/O_2 80/20 mixture, is introduced with the flow rate set to a desired value (typically 5.0-6.0 sccm). Using too much or too little oxygen can introduce other phases of vanadium oxides [27]. All other deposition parameters (i.e. pulse frequency and positive pulse period, negative and positive target bias voltage, cathode and anode gas flow rates and current) are set to desired values and allowed to stabilize for at least 15 minutes if O_2 is used, and 5 minutes otherwise. A residual gas analyzer (RGA) is used to monitor the partial pressures of gas species, particularly oxygen. The deposition will not start unless the partial pressure of oxygen observed via RGA is stable. The processing pressure is nearly the same for all depositions, ~ 1.0-1.2 mTorr during each deposition.

The deposition starts when the stage shutter is opened. After the desired deposition time, the stage shutter is closed. The system is shut down in the following order; stage heater, stage rotation, reactive gas flow, target bias, and pulsar. The anode and cathode power and gas flow are left on for 15 minutes and then turned off, letting the cathode and anode purge for another 15 minutes with 10 sccm Ar through the cathode and 50 sccm Ar through the anode before completely turning them off. The purpose of leaving the ion source on longer after the deposition is to prevent any material from re-depositing on the cathode and anode, which can make it difficult to restart the ion source for the next deposition. The stage is allowed to cool in vacuum down to the ambient temperature, which takes approximately 75 minutes after the ion source is finished purging. When base pressure is reached ($\sim 8.0\times10^{-8}$ Torr) and the stage is cool, the load lock chamber is retracted from the main chamber and vented to atmosphere in order to remove the samples.

3.2 X-ray diffraction (XRD)

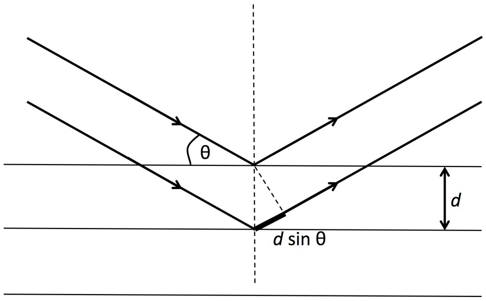

Figure 3.3 Schematic of basic XRD geometry on material with lattice spacing *d*.

X-ray diffraction (XRD) is a powerful analytical technique used to characterize the crystal structure and phase of thin film materials because the wavelengths of x-rays (Cu Kα is ~ 1.54 Å) are comparable to the atomic spacing in crystals. In a semi-classical mechanical model, XRD is a form of elastic scattering in which the incident x-ray photons have the same energy (wavelength) as that of the diffracted x-ray photons. A regular array of parallel equidistant atomic planes will reflect a small portion of an incident x-ray beam, which will produce a regular array of spherical waves. These will cancel each other out through destructive interference in most of the directions, except for the direction that satisfies Bragg's law [67]. In this direction, the waves add constructively, resulting in a reflection spot in the diffraction pattern. The law that describe the constructive interference is

$$2d \sin \theta = n\lambda \tag{3.1}$$

where n is an integer number describing the order of the reflection, λ is the wavelength of the X-rays (1.54 Å), d is the atomic spacing between the lattice planes, and θ is the Bragg angle at which a maximum diffraction intensity occurs. Figure 3.3 shows a schematic of the basic XRD geometry.

3.2.1 Out-of-plane $2\theta/\omega$

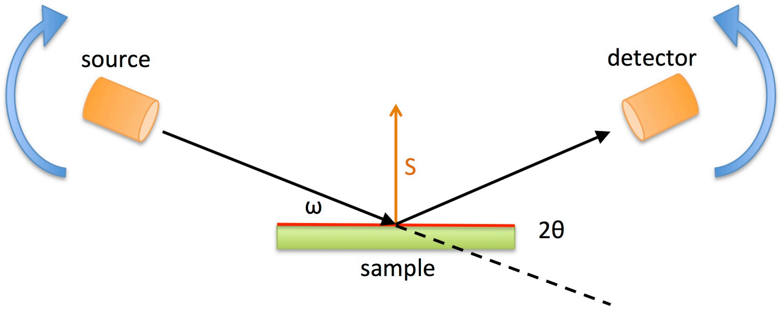

Figure 3.4 Schematic of $2\theta/\omega$ scan in Rigaku SmartLab XRD tool.

In an XRD tool, for an out-of-plane scan, the sample sits parallel to the ground, while the source and detector move up and down (in the vertical plane) with respect to the horizontal sample stage. For a $2\theta/\omega$ scan, the source moves with respect to the sample at an angle ω and the detector moves simultaneously by an angle 2θ, as shown in figure 3.4. The $2\theta/\omega$ scan is used to determine the phase composition in thin film samples and the lattice spacing can be extracted from the 2θ value via Bragg's law. The $2\theta/\omega$ scan can also distinguish between polycrystalline and textured growth. In this dissertation, the samples are either epitaxial or highly textured. In the case of highly textured growth, only selected sets of diffraction peaks corresponding to a family of lattice planes is observed.

3.2.2 In-plane $2\theta/\omega$, ϕ

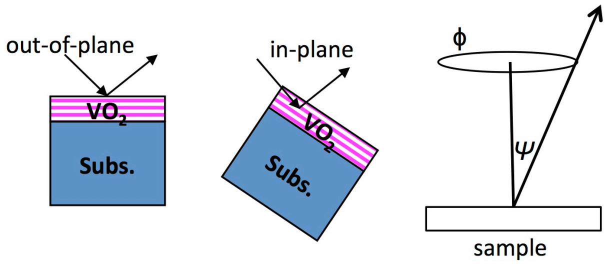

Figure 3.5 Schematic of in-plane $2\theta/\omega$, ϕ scans.

The in-plane scans are performed on a tilted sample as shown in figure 3.5. The tilt angle (ψ) is set to a fixed position with respect to the substrate normal for a desired lattice plane. Then the $2\theta/\omega$ is fixed to a value that satisfies the diffraction condition of the desired plane. The angle ϕ is scanned from 0° to 360° (the sample is rotated about the normal). The ϕ scan is used to determine the relative orientation of the film with respect to the substrate. For an epitaxial film, an additional in-plane $2\theta/\omega$ scan can be performed by fixing ϕ at an angle that yields maximum intensity (at a certain lattice plane) and $2\theta/\omega$ is scanned in the proximity of film and substrate peaks. Another lattice spacing d_{hkl} of the (hkl) plane can then be extracted from the $2\theta/\omega$ value. The lattice parameters can be calculated from a set of lattice spacing using the relationship:

$$d_{hkl} = \frac{1}{\sqrt{\frac{h^2}{a^2} + \frac{k^2}{b^2} + \frac{l^2}{c^2}}} \tag{3.2}$$

where a, b, and c are lattice parameters along [100], [010], and [001] of R-VO_2 respectively.

3.2.3 Temperature dependent XRD

The Rigaku SmartLab XRD tool is equipped with a domed hot stage (Anton Paar DHS 1100). The sample heating stage has a small spherical X-ray transparent dome that accommodates different atmospheres, i.e. air, inert gas, and vacuum (10^{-1} mbar). The heating stage is lightweight and equipped with air-cooling, and can be heated from room temperature to 1100 °C using a Rigaku software package. For some of the VO_2 samples, the out-of-plane $2\theta/\omega$ was performed at various temperatures in air (up to 380 K) to study the structural change. Figure 3.6 shows an example of the temperature dependent XRD pattern of a typical VO_2 thin film (deposited on *c*- Al_2O_3), with clear evidence of structural change around 340 K. The temperature range was set from 25 °C to 105 °C with a step of 10 °C for the scan at temperatures far from the MST and a step of 3-5 °C for the scan at temperatures close to the MST. At each temperature set point, the system was held for 2 minutes to wait for temperature stabilization and then the $2\theta/\omega$ scan was performed.

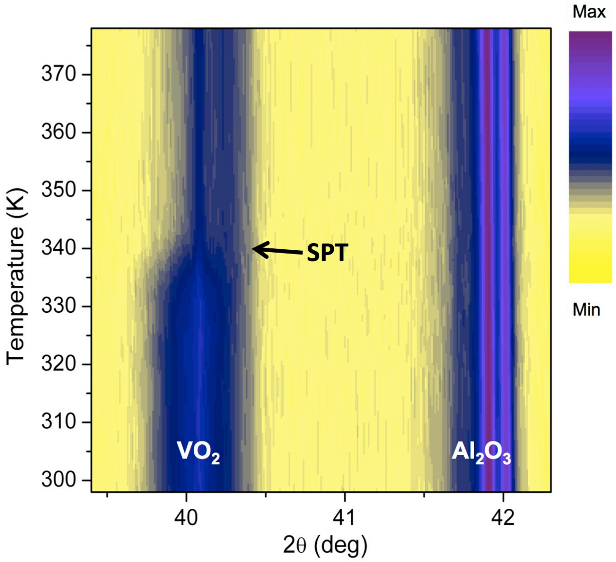

Figure 3.6 An example of temperature XRD results showing clear evidence of structural phase transition (SPT) at 340 K for a typical VO_2 thin film deposited on *c*-Al_2O_3.

3.3 X-ray reflectivity (XRR)

Film thickness is characterized via x-ray reflectivity (XRR). X-ray scattering at very small diffraction angles allows characterization of the electron density profile of a thin film. Through modeling/fitting of the reflectivity pattern, it is possible to obtain information about film thickness, interface roughness, and film density. The basic equation used to determine film thickness is [68]:

$$R = \left[\frac{r_1 + r_2 e^{-2i\beta t}}{1 + r_1 r_2 e^{-2i\beta t}}\right]^2 \tag{3.3}$$

where $r_{1,2}$ are Fresnel reflectivity coefficients of the film surface and the substrate-film interface respectively, β is the vertical component of the transmitted portion of the incident beam and t is the film thickness. An intensity maxima occurs whenever $e^{-2i\beta t} = 1$.

A typical XRR profile is shown in figure 3.7. The period of the oscillation of the interference fringes is related to the film thickness and the amplitude is related to the surface or interface roughness.

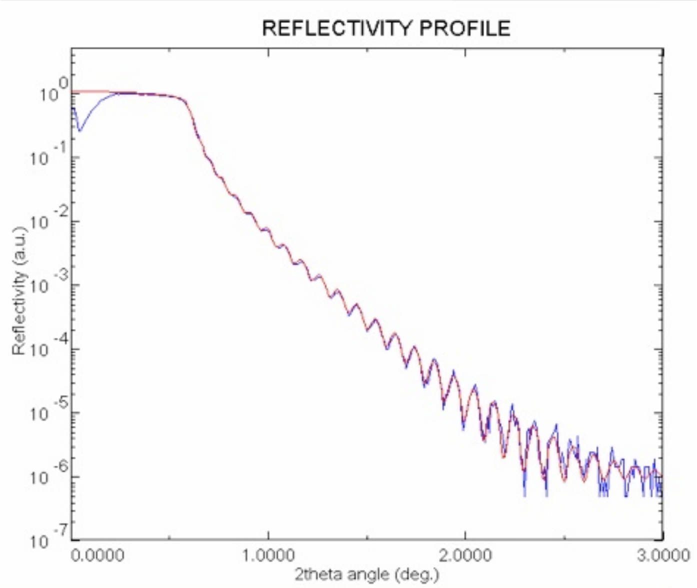

Figure 3.7 Typical XRR spectra of a VO_2 sample (blue) and the fitting simulation (red). The film thickness is related to the period of the oscillations.

3.4 Atomic force microscopy (AFM)

3.4.1 Surface morphology

Atomic force microscopy (AFM) was used to characterize the surface roughness of all VO_2 thin films. An Asylum Research Cypher AFM was used in tapping mode (ac air mode) for surface morphology. A schematic of the basic AFM mechanism is shown in figure 3.8. AFM consists of a cantilever with a sharp tip attached to its end. When the tip is brought close to the sample surface, forces between the tip and sample cause the cantilever to bend, and the deflection is detected by an array of photodiodes via a laser spot reflected from the top surface of the cantilever. In tapping mode, a piezoelectric forces the cantilever to oscillate near its resonance frequency. As the tip comes close the sample surface, the amplitude of this oscillation decreases due to forces between the sample and tip. The height of the cantilever, the distance between the cantilever and the surface of the sample, is controlled by a piezoelectric actuator. As the sample is scanned using piezoelectric scanners, the height of the cantilever is adjusted such that the oscillation amplitude is fixed. An image of the surface is produced from the deflections detected by the photodiode, occurring due to the height adjustments of the cantilever as the sample is scanned.

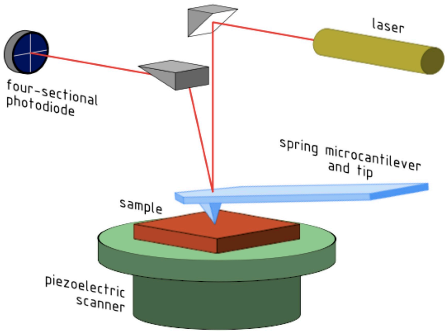

Figure 3.8 Schematic of basic AFM mechanism. [69]

3.4.2 Conductivity mapping

Conductive AFM (cAFM) imaging was performed using a module in the Asylum Research Cypher AFM tool. The module consists of a conductive cantilever holder and a conductive cantilever and tip. It provides low-current measurements at constant applied voltage for electrical characterization. The cantilever holder used in the system is the Dual Gain Orca cantilever holder, which has gains of 1×10^6 and 1×10^9 volts/amp (~1 pA to 10 μA). Before each cAFM, the holder was tested with two test resistors: 1 and 500 MΩ, to check both gains of the system. Schematics of the testing circuit and cAFM are shown in figure 3.9. After the testing was finished, the test resistor was then replaced with the cantilever/tip and sample. The sample was mounted to a sample holder with silver paint, where the silver paint covered one corner of the sample. The sample holder is conductive and magnetic; a tiny magnet pillar was placed on the holder to connect a wire from the sample back to the AFM system, making a complete electrical circuit. The conductivity mapping of the sample surface was then collected from a scan in contact mode while applying a small bias voltage and reading the current. The surface morphology of the same area was also collected at the same time. The conductivity mapping can also be plotted as an overlay on the surface morphology in 3D mode for a better overview of the relationship between the morphology and the conductivity of the thin film samples.

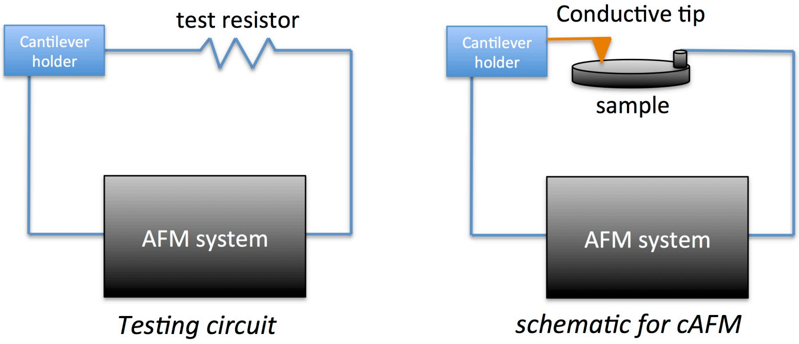

Figure 3.9 Schematics of testing circuit and conductive AFM mechanism.

3.5 Determination of the valence state of vanadium

To determine the valence state of vanadium, soft X-ray absorption (XAS) and photoemission (XPS) were performed at Beamline X1B of the National Synchrotron Light Source, Brookhaven National Laboratory by Dr. Jude Laverock at from Boston University. XAS measurements were performed at a resolution of 0.3 eV in both total electron yield (TEY) and total fluorescent yield (TFY) modes, which have probing depths of 10 nm and 100 nm respectively. XPS measurements were performed with a Scienta-

100 hemispherical analyzer, with energy resolution of 0.4 eV for the V 2*p* / O 1*s* core level (h*υ* = 900 eV) and 0.7 eV for the valence band measurements (h*υ* = 700 eV). Resonant photoemission spectroscopy (RPES) measurements, in which the incident photon energy is tuned to a feature of the absorption spectrum, were performed across the V $L_{3,2}$-edge (h*υ* = 510 – 525 eV) in order to resonantly enhance the photoelectron transition rate of the V 3*d* electrons.

3.6 Transport characterization

3.6.1 Micro-fabrication process

The transport characterizations were performed on thin film devices which were fabricated via a photo-lithography process. There are two types of device structures: simple-square contact (for R vs. T measurements), and Hall bar devices (for both R vs. T and Hall effect measurements).

(a) Simple current in plane devices

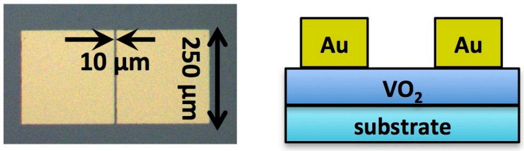

Figure 3.10 Schematic of a typical resistor device. Typical contacts were fabricated from 20 nm of Ti and 100 nm of Au by e-beam evaporation. The typical size of the contacts was 250×250 μm^2 separated by a gap of 10 µm.

The simple-square contact devices were fabricated using a photolithography procedure in a clean room to make top Ohmic contacts on blanket films. The step-by-step procedure is listed below:

1. Spin clean the sample with methanol+isopropanol and bake at 100 °C for 1 minute
2. Spin on photoresist (PR) AZ nLof 2020 at 4000 rpm for 30 seconds
3. Soft bake (pre-exposure bake) the sample at 110°C for 1 minute
4. Use the photolithography mask and contact aligner, expose the PR to UV at constant power of 275 W for 6 seconds
5. Post-exposure bake at 110°C for 1 minute
6. Develop the PR in AZ 300 MIF developer for 1 minute, then soak in DI for few seconds
7. Dry with UHP N_2, and check the pattern in optical microscope
8. Use electron beam evaporation to deposit 200 Å of Ti at a rate of 2 Å/s follow by 1000 Å of Au at a rate of 3 Å/s
9. Soak the sample in an acetone ultrasonic bath with low power to lift off the remaining PR leaving only the Ohmic contacts

(b) Hall bar devices

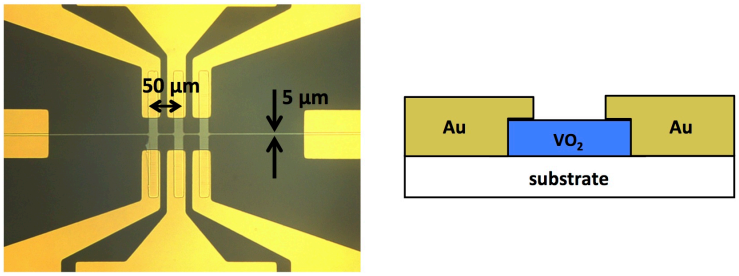

Figure 3.11 Schematic of a typical hall bar device. The VO_2 thin film was etched via RIE+ICP. Typical contacts were fabricated from 20 nm of Ti and 200 nm of Au by e-beam evaporation. Typical hall bar width is 5 μm, where the separation between two voltage leads is 50 μm.

Hall bar devices were fabricated using a photolithography procedure that consists of two main parts: Hall bar patterning and film etching, and contact patterning and evaporation following same procedure as listed in the previous section for simple-square contact devices. The first step is etching using a reactive ion etching (RIE) and inductively coupled plasma (ICP) technique. The step by step procedure for Hall bar patterning and etching is listed below:

1. Spin clean the sample with methanol+isopropanol and bake at 100 °C for 1 minute
2. Spin on photoresist (PR) AZ 4210 at 4000 rpm for 30 seconds
3. Soft bake (pre-exposure bake) the sample at 100°C for 1 minute
4. Use the photolithography mask and aligner and expose the PR to UV at constant power of 275 W for 36 seconds
5. Develop the PR in a 4:1 solution of DI water: AZ 400K developer for 1 minute, then soak in DI for few seconds

6. Dry with UHP N_2, and check the pattern in optical microscope
7. Put the sample in the dry etching tool which combines RIE+ICP: set the pressure 30 mTorr, ICP power 50 W, RIE power 20 W, O_2 4 sccm, SF_6 4 sccm, Ar 40 sccm. (Etch rate for VO_2 ~ 80 nm/min).
8. Soak the sample in acetone ultrasonic bath with low power to remove the PR, use a small cleaning swab if needed

After the etching was completed, the sample was prepared for contact patterning and evaporation with the same procedure as listed in section (a) simple-square contact devices, but with thicker Au/Ti that is thick enough to cover the etched thin film.

3.6.2 Temperature dependent resistivity

The temperature dependence of the dc resistivity was measured using a Versalab system (Quantum Design) from 250 to 400 K with a ramp rate of 2 K/min. The excitation current used ranged between 1 μA and 1 mA (well below critical current density for the current-driven transition) depending on the resistance of the material. Measurements were made in AC mode. In this mode, the system generates a DC excitation and reads the potential drop across the sample. Next, a DC excitation in the opposite direction is generated and the potential drop is read again. The read-out is an average of the absolute value of the positive and negative voltage measured; hence the errors from DC offset heating voltages are eliminated. The dc resistivity or conductivity was then calculated according to the device geometry and thickness of the film.

The metal-semiconductor transition temperature (T_{MST}) of each sample was extracted from the derivative of the logarithm of the resistivity, where

$$T_{MST} = \frac{T_{up} + T_{down}}{2} \tag{3.4}$$

When $T_{up} = T$ where $\frac{d(\log \rho_{up})}{dT}$ is at a minimum, and $T_{down} = T$ where $\frac{d(\log \rho_{down})}{dT}$ is at a minimum. ρ_{up} is the resistivity from the up-sweep (the heat up curve), and ρ_{down} *is* the resistivity from the down-sweep (the cool down curve).

3.6.3 Hall measurement

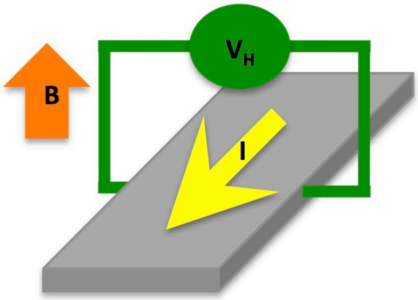

Figure 3.12 Schematic of basic Hall effect measurement.

The Hall effect was measured using a physical property measurement system (Quantum Design PPMS 6000), and Versalab system from 200 to 400 K with a 10 K step. A schematic of the Hall effect measurement is shown in figure 3.12. At each temperature, the magnetic field was then swept from -7 to 7 T for the PPMS and -3 to 3 T for the Versalab with a rate of 0.01 T/sec and a step of 0.1-0.2 T. At each magnetic field, an excitation current (ranging 1 μA - 1 mA depending on the resistance of the material) was applied, and the Hall voltage (V_H) was read. Therefore the Hall resistance was given by: $R_H^* = V_H^* / I$. Due to the misalignment of the Hall contacts, the magneto-resistance ($R_{MR}^{'}$) was included in R_H. The magneto-resistance is typically an even function of the external magnetic field for non-ferromagnetic materials, and the Hall resistance is an odd function. I separated the Hall resistance R_H^* the magneto-resistance $R_{MR}^{'}$ by

$$R_H^* = \frac{R_H(+H) - R_H(-H)}{2} \qquad (3.5)$$

$$R_{MR}^{'} = \frac{R_H(+H) + R_H(-H)}{2}$$

where $R_H(+H)$ and $R_H(-H)$ are the measured Hall resistance (V_H / I) at a positive magnetic field and a negative magnetic field, respectively. After extracting the Hall resistance, R_H^* vs. H was plotted at each temperature and the sign of the slope can be used to determine the type of the majority carrier: one sign for electrons and the opposite sign for holes (depending on the experimental configuration, i.e. direction of magnetic field, direction of excitation current, etc.)

Drude's model was used, assuming a one band model as a first-order approximation, using the Hall coefficient equation: $R_H = -1/(n\ e)$ to calculate the carrier density yields the equation:

$$\frac{V_H}{I} = -\frac{B}{d(ne)} \qquad (3.6)$$

where I is the excitation current, B – magnetic flux density directed perpendicular to the sample plane, V_H – Hall voltage (after the magneto-resistance removed), $e = 1.6 \times 10^{-19}$ coulomb, and d = film thickness. In other words, from the plot of R_H^* vs. H, the carrier density n can be extracted from the slope: $-1/(n\ e\ d)$. While the mobility:

$$\mu = \sigma/(n\ \mathrm{e}) \qquad (3.7)$$

was determined from the known value of conductivity σ (measured in 3.6.2) and carrier density n. The majority carrier density and mobility at each temperature were extracted using the methods described above. Plotting these values as a function of temperature together with the type of majority carrier noted will provide a better understanding of the transport properties of the material especially around the MST.

CHAPTER 4. Micro-strain induced by the oxygen related defects

4.1 Introduction

Recent efforts on a Mott field effect transistor (MottFET) have demonstrated that VO_2 can be employed as the channel in a MottFET, and the applied external gate voltage switches the channel resistance between the insulating OFF state and the metallic ON state [8-10]. There are still several challenges for these so-called "Mott devices" [11], among which is a concern regarding the repeatability/reproducibility of the Mott transition because the properties of these materials are sensitive to oxygen vacancy concentration, strain, and other factors. Understanding the role of defects and developing a suitable growth technique to maintain reproducibility is thus required to realize the potential applications of Mott oxides.

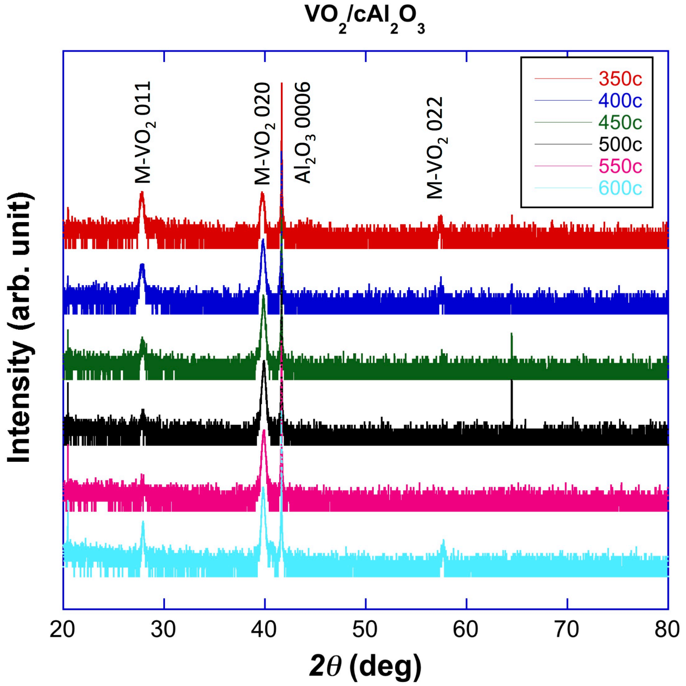

Figure 4.1 XRD show VO_2 film peaks coupling to sapphire substrate peak, for the films deposited in 6sccm Ar/O_2 at substrate temperature range 350-600 °C.

For an obvious reason, the substrate temperature for as-deposited films affects the film's crystallinity and its oxygen absorption ability, consequently affecting its transport properties. In figure 4.1, XRD scans reveal better crystallinity for the film deposited at a higher substrate temperature, and figure 4.2 shows a sharper transition, better resistivity ratio (OFF/ON ratio), and slight upshift of the transition temperature (T_{MST}) for the films deposited at higher temperatures. For the full range of substrate temperatures explored, especially with upper and lower limits of the optimum oxygen flow rate, additional phases of vanadium oxide were found and formed mixtures of V_6O_{13}, VO_2 and V_2O_3. [27]

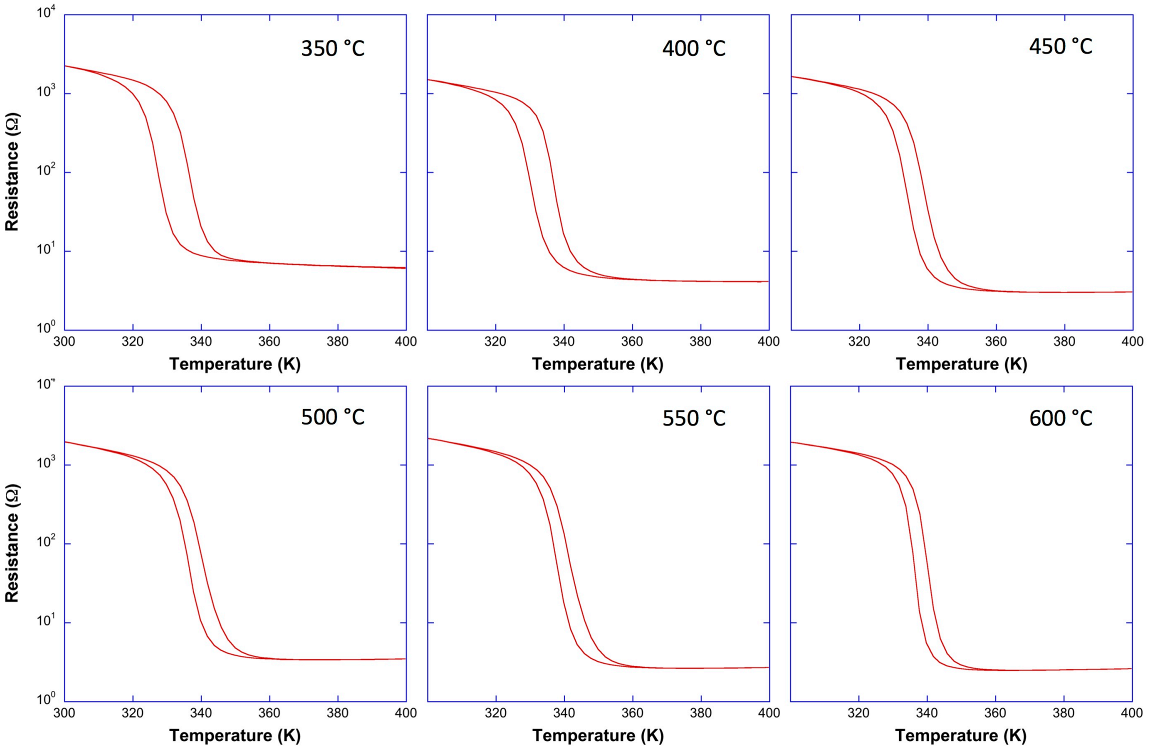

Figure 4.2 Resistance as a function of temperature for VO_2/*c*-Al_2O_3 deposited at different substrate temperature from 350-600 °C.

The growth and the physical properties of vanadium dioxide thin films have been explored by various deposition techniques such as electron beam evaporation [46-48], reactive sputtering [48-53], sol-gel process [54,55], chemical vapor deposition [55], atomic layer deposition [56], and pulsed laser ablation [57,58]. Though it was relatively straightforward to achieve a single phase VO_2, the MST behaviors, i.e. the transition temperature and the magnitude of resistivity ratio, lacked consistency in the literature. To discern the effect of oxygen content and the valence state of vanadium, I synthesized phase pure VO_2 films under different oxygen flow rates. Soft X-ray absorption (XAS) and photoemission (XPS) spectroscopy were used to characterize the thin films and investigate the valence state of the vanadium ion in these films. This work was carried out by Dr. Jude Laverock at Boston University. Despite the fact that the films are single phase, each sample has very distinctive transport properties. A systematic characterization of the electrical properties of these films was carried out using Hall devices, and I will discuss the correlation between the oxygen content, the electronic structure, and the MST

4.2 Morphological and structural characterizations

Reactive bias target ion beam deposition (RBTIBD) was used to grow VO_2 thin films on c-Al_2O_3 substrates with Ar/O_2 80/20 mixture flow rate set to 4.5-6.0 sccm. The total processing pressure was nearly the same for all depositions, ~ 1.2 mTorr during each deposition. The growth time was 37.5 min. Table 4.1 lists the deposition conditions for each sample in the set.

Table 4.1 Deposition conditions: Ar/O_2 80/20 was varied from 4.5 to 6.0 sccm while all other growth parameters remained constant.

GROWTH PARAMETERS	S-1	S-2	S-3	S-4
Negative Bias Voltage (kV)	0.90	0.90	0.90	0.90
Negative Bias Current (mA)	106	105	106	105
Positive Bias Voltage (V)	20.0	20.0	20.0	20.0
Positive Bias Current (A)	0.49	0.49	0.48	0.48
Cathode Ar Flow (sccm)	10	10	10	10
Cathode Voltage (V)	6.4	6.3	6.3	6.4
Cathode Current (A)	7.06	7.06	7.06	7.06
Anode Ar Flow (sccm)	70	70	70	70
Anode Voltage (V)	36.7	35.9	34.0	34.3
Anode Current (A)	6.55	6.55	6.55	6.55
V Target Frequency (kHz)	71.43	71.43	71.43	71.43
V Target Positive Pulse Period (μs)	3	3	3	3
Ar/O_2 80/20 Flow (sccm)	4.5	5.0	5.5	6.0
Substrate Temperature (°C)	450	450	450	450
Process Pressure (mTorr)	1.2	1.3	1.2	1.2

The film thickness was determined by XRR and the thickness of each film is shown in table 4.2. AFM has revealed that the lower oxygen flow rate samples have smaller grains and a smoother surface compared to the higher oxygen flow rate samples: the 4.5 sccm sample has a root-mean-square (RMS) roughness of 0.5 nm, while the 6.0 sccm sample has a RMS roughness of 1.8 nm as shown in figure 4.3. The increase of the grain size can be explained in terms of mean free path. In the presence of background Ar and O_2 gas, the molecular and atomic species in the chamber undergo frequent collisions. An increase in O_2 partial pressure leads to decrease in mean free path, hence the number of collisions increases. Due to the large number of collisions, the clusters formed have a greater chance of merging with each other, creating bigger clusters before depositing on the substrate. There were no cracks or pinholes observed on a large 20 x 20 μm^2 area (not shown here), as a result, the effect of these defects on the transport properties can be ruled out.

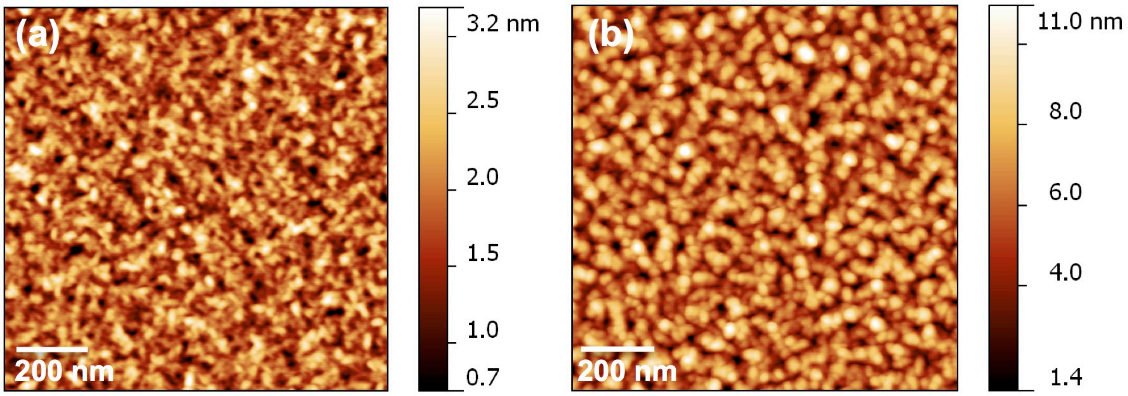

Figure 4.3 AFM images of (a) 4.5 sccm Ar/O_2 sample, (b) 6.0 sccm Ar/O_2 sample.

XRD scans showed that the VO_2 films deposited on the c-plane Al_2O_3 single-crystal substrates were single phase and highly textured. The out-of-plane *2θ* scans [figure 4.4(a)] show that the (020) peak in the VO_2 diffraction pattern is coupled to the (0006) peak of the Al_2O_3 substrate, and the VO_2 peak was the only peak detected in a wide-range *2θ* scans (not shown here). This indicates that there are no secondary phases in all the films despite the fact that they were deposited under various O_2 atmospheres. The (020) texture for VO_2 is typical when the template is *c*-plane sapphire [70]. There were clear Kiessig fringes in the out-of-plane *θ-2θ* scan observed in all samples, indicating high crystallinity with smooth interfaces, uniform thickness, and low defect density. The in-plane azimuthal scans of the (011) peaks of *M*-VO_2 and the (2204) peaks of Al_2O_3, as shown in figure 4.4(b), confirmed that the films are highly textured with three preferred orientations of monoclinic VO_2 clamping on the hexagonal shape of the

Al_2O_3 crystal. Each of the *M*-VO_2 orientations gives the corresponding two peaks, that in total give six peaks for (011) *M*-VO_2.

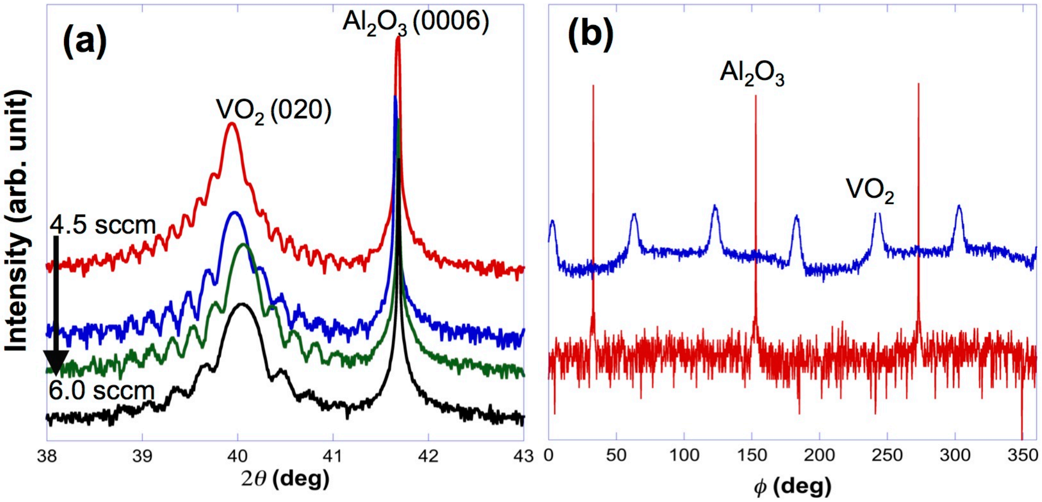

Figure 4.4 (a) Room temperature out-of-plane XRD data of Al_2O_3 (0006) and VO_2 (020). (b) The in-plane azimuthal scans of the (011) peaks of *M*-VO_2 and the (2204) peaks of Al_2O_3.

Figure 4.4(a) shows that as the Ar/O_2 flow rate increases, the diffraction peak for the (020) reflection shifts to larger *2θ*, resulting in a smaller lattice parameter. In comparison, the film deposited using a 6.0 sccm Ar/O_2 flow rate has a smaller *b*-spacing ([010] lattice parameter) compared to the film deposited at the 4.5 sccm flow rate.

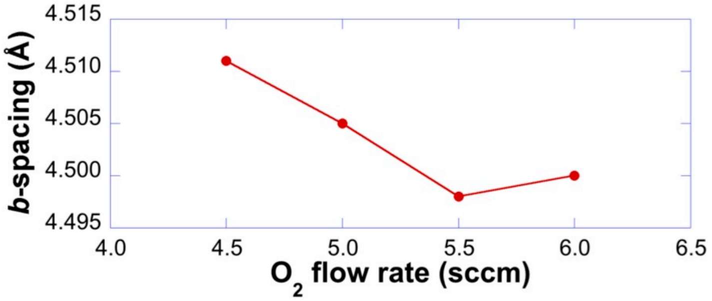

Figure 4.5 The effect of O_2 flow rate on lattice parameter '*b*' (*b*-spacing).

The effect of oxygen flow rate on the lattice parameter 'b' is shown in figure 4.5. I estimated the lattice parameters for the (010) reflection for different films deposited under various Ar/O_2 mixture flow rates. Using the values of 2θ from the diffraction pattern, I calculated the relative b-spacing of monoclinic VO_2 to be

$$b_{relative} = \frac{b_{peak} - b_{bulk}}{b_{bulk}} \tag{4.1}$$

where b_{peak} is the estimated b-spacing of M-VO_2 calculated from the (020) peak, and b_{bulk} is the lattice parameter along [010] of bulk monoclinic VO_2 which is 4.517 Å [71].

4.3 Valence state of vanadium

To determine the valence state of vanadium, soft X-ray absorption (XAS), photoemission (XPS) and Resonant photoemission spectroscopy (RPES) measurements were performed at Beamline X1B of the National Synchrotron Light Source, Brookhaven National Laboratory by Dr. Jude Laverock from Boston University.

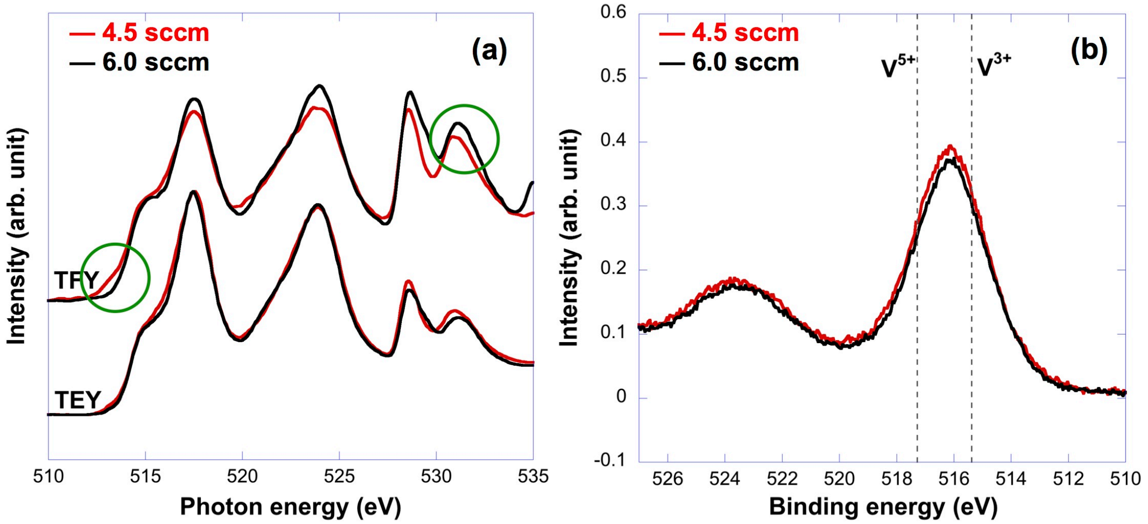

Figure 4.6 (a) V $L_{3,2}$-edge and O K-edge XAS, TFY is more bulk sensitive, and TEY is more surface sensitive. (b) V 2p XPS (courtesy of J. Laverock *et al.*).

To identify the valence state of the vanadium ion, soft X-ray absorption spectra were obtained [72]. For clarity, only spectra from the 4.5 sccm and 6.0 sccm samples are shown. Figure 4.6(a) shows the V $L_{3,2}$-edge and the O K-edge absorption spectrum. There is no indication of the mixed valence states of V in both TEY (more surface sensitive) and TFY (more bulk sensitive) modes, despite the difference in the oxygen flow rate and the lattice parameter. Different V charge states have quite different multiple structures in the V $L_{3,2}$-edge absorption spectrum, the most obvious difference being in their peak location. This change was not observed. The valence state of vanadium is also determined by V 2p XPS as shown in figure 4.6(b). The two structures are V $2p_{1/2}$ and $2p_{3/2}$ core levels. These are very sensitive to the V charge state, with the peak feature shifting by around 2 eV from V^{3+} to V^{5+} (as indicated). According to Silversmit *et al.* [73], the peak energies in figure 4.6(b) are consistent with the V^{4+} oxidation state, i.e. to VO_2. There is no shift in the V 2p core levels between the two extreme end-members of the set, indicating the valence state of vanadium cations does not change. XPS is surface sensitive; thus these results indicate that at least the surface is V^{4+} across the series. The absence of any shift in the V $L_{3,2}$-edge TFY [figure 4.6(a)], a bulk sensitive mode, suggest that the valence state of vanadium is also V^{4+} across the bulk of the films.

It is worth noting that there are two subtle features (circled) in the absorption spectrum that show some differences between the two end-members. Firstly, the pre-edge of the V L_3-edge*,* at around 514 eV, extra weight was observed in the 4.5 sccm sample. These states correspond to unoccupied states available at lower energy, indicating that the band gap has closed above the Fermi level for the 4.5 sccm sample. However, as shown in the O *K*-edge absorption [figure 4.6(a)], there is only a very weak change in the onset energy between the two samples. Therefore, the extra states available at lower energy are associated with pure V 3*d* states, i.e. with the V-V (along the *c*-axis) bonds. Secondly, there is an evolution in the crystal-field splitting of the t_{2g} and e_g states, shown in the O *K*-edge spectrum [figure 4.6(a)]. This is most likely due to the evolution in the structural distortion of the VO_6 octahedra associated with the change in the *b*-axis lattice parameter. The 6.0 sccm sample has a smaller *b*-axis lattice parameter than the 4.5 sccm sample. This means that the V 3*d* states feel the effects of the crystal field more strongly and the crystal field splitting increases. In other words, the 6.0 sccm sample should have a larger separation between t_{2g} and e_g states in accordance with the XAS results.

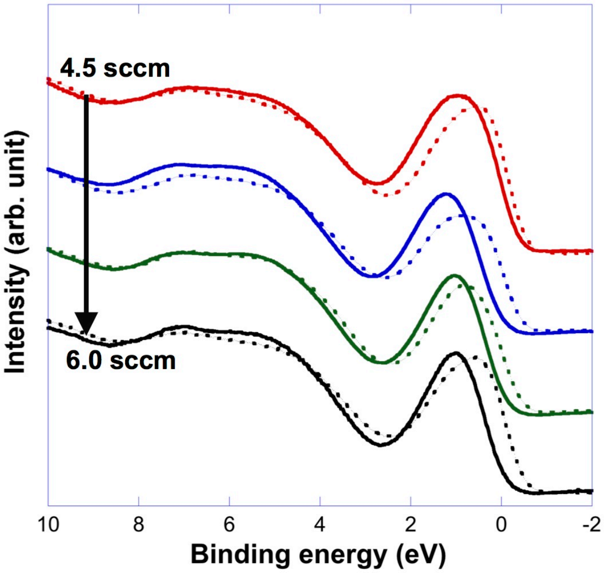

Figure 4.7 V L_3-edge resonant photoemission. Dashed lines are HT (metallic), solid lines are RT (insulating).

Resonant photoemission spectra (resonant with the V L_3 edge) are shown in figure 4.7. The RPES enhances the photoemission transition rate of those states that the incident photons are resonant with, in this case the V 3*d* states. The RPES results show the V 3*d* band more clearly across the transition. On both resonances (L_3 and L_2), the insulating gap is found to be much smaller for the 4.5 sccm sample, with the 6.0 sccm sample having a larger gap. The other two samples lie approximately in between, although the 5.0 sccm sample has a larger gap than the 5.5 sccm sample. It shows that the V 3*d* states were found to extend much closer to the Fermi level in the insulating phase, which was deposited with 4.5 sccm, compared with 6.0 sccm sample. The electronic structure observed near the Fermi level was expected to be in agreement with the transport behaviors shown in figure 4.8(a), where the insulating phase of the 4.5 sccm sample is much more conductive than that of the 6.0 sccm sample. The soft X-ray spectroscopy results show that the insulating gap closes symmetrically (i.e. both occupied and unoccupied states close) for the 4.5 sccm sample. The states involved in closing the gap are most likely V-V bonding electrons, since the O partial density of states shows only weak evolution with flow rate.

4.4 Transport properties

4.4.1 Metal semiconductor transition

To characterize the transport behavior of the films, Hall bar devices were fabricated for 4-point measurements. The Ohmic contact was 100 nm Au / 10 nm Ti, deposited by electron beam evaporation. The temperature dependence of the dc resistivity was measured from 300 to 400 K with a heating/cooling rate of 2 K/min. The *dc* resistivity was then calculated according to the device geometry and the thickness of the film. The Hall effect was measured from 300 to 400 K with a 10 K increment, sweeping the magnetic field from -7 to 7 T at each temperature. The Hall effect measurement was then extended from 200 to 400 K for the 4.5 sccm and 6.0 sccm samples.

The resistivity as a function of temperature is shown in figure 4.8(a). There are very distinguishable differences in the transport properties for the various samples, despite the fact that all of the samples are phase pure VO_2 with the same valence state for the vanadium cations. The insulating phase of the lower Ar/O_2 flow rate samples is more conductive than that of the higher Ar/O_2 flow rate samples, while the resistivity of all samples in the metallic phase are at about the same value; hence the lower Ar/O_2 flow rate samples exhibit a much smaller change in resistivity across the MST. The 6.0 sccm sample has the highest change in resistivity of about three orders of magnitude, while the change in resistivity of the 4.5 sccm sample drops down to just below one order of magnitude.

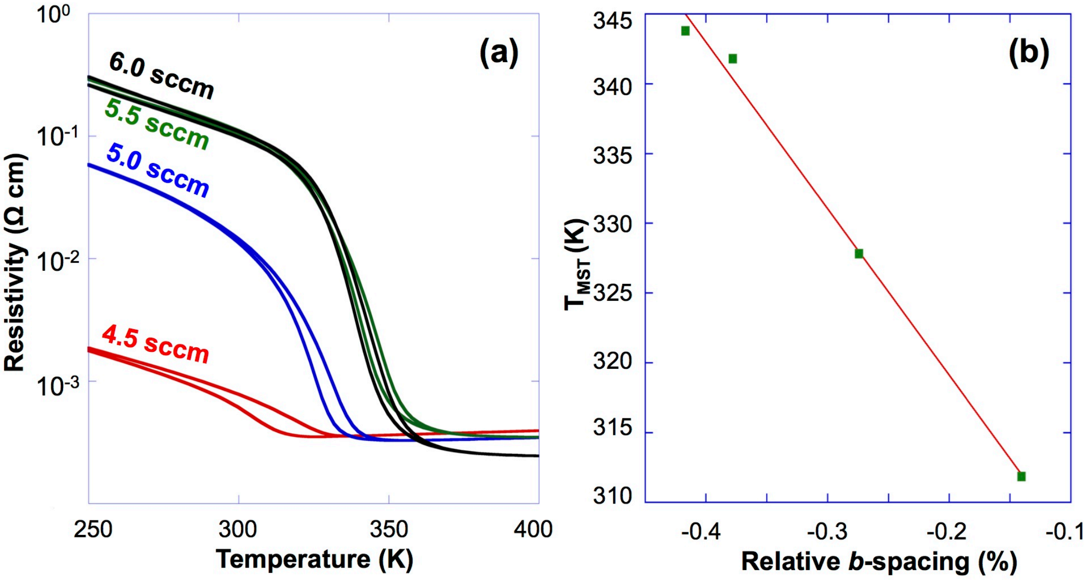

Figure 4.8 (a) dc resistivity as a function of temperature. (b) Transition temperature as a function of relative *b*-spacing.

The resistivity measurements of all samples also show a hysteresis loop around T_{MST} of each sample, which gets smaller as the Ar/O_2 flow rate increases. Extracting the results from resistivity measurements and XRD results clearly show that as the (010) spacing (i.e. relative *b*-spacing) increases, the T_{MST} of the sample also decreases toward room temperature as shown in figure 4.8(b). The shift in the T_{MST} and the drastic change in the transport properties are most likely due to the change in (010) spacing and the distortion introduced by different Ar/O_2 flow rates. The epitaxial strain in VO_2 grown on *c*-plane Al_2O_3 substrates was found to be fully relaxed at the thickness of 25 nm due to the large lattice mismatch between VO_2 and Al_2O_3 [74], hence it is plausible to conclude that the epitaxial strain is similar in 4.5 to 6 sccm samples despite the various thicknesses. According to the unit cell volume conservation, as the *b*-spacing increases, or as the (010 spacing becomes larger, the *c*-axis is expected to shorten proportionally and T_{MST} decreases accordingly, which is in agreement with a previous report by Y. Muraoka [40]. While the unit cell volume conservation may not hold true, especially for the thin films, the relationship of T_{MST} and oxygen partial pressure is in good agreement with a previous report [53]. The effect of oxygen partial pressure on the out-of-plane lattice parameter is also similar with Kaushal and Kuar's result when they deposited $(WO_3)_{1-x}(VO_2)_x$ nanocomposite thin films by pulsed laser deposition [75].

Table 4.2 Electrical transport properties of the 4 samples with different O_2 flow rate

	4.5 sccm	5.0 sccm	5.5 sccm	6.0 sccm
Thickness (nm)	66	50	45	35
T_{MST} (K)	311.9	327.8	343.8	341.8
R_{300K}/R_{400K}	~2.0	~41.9	~318.5	~440.5
n_{300K} ($\times 10^{20}$ cm^{-3})	~753	~1.49	~2.67	~0.24
n_{400K} ($\times 10^{20}$ cm^{-3})	~1250	~6130	~4140	~104
μ_{300K} (cm^2/Vs)	0.05	0.80	0.20	0.70
μ_{400K} (cm^2/Vs)	0.06	0.05	0.04	0.80

The magnitude of strain that is necessary to cause the change in the spacing was not pre-determined by the film thickness, but most likely by the oxygen partial pressure. The effect of film thickness on transport behavior was reported previously [74]. The transition temperature was shifted from lower temperatures to 340 K with an increase in thickness that was attributed to the strain relaxation as a function of film thickness. The opposite trend is observed in this experiment as summarized in table 4.2, which means that the T_{MST} reported here is more likely the affect of the oxygen partial pressure than the film thickness.

4.4.2 Carrier type and mobility

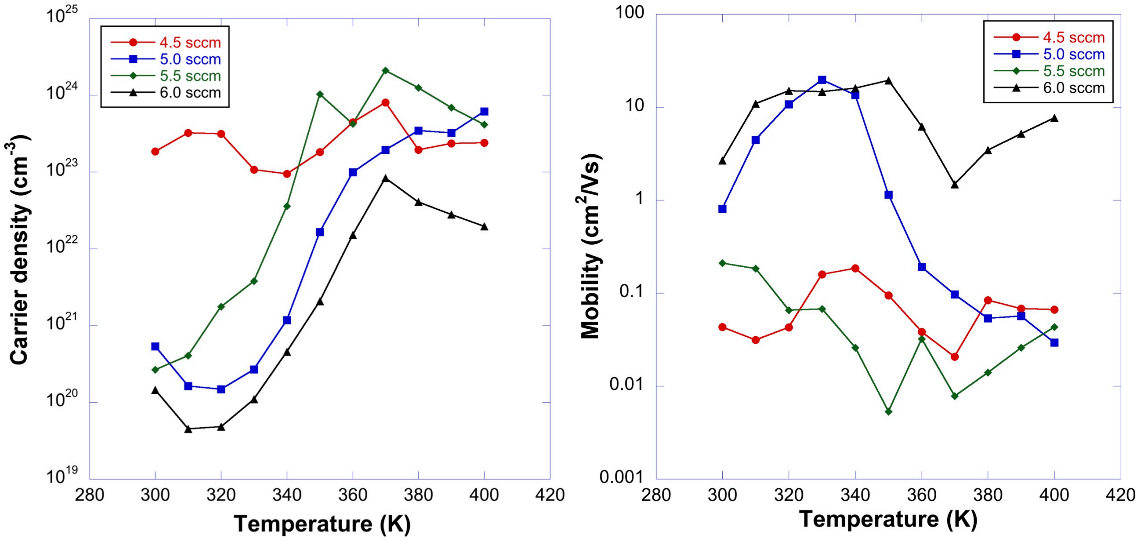

Figure 4.9 Carrier density and mobility as functions of temperature extracted from Hall effect measurements.

The Hall effect was measured on all samples from 300 to 400 K with a 10 K increment, sweeping magnetic field from -7 to 7 T at each temperature. The extracted carrier density and carrier mobility are shown in figure 4.9 and also summarized in table 4.2. There exists an abrupt change in the carrier density around the transition temperature, while the mobility seems to be constant before and after the transition. In the vicinity of the transition temperature, for the 5.0 and 6.0 sccm samples, there occurs a maximum of the mobility which is approximately 10-100 times larger than the mobility before and after the transition. Recently, Ruzmetov *et al.* [28] reported the same mobility trend for VO_2 thin films grown on *c*-plane Al_2O_3 substrates. Instead of the maximum, Ruzmetov *et al.* found that around the MST, there was a minimum mobility which was ten times smaller than the mobility both below and above T_{MST}. Unlike the higher flow rate samples, the 4.5 sccm sample has a very high carrier density. The carrier density of this sample does not have a large change around the transition temperature, while the mobility remains extremely low. The mobility of the 5.5 sccm sample looks more like the 4.5 sccm sample as there is no maximum around T_{MST} (~310 K for the 4.5 sccm). The majority carriers of all samples are electrons, except for the 4.5 sccm sample in which the majority carrier surprisingly switches to holes below room temperature as shown in figure 4.10, where the Hall measurements were extended to a larger temperature range of 200 - 400 K on the 4.5 sccm sample and the 6.0 sccm sample.

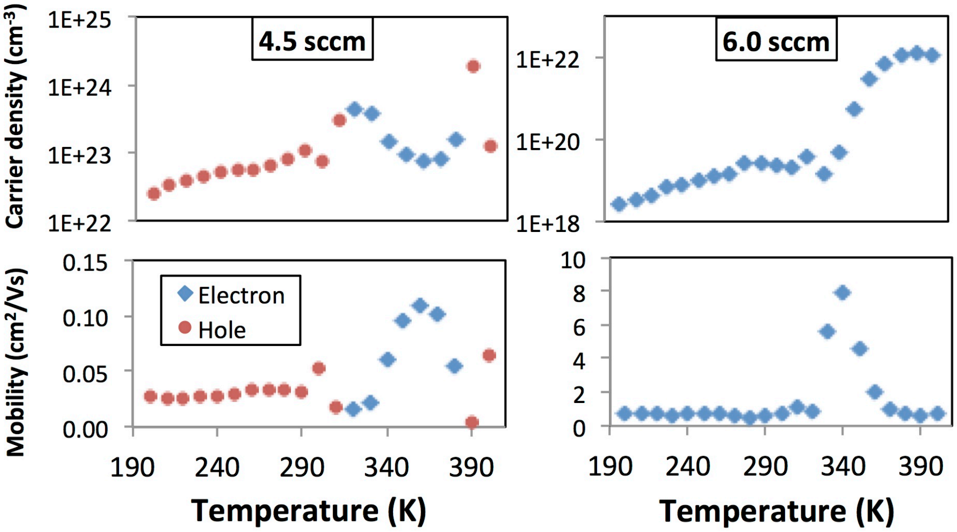

Figure 4.10 Carrier density and mobility as functions of temperature extracted from extended Hall effect measurements on two extreme samples.

4.5 Discussion

As the O_2 flow rate increased, the [010] lattice parameter for monoclinic VO_2 was reduced and coincidently distinctive changes in the metal-semiconductor transition (MST) and transport behaviors were observed despite the identical valence state of vanadium in these samples. It is likely that the oxygen-deficient growth condition probably led to the introduction of interstitial vanadium ions (do not contribute to the electronic structure) [18], which in turn led to increases in the carrier density and reduction in the resistivity of the material in the semiconductor state (RT). However since those interstitial V ions introduce extra electrons, as the flow rate decreases, the carrier density should also increase monotonically; the Hall effect results did not agree with this hypothesis. It is possible that the oxygen-deficient growth introduced interstitial V atoms instead, and if those V atoms are placed in between V-V pairs (as simulated in figure 4.11), the electrons trapped between the V-V pairs could be delocalized, resulting in a higher carrier density.

The interstitial defects result in an increase in the [010]-lattice parameter. The c_r-axis (a_m-axis) of the oxygen-deficient grown samples thus became smaller, resulting in a smaller T_{MST} as previously reported on epitaxial VO_2 deposited on TiO_2 [40]. On the other hand, oxygen-rich growth leads to V vacancies, reducing the [010]-lattice parameter. It is consistent with the transport behaviors if the interstitial V doping level is dilute (below the limits of detection) or the interstitial V only distorts the lattice, and does not donate electrons like V^{4+} cations on the lattice sites. Both the defects and the change in *b*-spacing directly contribute to the conductivity, especially in the insulating phase, but the effects seen in the electronic structure, i.e. closing of the gap, are more related to the strain. The results are consistent with interstitial V, however other techniques would be needed to properly study other types of defects such as oxygen vacancies.

Carrier mobility measured at room temperature did not significantly change throughout the series in agreement with the measurements conducted by Kwan *et al.* [76], so the resistivity is inversely proportional to the carrier density. In the semiconductor state, the crystal distortion reduces the stabilization, thus these extra carriers (electrons at RT) tend to lower the d_π level [18], and may screen the electron correlation energy of $d_{||}$ electrons [14] resulting in broadening lower $d_{||}$ band, closing both the insulating band gap and the separation of $d_{||}$ bands. In addition, the population of these thermally excited electrons increases with temperature as shown by the carrier density extracted from the Hall effect measurements. The effect is enhanced around T_{MST} and narrows the band gap of VO_2, resulting in a less sharp transition as shown in the resistivity measurement in figure 4.8(a).

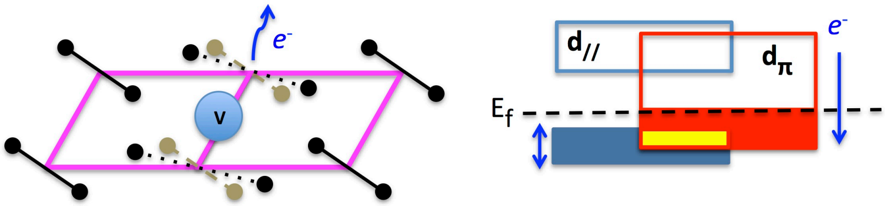

Figure 4.11 (Left) interstitial V atom with delocalized electron from rearranged V-V pair. (Right) electronic structure showing the effect of extra electrons in lowering d_π band, increasing screening effect.

4.6 Summary

In summary, VO_2 thin films were deposited on *c*-Al_2O_3 with different oxygen partial pressures. Despite the fact that the samples are single phase VO_2 and the valence state of V does not change much through the series, with predominantly V^{4+} in each sample, the transport properties of these samples are different due to the different Ar/O_2 flow rates during the deposition. The Hall effect measurements reveal very significant differences in carrier densities between samples deposited with higher and lower oxygen flow rates. The resistance as a function of temperature measurements also shows a shift of T_{MST}, and that the insulating phase of lower Ar/O_2 flow rate samples is much more conductive. This behavior is likely due to the strain that was caused by the different types of defects associated with the oxygen growth environments. The soft X-ray spectroscopy results show subtle evidence for the crystal distortions reflected by the different crystal-field splitting between the 4.5 and 6.0 sccm samples. These findings suggest that the repeatability and reproducibility of the Mott transition in VO_2 can be obtained when one discerns the effect of the growth condition on the film strain and the electronic structures.

CHAPTER 5. Macro-strain induced by substrate clamping effect

5.1 Introduction

This chapter focuses on transport phenomena in epitaxial VO_2 thin films deposited on TiO_2 single-crystal substrates. I investigated the role of the substrate clamping effect on the strain and its relation to the anisotropy of conductivity, and I also studied the effect of the magnitude of strain on transport behavior, i.e. MST. I also observed an unusually large conductivity anisotropy in epitaxial VO_2 films which was not previously reported.

The first part of this chapter investigates the effect of large strain on the properties of VO_2 films. One remarkable result is that highly strained epitaxial VO_2 thin films were rutile in the insulating state as well as in the metallic state. These highly strained VO_2 films appeared to undergo an electronic phase transition without the concomitant Peierls transition. The second part of the chapter explores the anisotropy of conductivity in VO_2 films deposited on (100) TiO_2.

5.2 Mott-like transition via thickness dependent strain

5.2.1 Growth conditions and surface morphology

VO_2 thin films with thicknesses of 5-17 nm in were grown on (100), (001), (011) TiO_2 and *c*-Al_2O_3 substrates, the growth conditions are listed in table 5.1. The thickness of the films was measured by XRR and summarized in table 5.2. The AFM images are shown in figure 5.1(a). The root-mean-square roughnesses of the films are also summarized in table 5.2. AFM showed a smooth and uniform surface without any cracks or pinholes. There are some signs of island growth mode for VO_2 in the very thin samples deposited for 10 minutes or less. This is due to the large lattice mismatch between the film and the substrate. The grain size also increases with the film thickness.

Table 5.1 Growth parameters of VO_2 thin films on various substrates

A: *c*-Al_2O_3, B: (100) TiO_2, C: (001) TiO_2, D: (011) TiO_2

GROWTH PARAMETERS	B1	A1, B2	A2, B3	A3, B4	C1, D1	C2, D2	C3, D3
Negative Bias Voltage (kV)	0.90	0.90	0.90	0.90	0.90	0.90	0.90
Negative Bias Current (mA)	102	102	102	102	102	102	102
Positive Bias Voltage (V)	20.0	20.0	20.0	20.0	20.0	20.0	20.0
Positive Bias Current (A)	0.50	0.50	0.50	0.50	0.50	0.50	0.50
Cathode Ar Flow (sccm)	10	10	10	10	10	10	10
Cathode Voltage (V)	6.7	6.7	6.7	6.7	6.6	6.7	6.7
Cathode Current (A)	7.06	7.06	7.06	7.06	7.06	7.06	7.06
Anode Ar Flow (sccm)	70	70	70	70	70	70	70
Anode Voltage (V)	35.5	35.6	35.6	35.6	35.0	35.0	35.2
Anode Current (A)	6.55	6.55	6.55	6.55	6.55	6.55	6.55
V Target Frequency (kHz)	71.43	71.43	71.43	71.43	71.43	71.43	71.43
V Target Positive Pulse Period (μs)	3	3	3	3	3	3	3
Ar/O_2 80/20 Flow (sccm)	6.0	6.0	6.0	6.0	6.0	6.0	6.0
Substrate Temperature (°C)	500	500	500	500	400	400	400
Process Pressure (mTorr)	1.1	1.1	1.1	1.1	1.2	1.2	1.2
Deposition time (min)	5	10	15	20	5	10	15

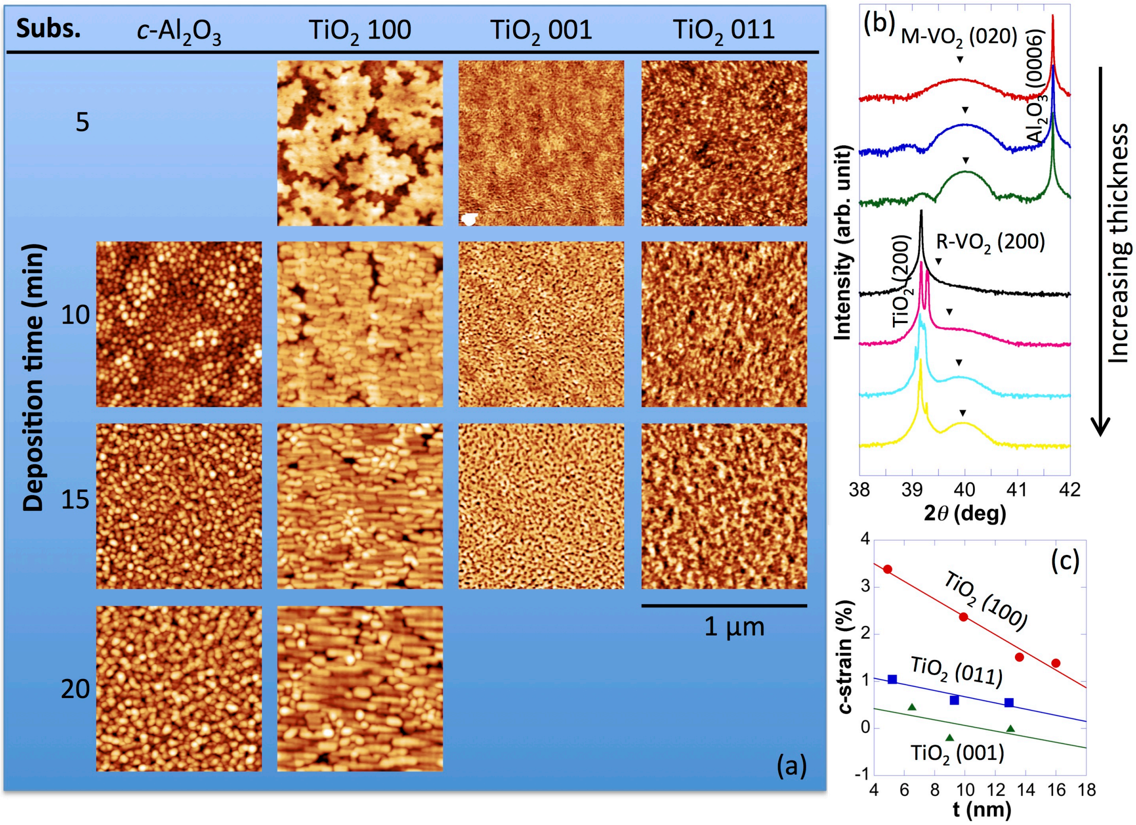

Figure 5.1 (a) 1×1 μm^2 AFM images of all samples (normalized scale for better detail), showing larger grains as the thickness increases. (b) 2θ XRD scans of VO_2/c-Al_2O_3 and VO_2/(100) TiO_2, showing theVO_2 peak (marked with down triangles) coupling to the substrate peak: the (020) peak of monoclinic VO_2 coupling to (0006) Al_2O_3, and the (200) peak of rutile VO_2 coupling to (200) TiO_2. The VO_2 peak shifts as the film thickness increases. There are Kiessig fringes around the VO_2 peak shown for VO_2/c-Al_2O_3, indicating a high quality film with smooth interfaces. (c) c_R strain vs. film thickness (t) for VO_2/(100) TiO_2 samples, showing a linear relationship with the fastest relaxation rate for (100) TiO_2 samples.

Table 5.2 Summary of thickness, RMS roughness, and lattice parameter (*b* or *c*)

Deposit time (min)	*c*-Al_2O_3			TiO_2 (100)			TiO_2 (011)			TiO_2 (001)		
	t (nm)	RMS (nm)	*b* (Å)	*t* (nm)	RMS (nm)	*c* (Å)	*t* (nm)	RMS (nm)	*c* (Å)	*t* (nm)	RMS (nm)	*c* (Å)
5				4.9	0.81	2.9493	5.2	0.19	2.8826	6.5	0.12	2.8660
10	8.7	1.60	4.5132	9.9	0.88	2.9204	9.3	0.24	2.8699	9.0	0.25	2.8475
15	12.7	0.40	4.5028	13.6	1.10	2.8961	12.9	0.34	2.8684	13.0	0.49	2.8529
20	17.0	0.60	4.5014	16.0	1.45	2.8924						

5.2.2 Crystal structure characterizations

(a) X-ray diffraction

The out-of-plane (2θ) XRD scans show that the (020) peaks of monoclinic VO_2 are coupled to the (0006) peaks of the Al_2O_3 substrate as seen in figure 5.1(b), and the VO_2 films deposited were highly textured. Furthermore, VO_2 was the only phase detected in wide-range 2θ scans: there were no other oxides grown on the substrate. As the films get thicker, the (020) VO_2 peaks shift to higher 2θ values, which means that the lattice parameter b (for monoclinic phase) gets smaller for thicker films. The lattice parameter b is reported in table 5.2. The Al_2O_3 substrate has hexagonal symmetry, and the structure of VO_2 deposited on top is monoclinic, which can have three preferred in-plane orientations according to the substrate and film crystal structures. The in-plane lattice spacing of bulk VO_2 is larger than that of Al_2O_3, hence an in-plane compressive strain is introduced for the films deposited on the Al_2O_3 substrates.

Table 5.3 Lattice parameters, in-plane spacing, and critical thickness of VO_2, TiO_2 (Å)

Material	***a***	***c***	d_{011}	d_{110}
R-VO_2	4.5546	2.8528	2.4177	3.2206
TiO_2	4.5936	2.9582	2.4871	3.2482
Mismatch (%)	0.86	3.69	2.87	0.86
H_c	2.6595	0.3861	0.4211	1.8806

Since VO_2 and TiO_2 both have a rutile crystal structure, a full epitaxial VO_2 films were deposited on TiO_2 substrates. The lattice parameters of bulk VO_2 are smaller that that of the TiO_2 substrate, hence this introduces an in-plane tensile strain due to this lattice mismatch as listed in table 5.3. Figure 5.1(b) also shows the out-of-plane XRD scans of the VO_2/(100) TiO_2 samples. The (200) peak in the VO_2 diffraction pattern is coupled to the (200) peak of the TiO_2 substrate, and it was the only peak detected in the wide-range scans (not shown here). The in-plane ϕ scans of the (101) plane, shown in figure 5.2, were performed to confirm the epitaxial growth of the VO_2. In-plane 2θ scans (figure 5.2) were also performed on the (110) and (101) planes of the substrate. The lattice parameters were directly determined from the 2θ peak positions of the (200), (110), and (101) peaks of VO_2, though only c is shown in table 5.2. The same processes were repeated on VO_2 films deposited on (001) and (011) TiO_2 substrates. All the lattice parameters, a, b, and c are plotted as a function of thickness in figure 5.1. As expected, epitaxial strains were relaxed with increasing thickness as shown in figure 5.1(c), and these films showed different relaxation rates as a function of the orientation of the TiO_2 substrate. The mechanism for strain relaxation is likely due to the introduction of misfit dislocations when the thickness of the epitaxial film is larger than a critical thickness, summarized in table 5.3.

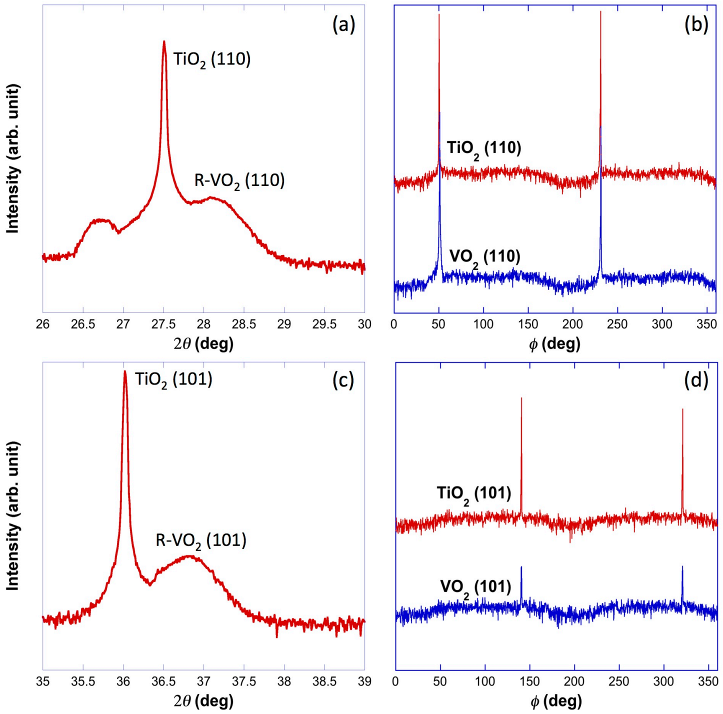

Figure 5.2 In-plane *2θ* scans of 15 minute deposited VO_2/(100) TiO_2 on (a) the (110) plane and (c) the (101) plane. (b) Azimuthal scans at the in-plane (110) VO_2 peak and (110) TiO_2 peak. (c) Azimuthal scans at the in-plane (101) VO_2 peak and (101) TiO_2 peak, confirming epitaxy growth and rutile structure of VO_2.

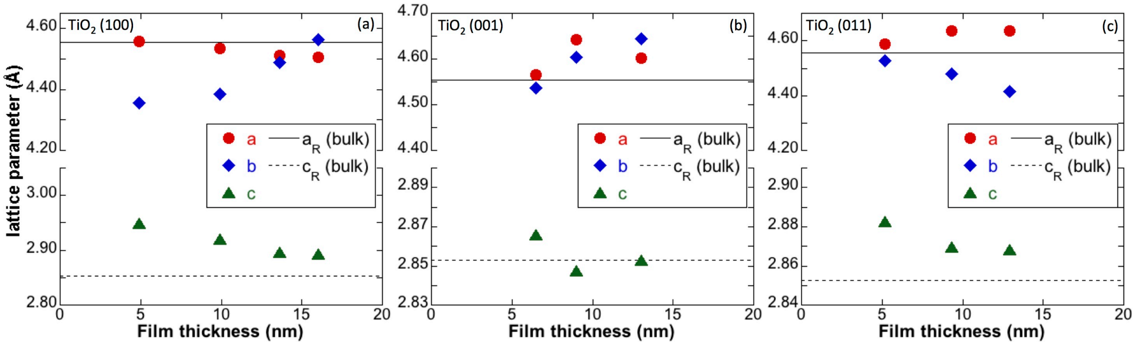

Figure 5.3 (a)-(c) Lattice parameters extracted from XRD as a function of film thickness for VO_2 deposited on (100), (001), and (011) TiO_2 respectively. The dashed and solid lines show bulk values. The trends of lattice parameters agree well with Hooke's law.

(b) Strain analysis

The strain and stress were analyzed using the elasticity tensor based on the rutile structure of VO_2, in order to understand the effect of substrate clamping on the strain/stress as a function of crystallographic orientation. For the epitaxially strained films presented here, the stress and the strain are second-rank tensors, and the Young's moduli is a fourth-rank tensor. Due to the crystal symmetry, Hooke's law can be expressed to matrix notation as shown below, with the stiffness (Young's modulus) of the tetragonal space group $P4_2$/mnm of VO_2 (*R*),

$$\begin{pmatrix} \sigma_1 & & \\ & \sigma_2 & \\ & & \sigma_3 \end{pmatrix} = \begin{pmatrix} E_{11} & E_{12} & E_{13} & & & \\ E_{12} & E_{11} & E_{13} & & & \\ E_{13} & E_{13} & E_{33} & & & \\ & & & E_{44} & & \\ & & & & E_{44} & \\ & & & & & E_{66} \end{pmatrix} \begin{pmatrix} \varepsilon_1 & & \\ & \varepsilon_2 & \\ & & \varepsilon_3 \end{pmatrix} \qquad (5.1)$$

where E_{ij} are the directional Young's moduli of *R*-VO_2, whereas E_{44} and E_{66} are for the shear stress. The property tensors are transformed for analysis by choosing the coordinate system as x_1//$[100]_R$, x_2//$[010]_R$, and x_3//$[001]_R$ for all the samples deposited on rutile TiO_2. For VO_2 thin films, it was found that E_{11} (E_{100}) is ~ 200 GPa,[77] and E_{12} (E_{110}) ~ 90 GPa [78]. However, there was a report on various simulated parameters, $E_{ij,}$ for single crystal VO_2.[79] Fan et al. developed a method based on Landau theory and phase field modeling to simulate the elastic constant E_{ij} of single crystal VO_2, and they found E_{11} = 492 GPa, E_{22} = 407 GPa, E_{44} =125 GPa, E_{55} =50 GPa, E_{12} =161 GPa, and E_{13} = 32 GPa. [79]. The epitaxial strains were calculated from $\frac{\Delta L_i}{L_i}$, *i.e.* $\varepsilon_1 = \frac{a - a_{bulk}}{a_{bulk}}$, where *a* is the measured lattice parameter along *a*-axis of VO_2 (*R*).

For further analysis, Eqn. 5.1 can be reduced to:

$$\begin{aligned}\sigma_1 &= E_{11}\varepsilon_1 + E_{12}\varepsilon_2 + E_{13}\varepsilon_3 \\ \sigma_2 &= E_{12}\varepsilon_1 + E_{11}\varepsilon_2 + E_{13}\varepsilon_3 \\ \sigma_3 &= E_{13}\varepsilon_1 + E_{13}\varepsilon_2 + E_{33}\varepsilon_3\end{aligned} \tag{5.2}$$

From Hooke's law, the bi-axially strained thin film boundary condition is applied according to the substrate orientation. It is stress-free along the out-of-plane direction, i.e. perpendicular to the film surface. For VO$_2$/(100) TiO$_2$, the condition $\sigma_1 = 0$ yields $\varepsilon_3 = \frac{E_{11}(-\epsilon_1)+E_{12}(-\epsilon_2)}{E_{13}}$. The strains ε_i were determined from the measured lattice parameters. They are positive if the lattice parameters are smaller than bulk values and negative otherwise. The plot in figure 5.3(a) agrees well with this formula. Both ε_1 and ε_2 are negative (compressive strains), while ε_3 is positive (tensile strain). As the in-plane tensile strain ε_3 decreases, the out-of-plane compressive strain ε_1 becomes more negative; hence the in-plane compressive strain $\varepsilon_2$becomes less negative, approaching zero (close to bulk value).

For VO$_2$/(001) TiO$_2$, the conditions $\sigma_1 = \sigma_2$, and $\sigma_3 = 0$, give $\varepsilon_1 = \varepsilon_2$, and $\varepsilon_3 = -\frac{2E_{13}}{E_{33}}\varepsilon_1$, respectively. The measured lattice parameters also agree with these conditions, as shown in figure 5.3(b). As the out-plane lattice parameter c_R decreases, the in-plane lattice parameter a_R increases. However, the measured out-of-plane strain ε_3 fluctuates around zero with a declining tendency when it should be negative (compressive), as the in-plane strains $\varepsilon_1$and ε_2 are both positive (tensile). The result could also mean that $E_{33} >> E_{13}$.

For VO$_2$/(011) TiO$_2$, the condition $\sigma_{[011]} = 0$ results in $\sigma_2 = -\sigma_3$, hence $\varepsilon_3 = \frac{(E_{11}+E_{13})(-\epsilon_2)-(E_{12}+E_{13})\epsilon_1}{E_{13}+E_{33}}$. In principle, from the substrate clamping effect, $\varepsilon_1$is positive (tensile). The measured lattice parameters plotted in figure 5.3(c) show that ε_2 is negative (compressive) and ε_3 is positive (tensile). As ε_3 is relaxed, ε_2 becomes more compressive, and the tensile strain ε_1 should increase faster than the compressive strain ε_2 (assuming $E_{11} > E_{12}$). The trend demonstrated by the evolution in the lattice parameters as a function of the film thickness agree with these nominal conditions, but the rate of change does not agree very well, implying that E_{12} may be larger than E_{11}.

In comparison, the stress and strain in the uniaxially strained nanobeams is very simple. [37,38] The uniaxial stress has the following stress tensor form:

$$\sigma = \begin{pmatrix} 0 & 0 & 0 \\ 0 & 0 & 0 \\ 0 & 0 & P \end{pmatrix} \tag{5.3}$$

Where *P* is the mechanical stress applied along *c*-axis of monoclinic VO_2. When *P* is tensile (positive), the strain along *c* is tensile, and the strains along [100] and [010] are compressive. When *P* is compressive (negative), the strains along [100], [010], and [001] change their signs accordingly.

(c) Raman spectroscopy

Figure 5.4(a) shows the Raman spectra of VO_2/TiO_2 compared to that of VO_2/*c*-Al_2O_3. The Raman spectroscopy was conducted at room temperature and at 150 °C with a 488 nm laser source. The spectra of VO_2/TiO_2 shown here (before substrate/background subtraction) were dominated by the TiO_2 signal at room temperature and at 150 °C; the Raman spectra of a plain (100) TiO_2 substrate is also shown for reference in figure 5.4(a), with the peaks of TiO_2 marked similar to a previous report [80]. The room temperature spectra of VO_2/TiO_2 did not reveal any insulating *M1* features, having peaks at 195, 224, and 615 cm^{-1}. Instead, the results showed small diffusive peaks after background subtraction, similar to what has been reported for metallic VO_2 (*Rutile phase*) [81] and to the result observed in the high temperature (*Rutile*) spectra of $VO_2/c\text{-}Al_2O_3$ shown in figure 5.4(a). Even though the lattice parameter c (i.e. c-strain) varies for the different film thicknesses, the Raman spectroscopy showed the *M1* phase only for all $c\text{-}Al_2O_3$ samples at lower temperature, and the ω_0 peak seems to shift slightly from 615 cm^{-1} to 617 cm^{-1} as the strain along [001] *M1*-VO_2 increased. The peaks are summarized in table 5.4. The tendency of the peak shift agrees with a previous report on VO_2 micro-beams, [38] but the *T* phase and *M2* phase were not observed in any of the samples.

Table 5.4 Raman shifts (cm^{-1}) of VO_2 samples

Substrate	**Thickness [nm]**	**Raman shifts [cm^{-1}]**				***c* or *b* [Å]***	**% "*c*-strain"**
TiO_2 100	4.9	142	232	446	611	2.9493	3.38
	9.9	142	232	446	611	2.9204	2.37
	13.6	142	232	445	611	2.8961	1.52
	16.0	142	233	446	611	2.8924	1.39
TiO_2 011	5.2	142	232	446	611	2.8826	1.05
	9.3	142	233	446	612	2.8699	0.60
	12.9	142	232	446	612	2.8684	0.55
TiO_2 001	6.5	142	231	447	611	2.8660	0.46
	9.0	142	233	445	611	2.8475	-0.19
	13.0	142	233	446	610	2.8529	0.004
Al_2O_3	8.7	195	224	***615***	750	4.5132	0.17
	12.7	192	224	***616***	750	4.5028	0.63
	17.0	193	224	***617***	749	4.5014	0.69

* For samples grown on sapphire, the values are for out-of-plane '*b*' for *M1* phase. For others, the values are for '*c*' lattice constant of *R* phase.

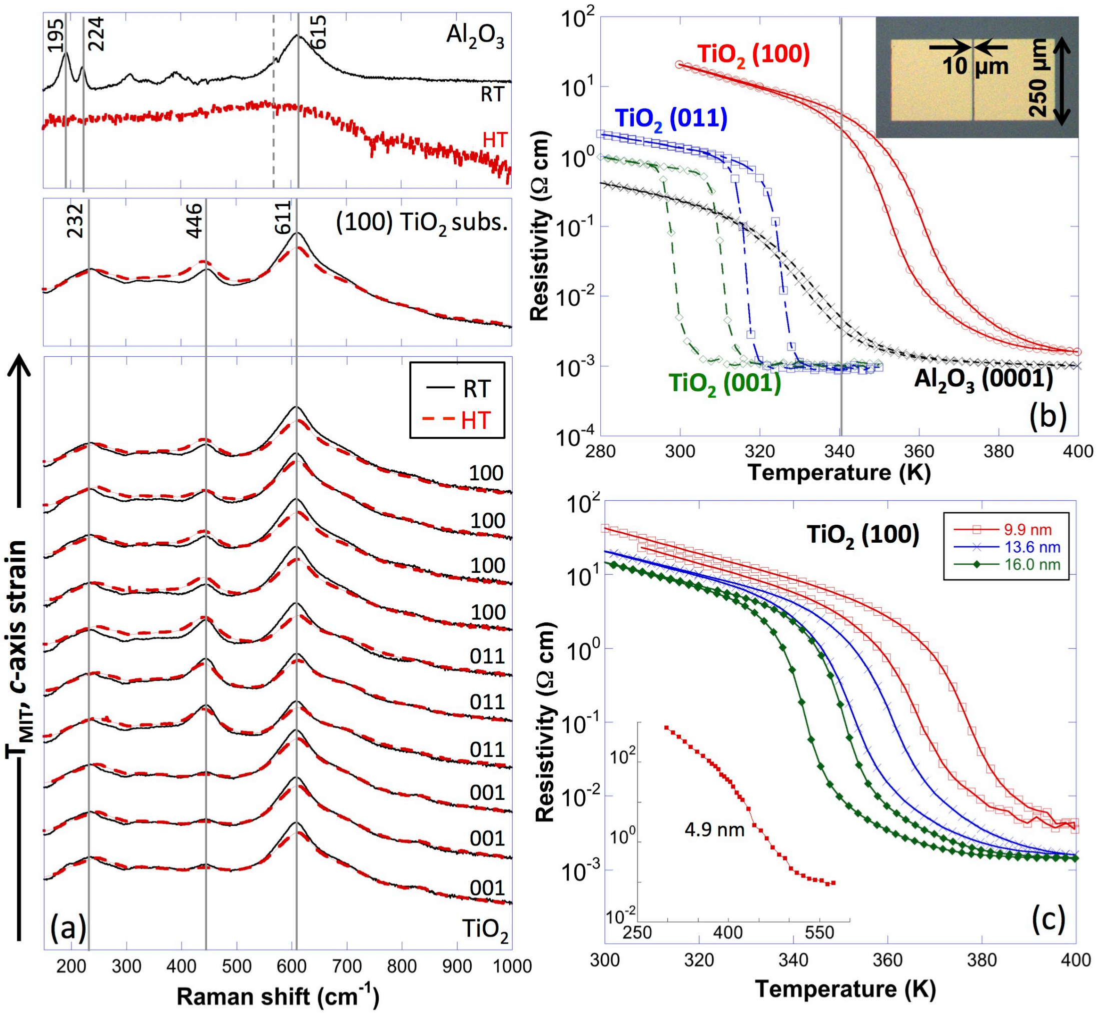

Figure 5.4 (a) Top: Raman spectra of VO_2 thin films grown on c-Al_2O_3 (for reference) showing insulating *M1* structure (significant peaks marked with solid grey lines) at room temperature and showing metallic rutile structure (broad peak at 570 cm^{-1} marked with a dashed line) at 150 °C respectively. Middle: Raman spectra of (100) TiO_2 substrate for reference. Bottom: Raman spectra of VO_2 thin films grown on TiO_2, measured at room temperature and 150 °C, the solid grey lines mark the peaks of TiO_2, after substrate signal subtraction, there is only the smear peak of VO_2 (*R*). (b) Resistivity as a function of temperature of 15-min deposited (12.7-13.6 nm) VO_2 on various substrates, the vertical solid line indicate T_{MIT} of bulk, the inset shows device image with Ti/Au top contacts and 10µm × 250µm VO_2 channel. (c) Resistivity as a function of temperature for various thicknesses of VO_2/(100) TiO_2, the inset shows the extended temperature measurement of the thinnest film with a transition at 433 K.

For the VO_2/TiO_2 samples, only the insulating-*R* phase was observed and there was no frequency shift at room temperature. The crystal structure of the substrate, i.e. the symmetry and the lattice parameters, plays an important role in determining the symmetry of the epitaxial films and the strains along different in-plane directions, hence only the *R*-phase VO_2 was observed for the TiO_2 substrates in the given thickness range. As a comparison, the free-standing nanobeams can adopt a crystal structure with a different symmetry (*M2*, *T*) to accommodate the applied mechanical strain. [37]

5.2.3 Transport properties

The devices used were simple current devices, fabricated via photolithography and electron beam evaporation (processing method is described in chapter 3). The optical image of the device is shown in figure 5.4(b) inset. Figure 5.4(b)-(c) summarizes the transport behavior of VO_2 deposited on TiO_2 and sapphire substrates. The transport behaviors of ~13 nm VO_2 deposited on various substrates are shown in figure 5.4(b). The film deposited on (100) TiO_2 has the highest T_{MST} ~358 K, while the film on (0001) Al_2O_3 has a T_{MST} ~332 K, the film on (011) TiO_2 has a T_{MST}~321 K and the film on (001) TiO_2 has the lowest T_{MST} ~ 305 K. A similar shift was explained using the strain from the TiO_2 substrate in a previous report.[40] In this current experiment, a systematic study of the thickness dependence of T_{MST} on various substrates is reported. The objective of this study is to further understand how to control the strain using different film thicknesses. The resistivity as a function of temperature for various thicknesses of VO_2 grown on (100) TiO_2 are shown in figure 5.4(c). As the films get thinner, or more strained, the T_{MST} shifts to higher temperature. The 4.9 nm film has an unusually high T_{MST} (~ 433 K) as seen in figure 5.4(c) inset.

Figure 5.5 shows resistivity as a function of temperature for samples with different thicknesses on all substrates and the possible two-phase temperature range is highlighted. The T_{MST} were determined from resistivity as a function of temperature measurements on all films. All the TiO_2 samples preserved the resistivity ratio during the transition very well, approximately 3-4 orders of magnitude change in resistivity, while the *c*-Al_2O_3 samples experienced great suppression of the resistivity ratio as the films get thinner as shown in figure 5.5. This due to the fact that the films grown on *c*-Al_2O_3 substrates are not epitaxial, since the crystal structure of the substrate is hexagonal, and the crystal structure of VO_2 is monoclinic (as shown in figure 5.5(a) inset). The different crystal structures together with the large lattice mismatch results in poorer VO_2 crystallinity as compared to the epitaxial VO_2 grown on the TiO_2 substrates.

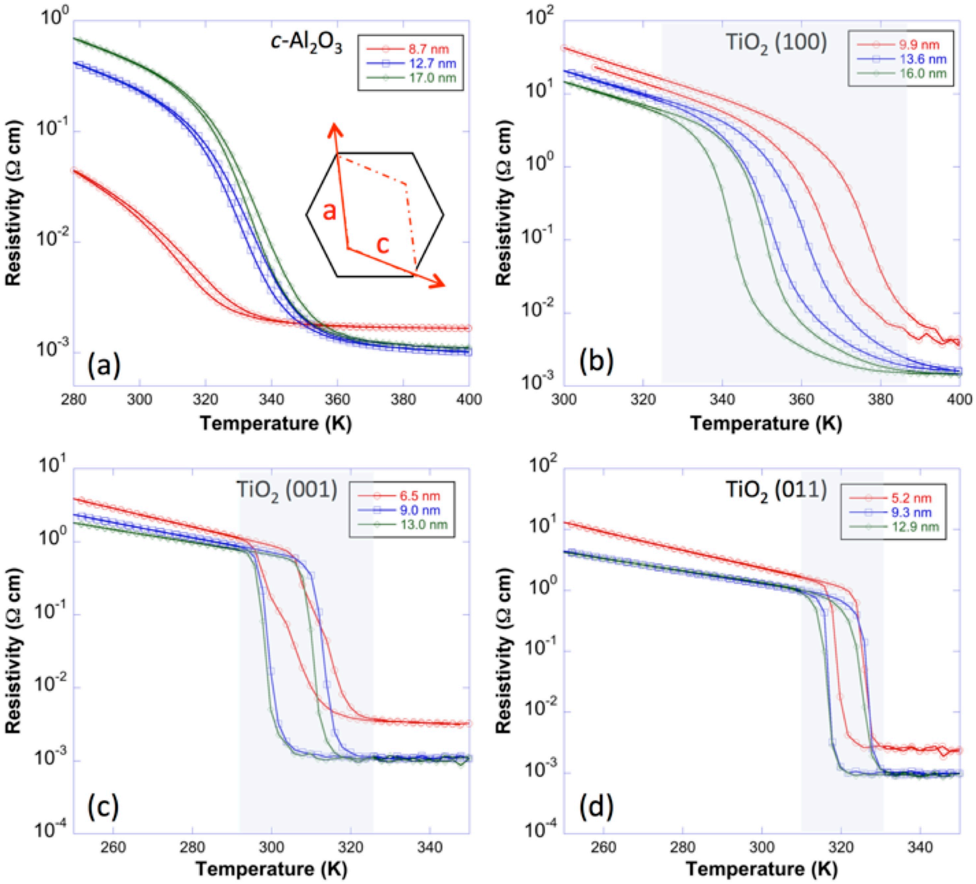

Figure 5.5 (a)-(d) Resistivity as a function of temperature for various thickness VO_2 deposited on *c*-Al_2O_3, (100), (001), and (011) TiO_2 respectively, inset showing the monoclinic structure of VO_2 (red dashed line) on top of the hexagonal crystal structure of *c*-Al_2O_3 (black solid line), the highlighted area showing a possible two phase region.

The films on the (100) TiO_2 substrates have the largest strain, resulting in the highest T_{MST}, while the films on the (001) TiO_2 substrates have the smallest strain, and the lowest T_{MST}. Because they are the most strained films, the VO_2/(100) TiO_2 samples experience the largest shift in T_{MST} as the thickness varies. On the other hand, thickness has the smallest effect on the *c*-strain and the T_{MST} for the (011) and (001) samples. This is because the *c*-mismatch is much larger than the *a*-mismatch, hence the (100) samples get the largest (in-plane) strain from the substrate clamping effect, and can relax much faster than the (011) and the (001) samples. The (011) samples and the (001) samples show much sharper transitions than the (100) or the *c*-Al_2O_3 samples since they are less strained and have better crystallinity. It is likely that the surface scattering plays an important role as the films get thinner: the resistivity in the metallic phase is higher than for the thicker films, as seen in figure 5.5, because the thickness of the film is less than an estimated mean free path of 7.3 nm using Fuchs–Sondheimer model [82]. Interestingly, the 6.5 nm (001) film also shows a two-step transition, suggesting multiple phases with different transition temperatures, while this is not the case for the (011) film deposited using the same conditions. The T_{MST} can be modified in a wide range from 300 - 440 K, via strain manipulation by both substrate choice and thickness, enhancing the useful temperature range of the MST for potential applications.

5.2.4 Phase diagram for bi-axially strained VO_2

A phase diagram is proposed in figure 5.6 for the bi-axially strained VO_2. It shows the regimes of the metallic phase, the semiconductor phase, and the region of coexistence of the rutile phases (two phase). The two-phase area is based on hysteresis loop and anisotropy of the transport data collected from previous reports. [43-45,83] In this phase diagram, the T_{MST} shows a rather linear relationship with the *c*-axis strain that is in good agreement with a previous report. [40] It is worthy noting that the lattice parameter *c* in Muraoka's report was calculated assuming the volume of the unit cell was conserved. In this study, the lattice parameters were directly determined from XRD 2θ scans.

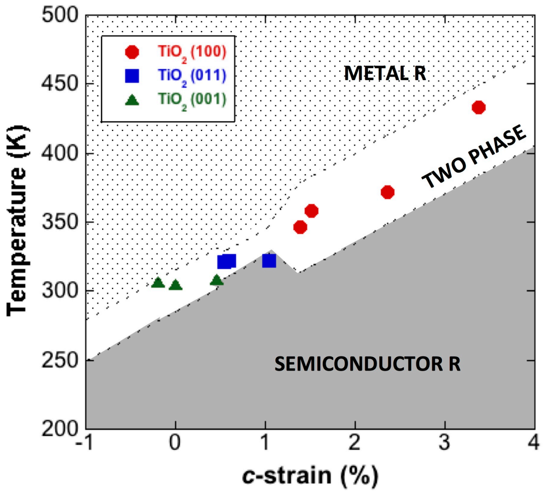

Figure 5.6 Phase diagram of rutile VO_2 assembled from data on T_{MIT} as a function of uniaxial *c*-strain; hysteresis loop; and transport anisotropy of VO_2 deposited on various TiO_2 substrates. For the clamped VO_2 thin films, the *rutile* phase can accommodate both metallic and semiconducting states.

This new phase diagram extracted from the experimental data confirms the predictions of cluster Dynamical Mean Field Theory (cDMFT). This theory investigates the effect of the epitaxial strain on the electronic structure of rutile VO_2 [41]. Indeed, these predictions of the strain dependence of the $d_{||}$ state were confirmed by Laverock *et al.* [72] Furthermore, these cDMFT calculations [41] demonstrated the effect of strain on electronic structure of VO_2, as shown in figure 5.7. Considering metallic state, a tensile strain along the *c*-axis [001] results in a longer V-V bond and reduces the splitting of bonding-antibonding states ($d_{||}$ bands). As a result, the $d_{||}$ band is narrowed. In a single crystal, the tensile strain along [001] also leads to a compressive strain in the *ab*-plane, resulting in shorter V-O bond and an upward shift in the position of the d_π band. This results in an increase of the insulating band gap which opens between the lower $d_{||}$ and d_π levels. The energy increase of the d_π electrons reduces the screening of electrons in the $d_{||}$ band, thus enhancing the effect of correlations. [84]

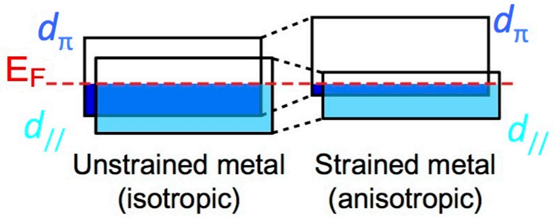

Figure 5.7 Effect of tensile strain along c_r on the electronic structure of metallic VO_2: antibonding d_π bands are shifted upwards while the $d_{||}$ band is narrowed. [43]

Not only does it show that the rutile phase can stabilize both metallic and insulating states, but it also predicts that the coexistence of both insulating and metallic phases for large values of the on-site Coulomb interaction potential (*U*). Experimentally, photoemission spectroscopy on bi-axially strained VO_2 on TiO_2 substrates showed a weak insulating gap as well as the suppression of orbital redistribution across the transition that lead to a conclusion of a more Mott-like MIT with the absence of a structural distortion, i.e. Peierls transition. [42] In highly strained epitaxial films (with thicknesses much larger than what are reported here), an intriguing unidirectional stripe state was observed with mixed metallic and insulating phases via scattering-type scanning near-field optical microscopy, [45] serving as strong evidence for the coexistence of insulating and metallic rutile phases.

5.3 Anisotropy in electrical conductivity

In this study, VO_2 thin films were deposited on (100) TiO_2 single-crystal substrates using reactive target biased ion beam deposition for 60 minutes with the conditions listed in table 5.5. The film thicknesses were all about 100 nm. The transport properties along [010] and [001] of the rutile VO_2 were measured. The carrier density and mobility were calculated from the Hall resistance and dc conductivity in the temperature range from 300 to 400 K.

Table 5.5 Growth parameters of VO_2/(100) TiO_2

GROWTH PARAMETERS	S-1
Negative Bias Voltage (kV)	0.90
Negative Bias Current (mA)	102
Positive Bias Voltage (V)	20.0
Positive Bias Current (A)	0.51
Cathode Ar Flow (sccm)	10
Cathode Voltage (V)	6.3
Cathode Current (A)	7.06
Anode Ar Flow (sccm)	70
Anode Voltage (V)	36.7
Anode Current (A)	6.55
V Target Frequency (kHz)	71.43
V Target Positive Pulse Period (μs)	3
Ar/O_2 80/20 Flow (sccm)	5.0
Substrate Temperature (°C)	500
Process Pressure (mTorr)	1.3

5.3.1 Crystal structure and surface morphology characterizations

XRD showed that the VO_2 films grew epitaxially on the (100) TiO_2 single-crystal substrates. The out-of-plane 2θ scan on one of the films [figure 5.8(a)] shows that the (200) peak in the VO_2 diffraction is coupled to the (200) peak of the TiO_2 substrate, and the VO_2 peak was the only peak detected in a wide-range 2θ scan (not shown here). This information indicates that there are no secondary phases in the film. The in-plane azimuthal scans (ϕ) of the (110) peaks of VO_2 and TiO_2, as shown in figure 5.8(b), confirm the epitaxy of the film with $(100)_{VO_2} \parallel (100)_{TiO_2}$ and $(010)_{VO_2} \parallel (010)_{TiO_2}$. It also shows that VO_2 is tetragonal at room temperature, which is likely due to the substrate clamping effect. The [010] and [001] in-plane directions were identified using XRD in-plane ϕ scans. The directions were later used to orient Hall bar devices.

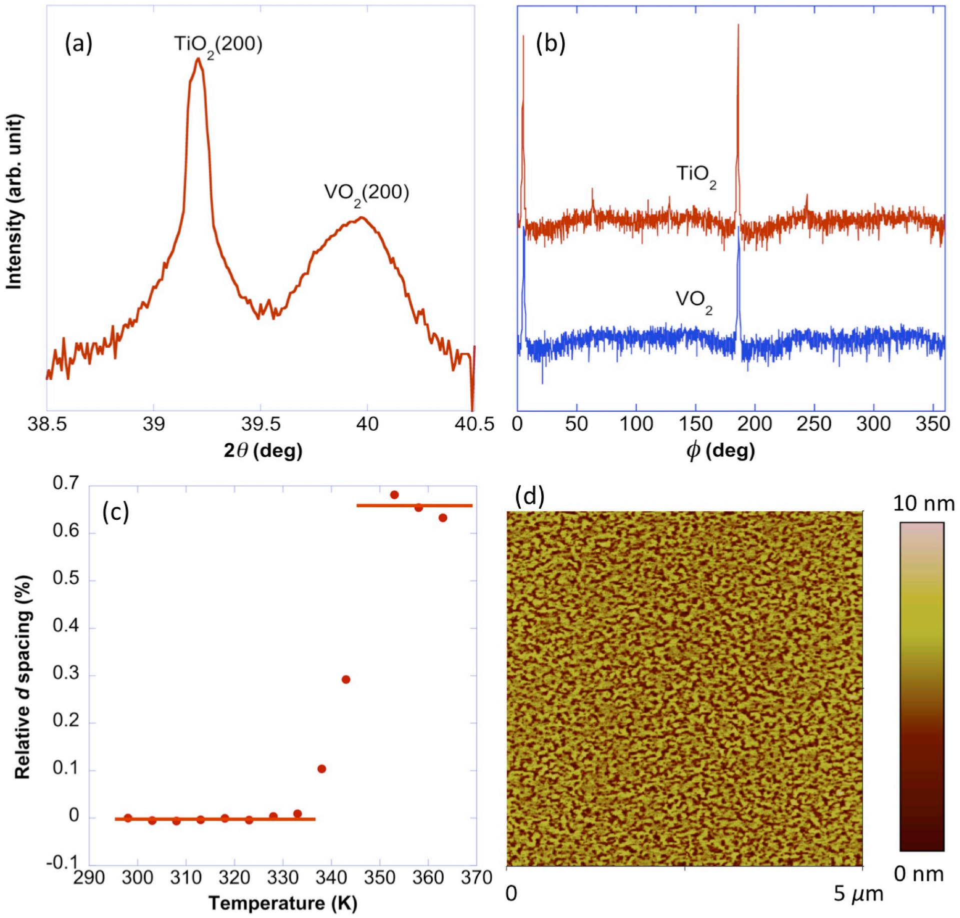

Figure 5.8 (a) Room-temperature XRD data of (200) TiO_2 and (200) VO_2. (b) ϕ scans of (110) TiO_2 and (110) VO_2. (c) Temperature-dependent XRD data showing a 0.65% step like increase in (100) spacing, at T_{MST} = 340 K. Relative d spacing = $(d-d_{300K})/d_{300K}$. (d) AFM image of 5 μm by 5 μm (100) VO_2 surface. The rms roughness is 1.5 nm.

From the values of 2θ, the (100) spacing of rutile VO_2 was estimated to be 4.5121 Å, the (010) spacing was 4.5109 Å, and the (001) spacing was 2.9076 Å (obtained by assuming volume conservation of the unit cell). The estimated spacings indicate that the film underwent a moderate compressive strain of -0.93% along [100] and [010] directions, and a large tensile strain of 1.92% along [001]. Since the (001) spacing was obtained by volume conservation, the magnitude of the strain estimated is qualitative, but the sign of the strain remains true. The strain was due to the epitaxial strain arising from the lattice mismatch between rutile VO_2 and TiO_2 (a = 4.5936 Å and c = 2.9582 Å).

Temperature-dependent XRD results on a different film grown under the same conditions [figure 5.8(c)] show a small (100) spacing expansion, ~0.65%, occuring at T_{MST} = 340 K with increasing temperature. This value can be compared to that of bulk VO_2 (0.6-0.8%). [71,85] Figure 5.8(d) is an AFM image of a (100) VO_2 film surface over an area of 5 μm by 5 μm. The film surface was very smooth with the root-mean-square (rms) roughness of 1.5 nm. There were no pin holes or cracks observed; thus, the influence of these defects on the transport properties can be ruled out.

5.3.2 Transport properties

(a) Hall bar structures

Two Hall bar devices were fabricated and oriented in directions perpendicular to each other, with one parallel to [001] and the other being parallel to [010] of the substrate as shown in figure 5.9. The Hall bar was patterned by photolithography and the film outside the pattern was etched via RIE+ICP. The width is 5 μm and the spacing between contacts along the bar is 50 μm. The Ohmic contact was 200 nm Au / 20 nm Ti, deposited by electron beam evaporation. More detail about device fabrication process is included in chapter 3.

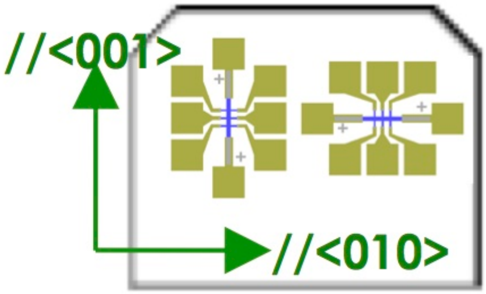

Figure 5.9 Schematic for Hall bar devices oriented perpendicular to each other.

(b) Metal-semiconductor transition

Figure 5.10(a) shows the dc conductivity of the VO_2 film as function of temperature measured along [010] and [001]. At room temperature, the conductivity along [010] was found to be 1.04 S/cm, and along [001] it was found to be 43.22 S/cm. Therefore, the anisotropy ratio $\sigma_{[001]}/\sigma_{[010]}$ was 41.5, which is significantly larger than that of bulk VO_2 which has an anisotropy ratio around 2. The ratio of 41.5 is the largest among those previously reported. [86-89] The conductivity anisotropy persists through the metal semiconductor transition. It was surprising that two distinct transition temperatures (defined by the midpoint of the transition) were found at 336.8 and 339.3 K for the [010] and the [001] Hall bars, respectively. The conductivity measurements were repeated using different heating/cooling rates from 2-5 K/min, all measurements yielded the same transition temperatures. It is suspected that the difference in the transition temperature likely dues to the co-existence of both metallic and semiconducting phases [45].

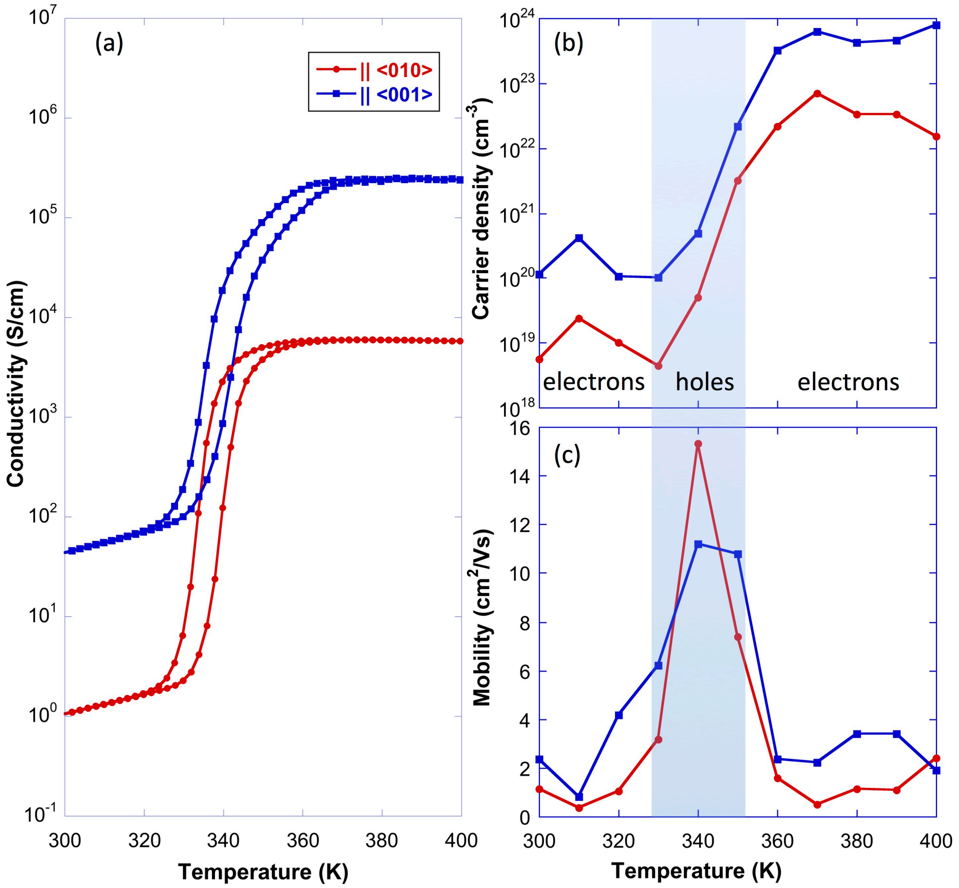

Figure 5.10 (a) DC conductivity, (b) carrier density, and (c) mobility as functions of temperature of a VO_2 film grown on a (100) TiO_2 substrate measured parallel and perpendicular to the [001] of rutile VO_2, respectively. The majority carriers were electrons everywhere except between 330-350 K where the majority carriers were holes.

(c) Carrier density and mobility

To further investigate the influence of the transport anisotropy, I calculated the carrier density and mobility as functions of temperature using the Hall effect measurement and dc conductivity; the carrier density and mobility are plotted in figure 5.10(b) and 5.10(c), respectively. There was a large anisotropy in the effective carrier density but a very small anisotropy in the mobility. Note that the carrier density was extracted using the assumption of a free electron model that does not take into account either the effective mass of the carriers or the possibility of multiple bands of carriers. Table 5.6 summarizes the transport properties of two Hall bars, one along [010] and the other along [001]. The results presented in the table show that the Hall bar along [001] has a higher conductivity, a higher carrier concentration, and a higher mobility than the Hall bar along [010]. Electrons were found to be the majority carriers on both sides of the transition, except that the majority carriers switched to holes in the vicinity of the transition temperature around 330 to 350 K.

Table 5.6 Comparison of transport properties of [010] and [001] Hall bar.

	// [010]	**// [001]**
T_{MST} (K)	336.8	339.3
Conductivity at 300 K (S/cm)	1.04	43.22
Conductivity at 400 K (S/cm)	5.81×10^{3}	2.41×10^{5}
Carrier density below MST (cm^{-3})	1.09×10^{19}	1.85×10^{20}
Carrier density above MST (cm^{-3})	3.49×10^{22}	5.23×10^{23}
Mobility below MST ($cm^2/(V{\cdot}s)$)	1.43	3.38
Mobility above MST ($cm^2/(V{\cdot}s)$)	1.35	2.65

The carrier density anisotropy ratio $n_{[001]}/n_{[010]}$ was ~17 below T_{MST}. Above T_{MST}, the anisotropy ratio $n_{[001]}/n_{[010]}$ was ~15. For both the [010] and the [001] directions, the carrier density increased by 3 orders during the transition. For the Hall bar parallel to [010], the mobility calculated was ~1.43 $cm^2/(V{\cdot}s)$ below T_{MST} and ~1.35 $cm^2/(V{\cdot}s)$ above T_{MST}. For the Hall bar parallel to [001], the mobility was slightly larger with an approximate value of 3.38 $cm^2/(V{\cdot}s)$ below T_{MST} and ~2.65 $cm^2/(V{\cdot}s)$ above T_{MST}. Figure 5.11 shows Hall resistance as a function of the external magnetic field measured along [010] and [001] at 320 K, 350 K and 400 K, respectively. After extracting the Hall resistance from the measured voltage using the method described in chapter 3, there was small magnetoresistance ΔR/R of 0.2 % at room temperature and 0.05% at 400 K extracted for magnetic fields in the range of -7 T to +7 T, larger than the magnetoresistance reported by Ruzmetov *et al*. [28]

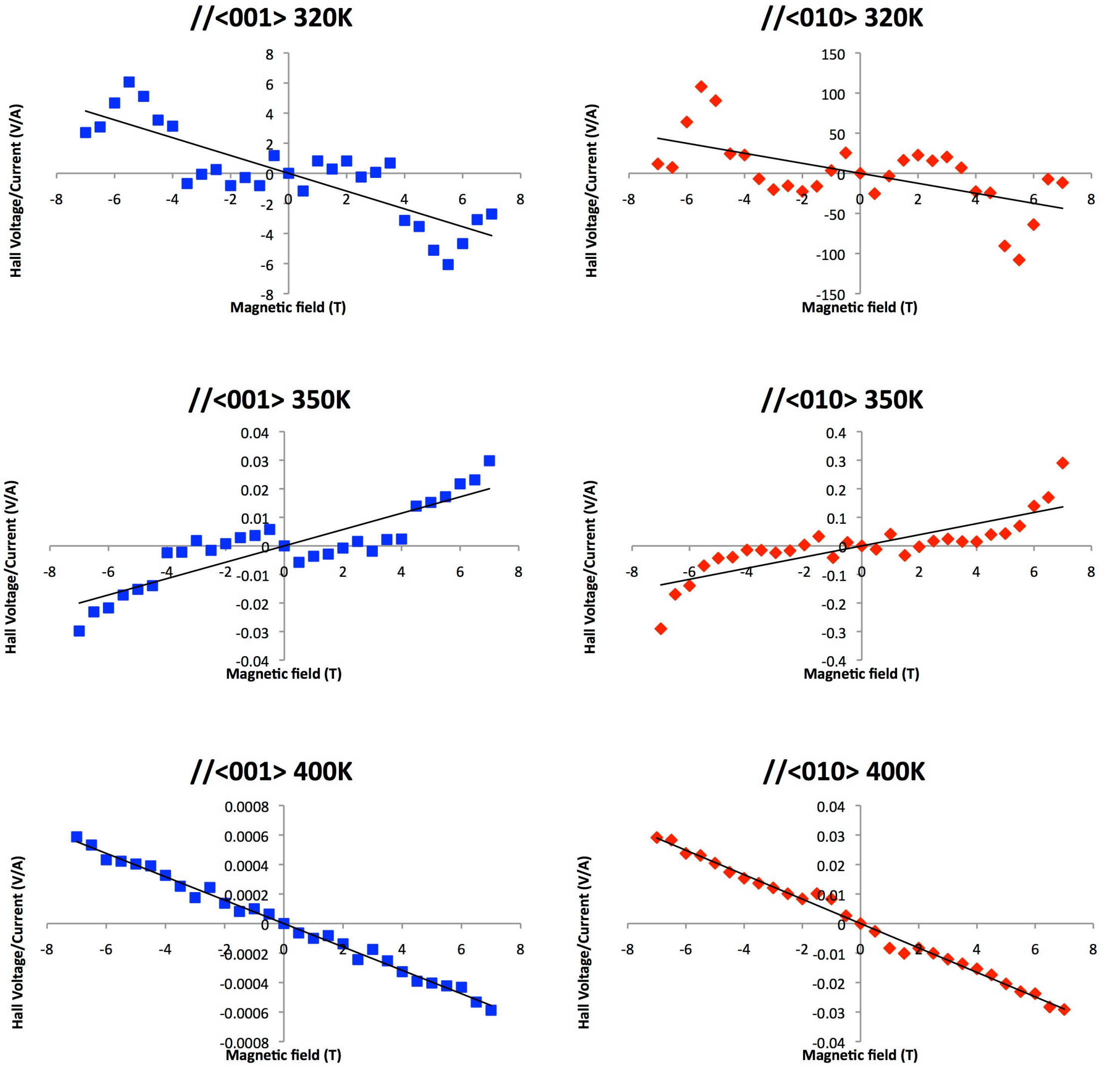

Figure 5.11 Hall resistance as a function of the external magnetic field measured along [010] and [001] at 320 K, 350 K and 400 K, respectively. Negative slope indicates electrons as majority carrier, and positive slope indicates holes.

Strikingly, there was a spike (maximum) in the mobility in both directions around the MST, which is ~10 times larger than the mobility both below and above T_{MST}. Recently, Ruzmetov *et al.* [28] have reported the same trend of mobility in VO_2 thin films grown on *c*-plane Al_2O_3 substrates. Instead of the upward spike, Ruzmetov *et al.* found that around the MST, there was a drop (downward spike) which was ten times smaller than the mobility both below and above T_{MST}. In order to confirm that the abrupt spike around MST was not an artifact of the measurements, Hall measurements were repeated using a Quantum Design Versalab system instead of the Quantum Design PPMS, and the maximum in the mobility still appeared.

5.3.3 Discussion

The carrier concentration in metallic VO_2 was estimated to be 3.4×10^{22} cm^{-3}, assuming one electron per vanadium ion. In this case, the measured carrier density in the metallic phase of the [010] bar corresponds to 1.03 itinerant carriers per vanadium ion, while the carrier density in the metallic phase of the [001] bar corresponds to 15.47 itinerant carriers per vanadium ion. The result of the [001] bar was larger than that in previous reports of 3.3 itinerant carriers per vanadium ion for bulk single-crystal VO_2 [12] and 4.7 for VO_2 thin films on *c*-plane Al_2O_3 substrate.[28] The fact that there appears to be more than one itinerant carrier per vanadium ion has been observed in single-crystal VO_2. [90] The multiple itinerant carriers can also be explained using the electronic structures of the metallic phase. According to Goodenough [18], the conduction along the *c*-axis in the metallic phase is in two overlapping vanadium d-bands. Such overlapping d-bands as opposed to the one-band-spherical-Fermi-surface model could produce a number of itinerant electrons per vanadium larger than one electron per V^{4+} ($3d^1$). [90] Since the conduction along the [010] direction is due to oxygen 2p orbital participation in the band formation, it is significantly different than conduction in the [001] direction. Below the $T_{MST,}$ conduction electrons are trapped between pairs of cations along the *c*-axis. Therefore a conduction anisotropy is expected. The fact that the thin film is highly strained may also enhance the anisotropy.

The anisotropy in both conductivity and effective carrier density in VO_2 were surprisingly large. In the light of phase separation, this most likely results from a strong anisotropy in the effective masses of carriers, which was observed, for example, in the organic superconductor κ-$(BEDT\text{-}TTF)_2Cu(NCS)_2$. [91] One can also speculate that the large conductivity anisotropy can also be attributed to the multiple Fermi surfaces, each containing its own carriers and with anisotropic effective masses as exemplified in the *ab*-plane of the high T_C superconductor $YBa_2Cu_3O_{7-\delta}$ [92] . In this material, the conductivity anisotropy was due to two separate Fermi surfaces: one from the Cu-O planes and the other from the Cu-O chains. Though VO_2 lacks a complicated crystal structure like the cuprates, the dispersion of the O *2p* band was observed in Angle Resolved Photoemission Spectroscopy [93], indicating various Fermi surfaces along the *a*-direction versus the *c*-direction in rutile VO_2.

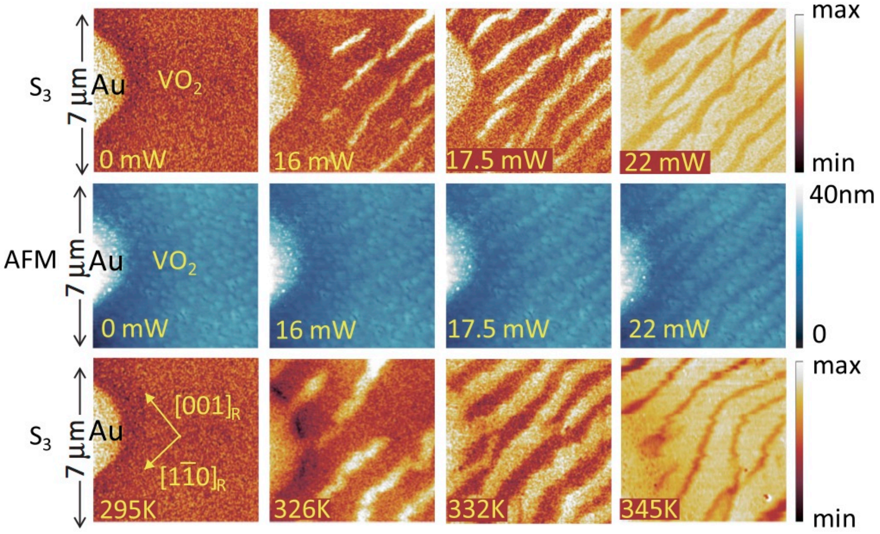

Figure 5.12 Top row: IR scattering amplitude S_3 recorded at distinct power levels of the pump laser. Middle row: sample topography (AFM) for the images displayed in the top row. Bottom row: S_3 images recorded at distinct temperatures. The near-field signal in all images is normalized to that from a 50 nm gold film (middle left of each image). [45]

Another study using nanoscale infrared spectroscopy [45] revealed the origin of a large anisotropy in the transition region for VO_2 thin films deposited on a (110) TiO_2 substrate: epitaxial films under bi-axial strain demonstrated a very pronounced anisotropy in optical and transport properties, [43,44] as a result of the formation of unidirectional stripe states in which the semiconducting and metallic states coexisted as shown in figure 5.12. [45] The higher epitaxial strain along the *c*-axis has been found to promote nucleation of local metallic regions below the transition temperature. [45,94] Even though the overall strain along the *c*-axis is tensile, the local strain near the metallic nucleation was found to be highly compressive, creating a tensile-compressive-tensile strain environment that leads to the nucleation of the stripe state. It is also found that the metallic stripes were nucleated at the film/substrate interface where the epitaxial strain is the strongest. [94] These metal-semiconductor-metal stripes have rutile-monoclinic-rutile structural variation introducing the conductivity, compared to the [010] direction, parallel with the stripe pattern.

As the metallic stripes begin to form (perpendicular to *c*-axis), the conductivity measured along the direction of the stripes will start to increase sooner due to the high resistance of the insulating areas in parallel with the low resistance of the metallic areas. The conductivity measured along the *c*-axis (perpendicular to the stripes), where the high and low resistance areas are in series, will start to increase later. This results in a difference in the T_{MST}. The T_{MST} reported here are very closed to each other because the metallic stripes found on VO_2 / (100) TiO_2 are not perfectly perpendicular to the *c*-axis, but rather make a ±57° angle to the *c*-axis as show in figure 5.13 due to relaxation of very thick film [94]. This may also be the case for the etched hall bars where the substrate clamping is reduced (compared to continuous thin film). The extremely high conductivity along [001] is likely due to the “cracks” along [001] forming from the relaxation and creating a “short path” where metallic stripes from two regions merge, as shown in figure 5.13.

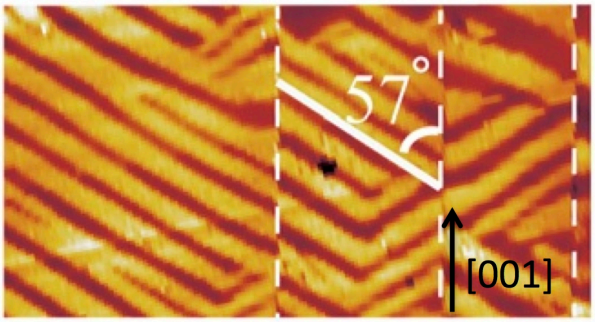

Figure 5.13. Pump near-field infrared spectroscopy, showing simultaneously acquired near-field S3 with 18.8 mW pump excitation on VO_2/TiO_2 (100). [94]

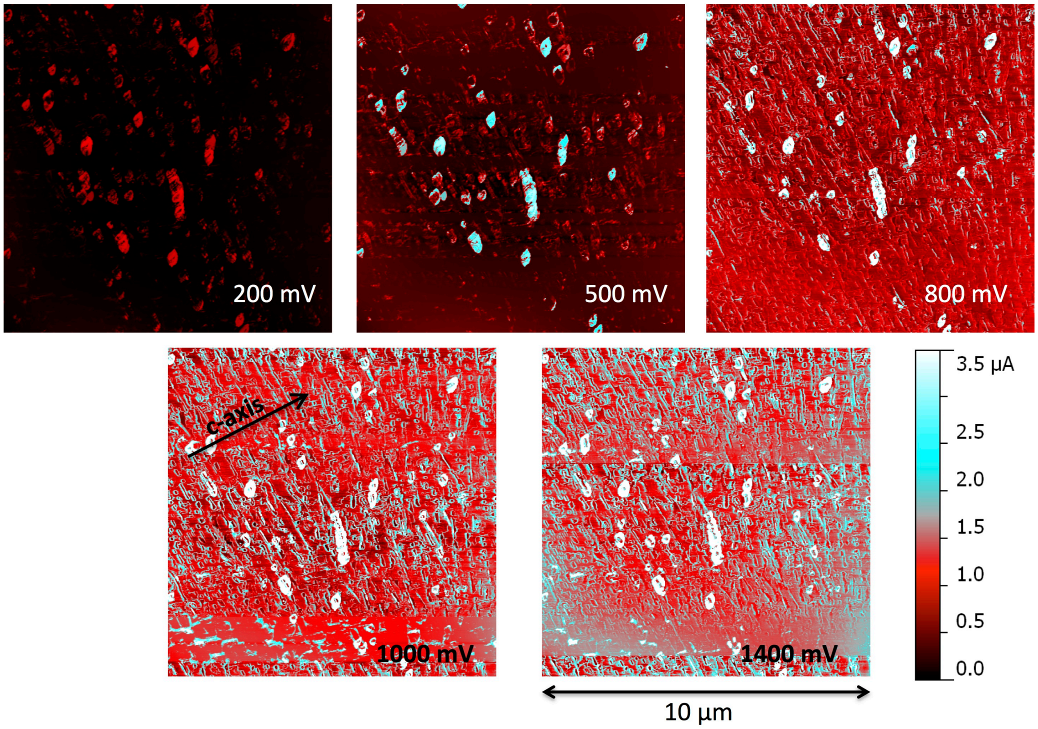

Figure 5.14 Conductivity mapping of 300 nm VO_2/(110) TiO_2 via conductive AFM, with the different bias voltage from 200-1400 mV, showing conductive stripes perpendicular to *c*-axis.

In addition, conductive AFM measurements on VO_2 thin films deposited on (110) TiO_2 also unveiled the same stripe pattern, but in this case the stripes are local since the sample was locally biased at different bias voltage as the current was read back during each scan. The result is shown in figure 5.14. The conductive stripes (perpendicular to the *c*-axis) are getting larger as the applied bias voltage get larger.

5.4 Summary

The properties of single-phase strained VO_2 thin films were studied on various single crystal substrates. Raman spectra showed that epitaxial VO_2 films grown on TiO_2 single crystal substrates were the rutile phase in both the insulating state and metallic state despite various orientations, instead of the *M1* state observed on *c*-plane sapphire. The strained VO_2 undergoes an electronic phase transition without the Peierls transition as observed in single crystal and polycrystalline VO_2. A new phase diagram of bi-axially strained VO_2 was proposed in which only the rutile VO_2 is presented. Secondly, a large increase in T_{MST} up to 433 K was observed for VO_2/(100) TiO_2. This increase is much higher than any previous report. In contrast, the T_{MST} of VO_2/(001) TiO_2 was reduced to 305 K and the large change in resistivity of 3-4 orders of magnitude was preserved. The ability to tune the T_{MST} using strain engineering that has been demonstrated in this work extends the potential temperature range for the use of VO_2 in nanoelectric devices.

Moreover, a very large anisotropy in the dc conductivity of epitaxial VO_2 thin films deposited on a single-crystal (100) TiO_2 substrate was discovered. A conductivity mapping of VO_2 thin films also revealed the co-existing stripe states, leading to the anisotropy for both optical and transport properties. The in-plane conductivity was measured along the [010] and [001] directions of VO_2, and it was found that the conductivity anisotropy ratio $\sigma_{[001]}/\sigma_{[010]}$ was 41.5 at 300 K, much larger than that of single-crystal VO_2. The conductivity along [001] in the metallic phase was unusually high ~2.4×10^5 S/cm, and is comparable to a very good conductor. The very low resistivity of the VO_2 film, especially along [001], can be a significant benefit for low power electronic devices.

CHAPTER 6. Doping effects on vanadium dioxide films

6.1 Introduction

This chapter discusses chemical doping with isovalent Mn^{4+} and aliovalent Al^{3+} in VO_2 thin films and the effect of doping on microstructures and properties. Two approaches for doping during the synthesis were used; it was found that different doping methods – taking advantage of the flexibility of RBTIBD – yield extremely distinctive results in both the microstructures and characteristics of the MST, namely the size of the resistive jump. One doping method enhances the MST while the other degrades the film microstructures and highly suppresses the MST. The doping technique I developed here results in a better crystallinity of the doped films compared to other doping methods explored [35,36,95,96]. The technique used can also be controlled with dopant increments of about of 0.1%.

The effect of Al-doped VO_2 on the MST was explored in comparison with the effect of isovalent Mn^{4+} doping. Both Al^{3+} and Mn^{4+} have about the same effective ionic radius, 53.5 and 53.0 pm, respectively [97], thus it is expected that the distortions caused by their substitutions would be equivalent. The change in transport properties would arise mostly from the difference in the valence states of these two dopants. Doping with Al^{3+} is likely to introduce holes into the conduction band of VO_2. The evidence for hole doping by Al^{3+} is provided by Hall effect measurements. This evidence has not been reported previously. Both types of dopants were found to greatly increase the resistance ratio and enhance the MST, which was rarely observed in any other reports. As the T_{MST} is modified, it often is accompanied with a suppressed transition. [7,35,36]

6.2 Experimental

Using the RBTIBD method, sputtering occurs during the negative pulse bias that exceeds the sputtering threshold for the target materials. Hence the amount of material sputtered from the target is directly associated with the negative pulse width and the pulse frequency, i.e. the duration for the negative biasing of the target. I hypothesized that the rate of sputtered metal is then linearly proportional to both negative pulse width (w) and frequency (f): $metal\ amount \propto w \times f$, where $w = \frac{1}{f} - positive\ pulse\ width.$

Before each set of depositions, two samples were deposited for deposition rate calibration and to estimate w and f of the dopant target for various dopant concentrations. The first sample was a pure VO_2 thin film and the second sample was the oxide of the desired dopant. They were deposited under the same conditions with 71.43 kHz and 3 μs positive pulse width (~ 11 μs negative pulse width). The nominal percentage of dopant (%) was estimated by

$$\%\, nom. = \frac{r_d}{r_{vo_2} + r_d} \times \frac{f \times w}{71.43 \times 11} \times 100\% \tag{6.1}$$

where r_{vo_2} and r_d are the deposition rate (nm/hour) of VO_2 and the oxide of dopant respectively. Hence the estimated concentration is not the same as atomic percentage, where the density and the molecular mass of the oxide materials need to be taken into account. Therefore the nominal percentage estimated by this method may not be sufficient enough to compare different dopants but it is sufficient enough to semi-quantitatively compare results associated with the same type of dopant.

The oxides of Mn and Al were confirmed with XRD to be MnO_2 and Al_2O_3, respectively. To convert the estimated % nom. to % atomic, each deposition rate should be multiplied by a correction factor, $\frac{\#\, metal\ ions}{molecule} \times \frac{density\ (g\ cm^{-3})}{Molar\ mass\ (g\ mol^{-1})}$. The correction factor for VO_2, MnO_2, and Al_2O_3 are 0.055, 0.058, and 0.077 respectively. The deposition rates of VO_2, MnO_2, and Al_2O_3 were 50, 80, and 144 nm/hour. In other words, the deposition rate ratio term in equation 6.1 needs to be corrected. After applying the correction factor to the deposition rates, the at. % of Mn is ~ 1.02 × % nom. Mn, and the at. % of Al is ~ 1.08 × % nom. Al. Therefore the % nom. is fairly sufficient to represent the at. % of Al and Mn.

However as the metal ions of dopants are introduced along with the V^{4+} in the same oxygen atmosphere, the additional metal ions most likely introduce a donor-like oxygen deficiency; this is true for any metal ions introduced by the doping method used in these experiments.

There are 4 sets of samples investigated in this study:

A. Fixed frequency mode for Mn-doped VO_2 (1.56 kHz)
B. Variable frequency mode for Mn-doped VO_2
C. Mn^{4+} doped at 1.00 kHz
D. Al^{3+} doped at 1.00 kHz

All the samples were deposited for 60 minutes, resulting in ~50 nm thick films. The growth parameters are listed in tables below:

Table 6.1 Growth conditions with calculated % doping for sample set A

GROWTH PARAMETERS	A1	A2	A3	A4	A5
Negative Bias Voltage (kV)	0.90	0.90	0.90	0.90	0.90
Negative Bias Current (mA)	102	105	107	106	107
Positive Bias Voltage (V)	20.0	20.0	20.0	20.0	20.0
Cathode Ar Flow (sccm)	10	10	10	10	10
Cathode Voltage (V)	7.0	4.3	5.2	5.1	4.8
Cathode Current (A)	7.06	7.06	7.06	7.06	7.06
Anode Ar Flow (sccm)	70	70	70	70	70
Anode Voltage (V)	36.1	38.4	38.0	38.4	38.6
Anode Current (A)	6.55	6.55	6.55	6.55	6.55
V Target Frequency (kHz)	71.43	71.43	71.43	71.43	71.43
V Negative Pulse Period (µs)	11	11	11	11	11
Mn Target Frequency (kHz)	---	**1.56**	**1.56**	**1.56**	**1.56**
Mn Negative Pulse Period (µs)	---	**3**	**10**	**17**	**35**
Ar/O_2 80/20 Flow (sccm)	6.0	6.0	6.0	6.0	6.0
Substrate Temperature (°C)	500	500	500	500	500
Process Pressure (mTorr)	1.1	1.1	1.0	1.1	1.1
Calculated % doping	0%	1%	3%	5%	10%

Table 6.2 Growth conditions with calculated % doping for sample set B

GROWTH PARAMETERS	B1 (A1)	B2	B3	B4	B5
Negative Bias Voltage (kV)	0.90	0.90	0.90	0.90	0.90
Negative Bias Current (mA)	102	105	116	119	146
Positive Bias Voltage (V)	20.0	20.0	20.0	20.0	20.0
Cathode Ar Flow (sccm)	10	10	10	10	10
Cathode Voltage (V)	7.0	4.3	3.6	3.5	4.3
Cathode Current (A)	7.06	7.06	7.06	7.06	7.06
Anode Ar Flow (sccm)	70	70	70	70	70
Anode Voltage (V)	36.1	38.4	39.0	39.2	38.6
Anode Current (A)	6.55	6.55	6.55	6.55	6.55
V Target Frequency (kHz)	71.43	71.43	71.43	71.43	71.43
V Negative Pulse Period (µs)	11	11	11	11	11
Mn Target Frequency (kHz)	---	**1.56**	**8.47**	**18.18**	**41.67**
Mn Negative Pulse Period (µs)	---	**3**	**3**	**3**	**3**
Ar/O_2 80/20 Flow (sccm)	6.0	6.0	6.0	6.0	6.0
Substrate Temperature (°C)	500	500	500	500	500
Process Pressure (mTorr)	1.1	1.1	1.1	1.1	1.1
Calculated % doping	0%	1%	5%	10%	20%

Table 6.3 Growth conditions with calculated % doping for sample set C (Mn^{4+})

GROWTH PARAMETERS	C1	C2	C3	C4	C5
Negative Bias Volt. (kV)	0.90	0.90	0.90	0.90	0.90
Negative Bias Curr. (mA)	110	107	107	106	108
Positive Bias Voltage (V)	20.0	20.0	20.0	20.0	20.0
Cathode Ar Flow (sccm)	10	10	10	10	10
Cathode Voltage (V)	3.9	4.0	3.9	4.3	5.7
Cathode Current (A)	7.06	7.06	7.06	7.06	7.06
Anode Ar Flow (sccm)	70	70	70	70	70
Anode Voltage (V)	40.8	40.3	40.5	40.0	39.2
Anode Current (A)	6.55	6.55	6.55	6.55	6.55
V Target Freq. (kHz)	71.43	71.43	71.43	71.43	71.43
V Neg. Pulse Period (µs)	11	11	11	11	11
Mn Target Freq. (kHz)	1.00	1.00	1.00	1.00	1.00
Mn Neg. Pulse Period (µs)	**26**	**55**	**87**	**123**	**164**
Ar/O_2 80/20 Flow (sccm)	6.0	6.0	6.0	6.0	6.0
Subs. Temperature (°C)	500	500	500	500	500
Process Pressure (mTorr)	1.1	1.0	1.0	1.0	1.0
Calculated % doping	**5%**	**10%**	**15%**	**20%**	**25%**

Table 6.4 Growth conditions with calculated % doping for sample set D (Al^{3+})

GROWTH PARAMETERS	D1	D2	D3	D4
Negative Bias Volt. (kV)	0.90	0.90	0.90	0.90
Negative Bias Curr. (mA)	108	108	107	106
Positive Bias Voltage (V)	20.0	20.0	20.0	20.0
Cathode Ar Flow (sccm)	10	10	10	10
Cathode Voltage (V)	2.9	7.3	7.5	7.6
Cathode Current (A)	7.06	7.06	7.06	7.06
Anode Ar Flow (sccm)	70	70	70	70
Anode Voltage (V)	41.6	38.2	37.4	37.2
Anode Current (A)	6.55	6.55	6.55	6.55
V Target Freq. (kHz)	71.43	71.43	71.43	71.43
V Neg. Pulse Period (µs)	11	11	11	11
Al Target Freq. (kHz)	1.00	1.00	1.00	1.00
Al Neg. Pulse Period (µs)	**14**	**30**	**48**	**68**
Ar/O_2 80/20 Flow (sccm)	6.0	6.0	6.0	6.0
Subs. Temperature (°C)	500	500	500	500
Process Pressure (mTorr)	1.1	1.0	1.0	1.0
Calculated % doping	**5%**	**10%**	**15%**	**20%**

6.3 Doping of manganese

VO_2 thin films were doped with Mn^{4+} in two series: 1.56 kHz fixed frequency mode (set A) and variable pulse frequency mode (set B). The percentage of dopants was calculated and summarized in tables 6.1-6.2. A pure VO_2 thin film was also grown for reference.

The Mn^{4+} ion has a smaller effective ionic radius (53 pm) compared to that of V^{4+} (58 pm) [97]. Consequently, when a Mn^{4+} ion substitutes for the V^{4+} ion in a V-V pair (along c_r or a_m axis), the repulsive force between the Mn^{4+} and the paired V^{4+} ion in the nearest neighbor is reduced. The nearest neighbor V-V pair (in plane) will be less distorted, however the next nearest pair will be more distorted, and the next will be less distorted and so on. This creates a highly disordered in-plane lattice. In addition the out-of-plane lattice spacing at the point of substitution will likely to decrease due to the smaller ionic radius of Mn^{4+}, creating distortion, i.e. mosaicity. Moreover the substitution of Mn^{4+} will introduce extra electrons to the films, because Mn^{4+} has three 3*d* electrons, where V^{4+} has one 3*d* electron.

6.3.1 Crystal structure and surface morphology characterizations

Figure 6.1(a) shows wide range XRD, revealing a single-phase monoclinic structure except for the 20% doped sample deposited with fixed pulse width (using the variable frequency mode). For the highest doped sample (20%), there were extra peaks found, identified as the peaks of (022) Mn_2O_3 ~ 27°, (110) MnO_2 ~ 29°, and (400) Mn_5O_8 ~ 37°. This suggests that too many Mn ions were introduced, creating mixed phases. For all other films, the only peak shown is the peak of (020) monoclinic VO_2 coupling to the (0006) Al_2O_3 peak of the substrate.

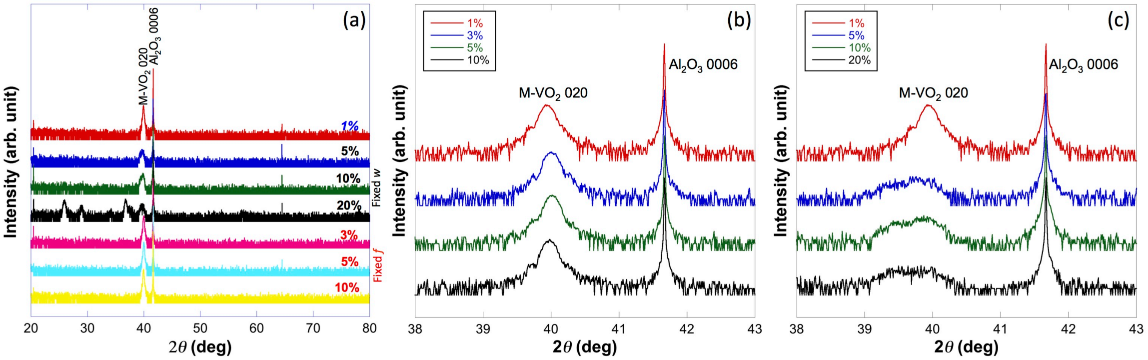

Figure 6.1 (a) XRD of sample set A and B showing single phase *M*-VO_2 except the 20%. A zoom-in of XRD around (020) *M*-VO_2 and substrate peak for (b) the samples doped with low fixed bias frequency (set A), and for (c) the samples doped with various frequencies (set B). The increase in frequency introduces dislocation and point defects, resulting in broaden film peak.

Figure 6.1(b) and (c) show the film peak coupling to substrate peak for the two modes. In the variable frequency mode set B [figure 6.1(c)], as the % Mn increases with increasing frequency, the film peak worsens: it decreases in intensity (peak height) and appears as a broadened peak with a sign of peak splitting. The worse intensity and the broadening peak indicate poorer crystallinity and inhomogeneity of the film in the out-of-plane direction, the plane perpendicular to substrate surface. The broadened peak, as shown in figure 6.1(c), is likely from the merging of two peaks, suggesting multiple crystal orientation growth. The results of set A with a low fixed frequency mode seem to be unchanged as the pulse width varies, as shown in figure 6.1(b).

The FWHM (full width half max) was extracted from Gaussian fits of the (020) *M*-VO_2 peak of doped films and summarized in table 6.5-6.6, where the FWHM of the undoped film was found to be ~ 0.114 deg. The broadening of the peak in doped VO_2 thin films is due in part to larger-scale flaws such as mosaicity, microstrain, and crystallite size.

For the sample set A which was doped at low fixed frequency (table 6.5), the FWHM stays constant at a low value of ~0.2 deg. However, it is almost twice as large as that of the undoped film. On the other hand, for the variable frequency set B (table 6.6), the FWHM increases drastically as the doping frequency increases (rising % Mn). For the samples in set B, the (020) *M*-VO_2 peak also shifts down as the Mn concentration increases (table 6.6), indicating a larger lattice parameter *b*. This behavior arises from the merging of peaks of multiple crystal orientations. In contrast, the film peak position for set A (the fixed pulse width mode) stays rather constant.

As Mn^{4+} ions substitute V^{4+} ions, there may be inhomogenous strain induced since the Mn^{4+} ions are introduced at different frequencies than V^{4+}, creating inhomogeneous out-of-plane spacings since not all planes get doped. This leads to an increase in the FWHM. However, the fast incorporation of dopants by high doping frequency changes the out-of-plane spacing more often, together with the random in-plane distortion of V-V pairs, likely resulting in the introduction of crystal defects such as dislocations and grain boundaries, and secondary phases that all contribute to the broadening of the peak and the increase in the FWHM. In other words, the higher doping frequency will likely to create more mosaicity.

Table 6.5 Summary of XRD *M*-VO_2 peak with FWHM and average grain size for set A: fixed frequency mode.

% Mn	FWHM (deg)	Peak position (deg)	Grain size (nm)
1	0.198	39.965	101
3	0.206	40.006	109
5	0.194	40.016	143
10	0.199	39.978	97

Table 6.6 Summary of XRD *M*-VO_2 peak with FWHM and average grain size for set B: variable frequency mode.

% Mn	FWHM (deg)	Peak position (deg)	Grain size (nm)
1	0.198	39.965	101
5	0.677	39.730	106
10	0.691	39.787	149
20	0.847	39.684	243

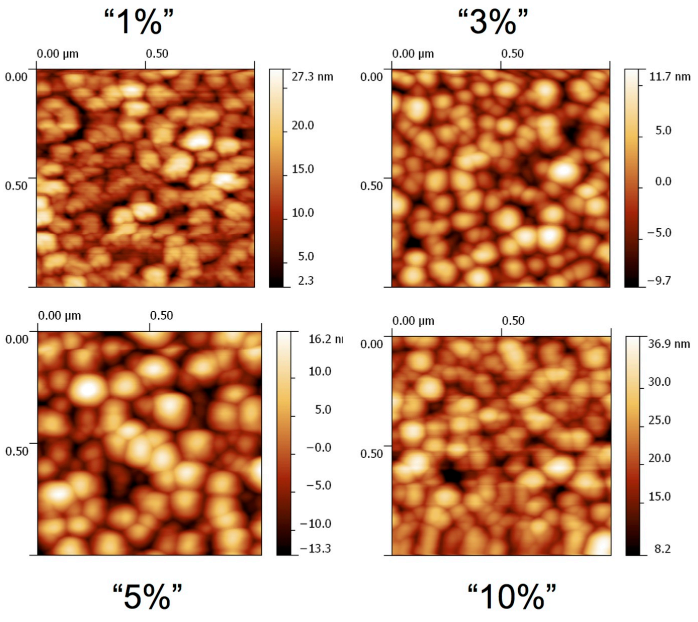

Figure 6.2 1×1 µm^2 AFM images of sample set A for the fixed frequency depositions, showing roughly the same size grains except the 5% sample

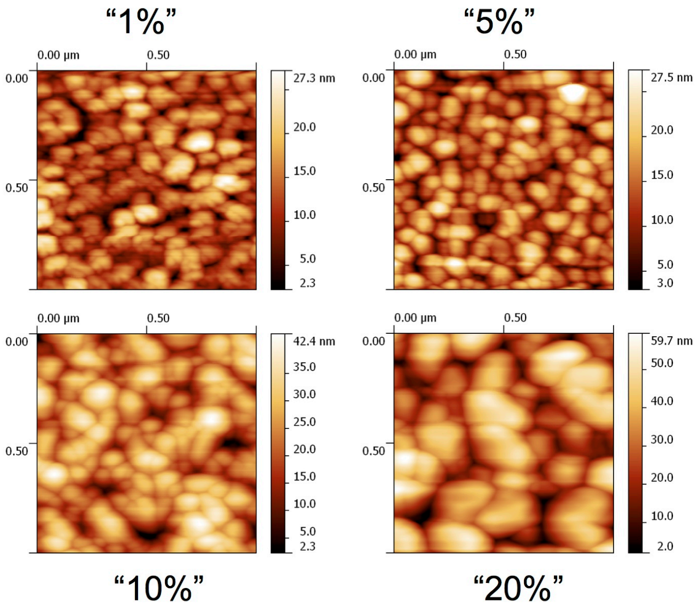

Figure 6.3 1×1 μm^2 AFM images of sample set B for the variable frequency depositions, revealing worse surface morphology (higher rms roughness and also larger grains) for the high frequency depositions.

AFM images reveal that the samples deposited at higher frequency (set B) have worse surface morphology with larger grains (figure 6.3), while doping at low fixed frequency (set A) did not have obvious effect on the morphology (figure 6.2); the average grain sizes of these samples are summarized in table 6.5-6.6. The root mean square (rms) roughness also increases drastically as the bias frequency increases, which is likely due to the large grain size.

The structure of the grain boundary depends on the misorientation of the crystal grains that it separates. For a system with small misorientation, the boundary will look like the boundary of the undoped films. As the misorientation gets larger, the boundary structure/shape is more complicated. The larger grain size is also likely due to more Mn incorporated into the film lattice that introduces more dislocation from interstitial defects.

6.3.2 Metal-semiconductor transition

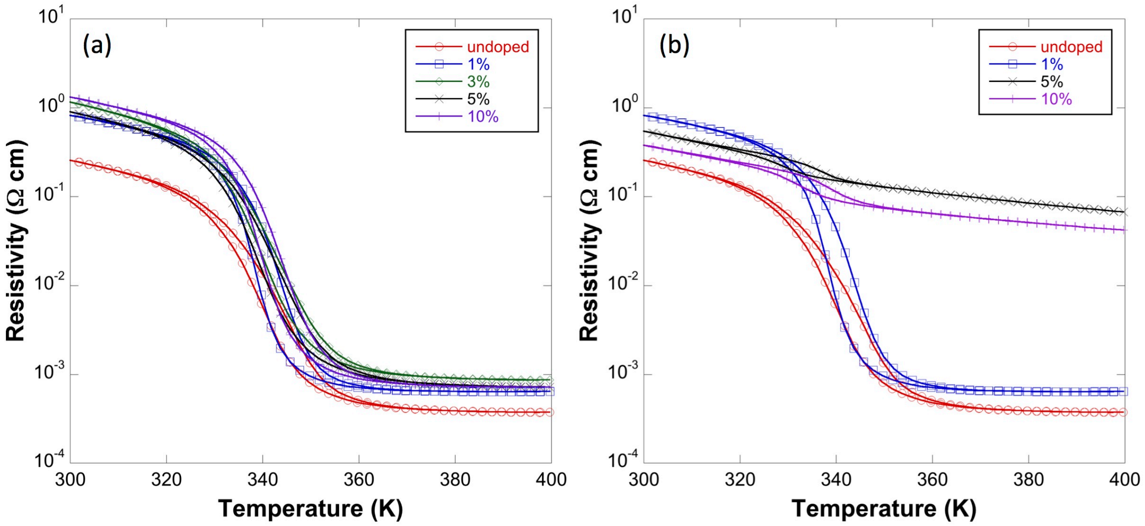

Figure 6.4 Resistivity as a function of temperature of (a) sample set A: fixed frequency mode and (b) sample set B: variable frequency mode. The low fixed frequency doped Mn^{4+} results in resistance ratio enhancement up to 3 folds, while for the variable frequency set, the increasing in bias frequency results in a suppressed MST.

The resistivities as a function of temperature for all of the samples in set A and B, including the reference undoped VO_2, are shown in figure 6.4. The Mn^{4+} doping at low fixed frequency improved the MST, enhancing the resistance ratio between the semiconducting phase and the metallic phase up to 3 times as compared to the undoped film. Figure 6.4(a), for sample set A, unveils the increase of resistivity in both semiconducting and metallic states, with a larger increase in the semiconducting state resulting in the enhanced MST. The point defects, i.e. inhomogeneous out-of-plane lattice and random in-plane distortions of V-V from substitution of Mn^{4+}, will increase the resistivity in both phases (below and above T_{MST}). However, as the samples are heated up, the crystal will be more ordered due to the removal of V-V distortion. As a result, the effect of the defects in the resistivity is reduced, resulting in the enhance MST.

On the contrary, for the variable frequency set as shown in figure 6.4(b), the MST gets highly suppressed as the doping frequency increases (% Mn increases), with a drastic increase in the resistivity of the metallic state. This is likely due to the surface scattering from larger grain boundaries and rougher film surface as shown in AFM images (figure 6.3). The multiple orientations of crystal grown (mosaicity) also play a role in the metallic phase since the resulting in-plane lattice is still more disordered compared to those of the single out-of-plane crystal orientation even after the sample is heated up. The resulting MST of sample set B is similar to the optical properties of Mn doped VO_2 [95]. The 20% sample (doped at 41.67 kHz) was insulating and R vs T cannot be measured. This could be the result of a large amount of defects and the additional phases as detected in XRD.

The decreasing resistivity below T_{MST} in set B as the % Mn increases from 1-10% could be related to the extra electrons from the substitution of Mn^{4+}. These extra electrons increase the conductivity in both the metallic and semiconducting phases. However, the absence of reduction in resistivity of set A found in this experiment suggests that the defects dominated the effect of additional electrons; it is also possible that the defects introduced reduce the mobility of the carriers in the lattice. Since a decreasing resistivity was found in set B, with more point defects than set A, it suggests that the actual doping concentration of set B (at higher frequency) may be higher than the estimated.

The decrease in the resistivity was also reported on Mn-doped VO_2 thin films grown by magnetron sputtering. [95] The two films with lower doping concentration showed lower resistivity than the undoped film, however Liu et al. [95] observed a larger resistivity as the Mn concentration increased. This is most likely due to point defects and degraded crystallinity associated with the dopants.

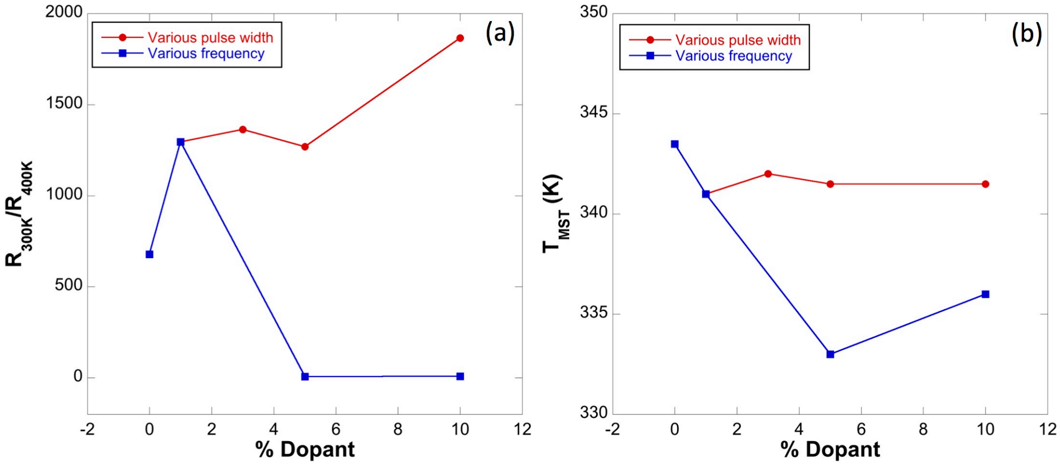

Figure 6.5 (a) Resistance ratio as a function of % Mn for the samples doped with different modes. The 10% doped with low fixed frequency mode gives the highest ratio, which is about 3 times larger than the undoped sample. (b) Transition temperature as a function of % Mn, comparing two modes.

Figure 6.5 summarizes the resistance ratio [R(300K)/R(400K)] and the T_{MST} as functions of Mn content for two different processes. The resistance ratio in figure 6.5(a) shows the increasing trend of the ratio as the Mn content increases for the variable pulse width (fixed frequency) mode, and the resistance ratio increases up to 3 times at the 10% Mn concentration. On the other hand, for the variable frequency mode, the ratio dramatically decreases as the Mn content increases from 1-10%, due to the defect related scattering of carriers as mentioned earlier. In both modes, the 1% sample doped at 1.56kHz already doubles the resistance ratio compared to the undoped film.

In contrast, T_{MST} appears to be relatively unchanged as seen in figure 6.5(b); while in the variable frequency set, T_{MST} appears to shift to lower temperatures as the doping bias frequency increases (higher % Mn). This change in the transport behaviors could relate to the change in lattice parameter *b* as evident in XRD spectra. As the film peak position shifts down (summarized in table 6.6), the c_r-axis (a_m) is likely to be compressed and that can result in the reduced T_{MST} which is in agreement with the aforementioned results in Chapter 5 and a previous report [40].

6.3.3 Doping at lower frequency 1.00 kHz

In this experiment, the transport properties of Mn-doped samples with a lower bias frequency of 1.00 kHz were studied to minimize the effect of defects introduced from higher frequency doping. The deposition conditions are listed in table 6.3 for sample set C, where the content of Mn^{4+} explored is in a wider range than that of set A. The estimated % dopants are 5, 10, 15, 20, and 25%. Samples in the set were also used as references for the Al-doped samples in section 6.4, and also to study the frequency dependence of the same Mn content samples in section 6.3.4.

The AFM images over 1×1 μm^2 area of the samples reveal similar grain size ~ 100 nm for all samples (similar to those of set A as shown in figure 6.2). The rms roughness of the samples is in the range of 1.6-2.8 nm; the rms roughness does not depend on the % doping – it does not monotonically increase but rather fluctuates . XRD scans of all samples are shown in figure 6.6(a). The peaks shown were the only peaks detected in long range XRD scans from 20 to 80 degrees, indicating single phase VO_2. The (020) peak of *M*-VO_2 first shifts down (increasing lattice parameter *b*) as the % Mn increases from 5 to 10%. Then, it shifts up and stays rather constant at 15-25% Mn with no obvious change in the peak height.

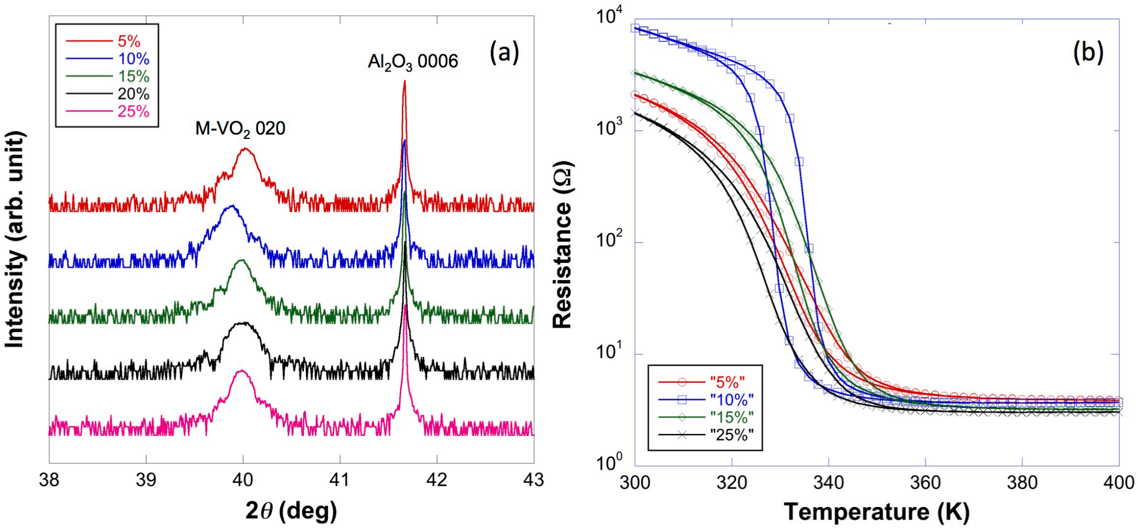

Figure 6.6 (a) XRD of sample set C showing (020) *M*-VO_2 peak coupling to the substrate peak. (b) Resistance as a function of temperature for the samples doped at 1.00 kHz.

The temperature dependent resistance measurements are shown in Figure 6.6(b), while the data from the 20% Mn-doped sample is not included for better clarity. The 20% sample result lies in between the 15% and 25% Mn-doped results for both T_{MST} and resistance ratio (R_{300K}/R_{400K}). Since the thicknesses of the films were roughly the same at about 50 nm, the resistance measured on devices of the same size can be compared without converting to resistivity.

The MST results reveal that doping at 1.00 kHz introduced point defects slowly enough to see the evolution of these defects as the % dopant increased from 5 to 10%. There is a huge enhancement of the MST in the 10% Mn-doped sample (compare to the 5%): the transition gets sharper with larger resistance ratio. Then the MST starts to get suppressed as the % Mn increases further. The resistance (resistivity) in the semiconducting phase starts to decrease as the Mn content increases from 10-25%. This effect could be from the electrons which are introduced from the substitution of Mn^{4+}

ions in the lattice. It could also be from the role of oxygen deficiency (interstitial defect), or from contributions of both electrons and oxygen defects, since the effect is similar to what have been observed in chapter 4 as the oxygen flow rate is reduced.

6.3.4 Bias pulse frequency effect on transport properties

In this part, to minimize the effect of additional Mn introduced, the transport properties of Mn-doped samples with the same nominal dopant concentration of 5% are compared. The samples are from set A, B, and C, grown with various doping frequencies of 1.00 (C1), 1.56 (A4), and 8.47 (B3) kHz respectively. The resistivity as a function of temperature was measured on a simple-current device, while the Hall effect measurements were conducted on a Hall bar device fabricated on each sample.

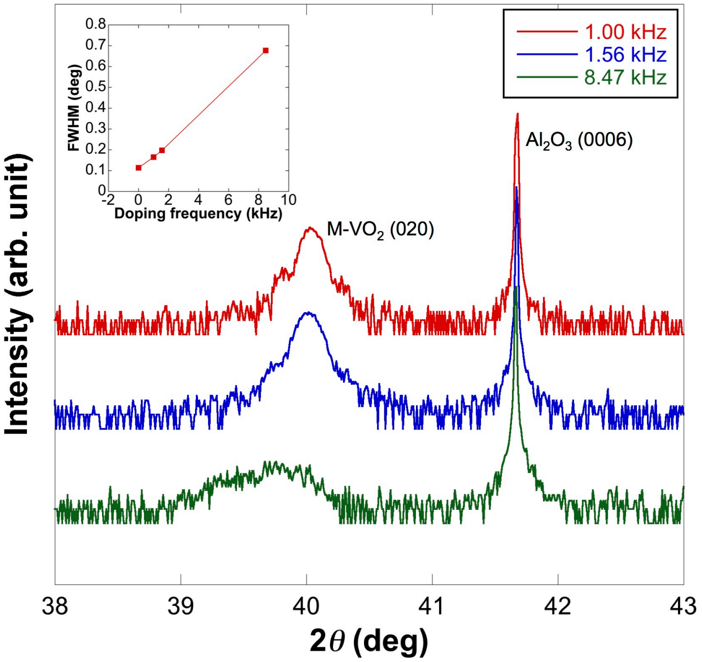

Figure 6.7 XRD of the 5% Mn-doped samples, doped at different frequencies, showing (020) M-VO_2 coupling to the Al_2O_3 substrate peak. The inset shows FWHM of the (020) M-VO_2 peak as a function of doping frequency (*0% from undoped sample).

XRD scans show the broadening of the (020) *M*-VO_2 peak as the doping frequency increases (figure 6.7), indicating a degraded crytallinity as a result of high frequency target biasing. The inset shows the FWHM of the (020) *M*-VO_2 peak as a function of doping frequency. The FWHM of the undoped film (A1) is also included for reference. The FWHM increases as the doping frequency increases. At the highest frequency (8.47 kHz), the film peak also starts to split, indicating either the introduction of a secondary phase or the multiple crystal orientations.

The resistivity as a function of temperature, shown in figure 6.8(a), shows a significant suppression of the MST in the highest doping frequency sample. As the doping frequency increases from 1.56 to 8.47 kHz, the resistivity in the metallic state also increases significantly as a result of scattering carriers in the multiple crystal orientations as found in XRD. As the doping frequency changes from 1.00 kHz to 1.56 kHz, there was no sign of multiple crystal orientation or secondary phase growth, hence a slight increase in the introduced point defects enhanced the MST.

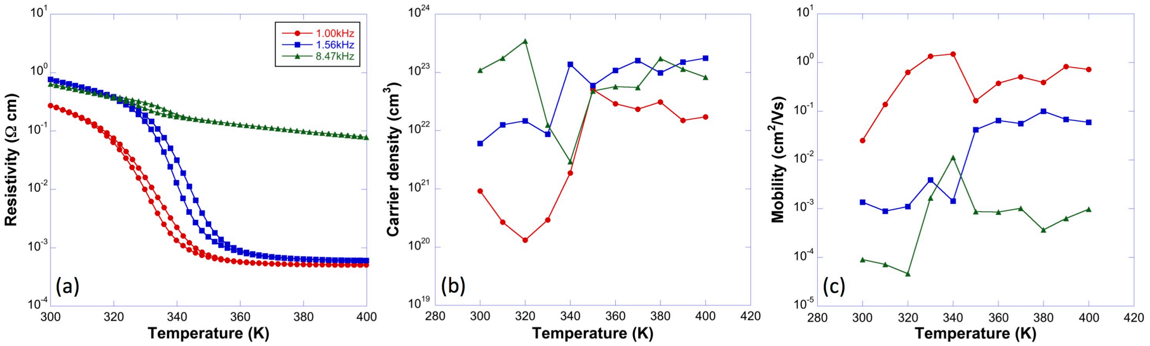

Figure 6.8 (a) Resistivity as a function of temperature of 5% Mn-doped samples, with various doping frequencies. (b) Carrier density and (c) Hall mobility as a function of temperature extracted from Hall effect measurements.

Hall effect measurements provide information on the majority carrier density and Hall mobility of these films as a function of temperature as shown in figure 6.8 (b) and (c). The carrier densities of all samples were found to be higher than that of the typical undoped VO_2, especially in the semiconducting phase. The carrier density is about 1-4 orders larger (~10^{19} cm^{-3} for undoped thin films) [28,44]. The carrier density in the semiconducting phase increases as the doping frequency increases. In the metallic phase, the carrier density is about the same or slightly smaller than that of the typical undoped films (~10^{23} cm^{-3}) [28,44]. The 1.00 kHz doped sample showed a 2-3 order change in the carrier density around the transition, similar to what has been observed in undoped films [44] but with slightly smaller change, where the size of the change in the carrier density is decreasing as the doping frequency increases.

For the sample doped with 1.00 kHz, the majority carriers were electrons in the semiconducting phase and switched to holes in the metallic phase (350 - 400 K). For the 1.56 kHz sample, the majority carriers were electrons in both phases. For the 8.47 kHz sample, the majority carrier type randomly switched throughout the measured temperature range (300 - 400 K). The evidence of changing the majority carrier type was found in previous reports [24,44], however the origin of the behavior has not been fully understood. The sample with the lowest doping frequency of 1.00 kHz has the highest Hall mobility, which is similar to the values found in undoped VO_2 films [28,44]; the mobility decreases as the doping frequency increases. The reduced Hall mobility is likely due to the defect-related scattering of free carriers that occurs in both semiconducting and metallic states of doped VO_2.

There was also a sign of an abrupt change, a jump or drop, of the mobility around the T_{MST} similar to previous reports on undoped VO_2 films [28,44], which is likely from the change in majority carrier type from electron to hole (for the abrubt drop). The difference of these doped films compared to the undoped films was that after the MST, the mobility seems to be 1-2 orders of magnitude higher than before the MST. This explains the role of defects, since the crystal became more ordered as it was heated up and the effect of defects was reduced, resulting higher mobility above T_{MST}.

6.4. Doping with aluminum

In this experiment, the microstructures and transport properties of Al-doped samples (set D) are compared to those of Mn-doped samples (set C), where all the samples were doped at 1.00 kHz to minimize the effect of defects arising from high frequency doping. The deposition conditions are listed in table 6.4 for sample set D. The estimated % doping are 5,10,15, and 20% Al.

6.4.1 Crystal structure and surface morphology of Al-doped VO_2

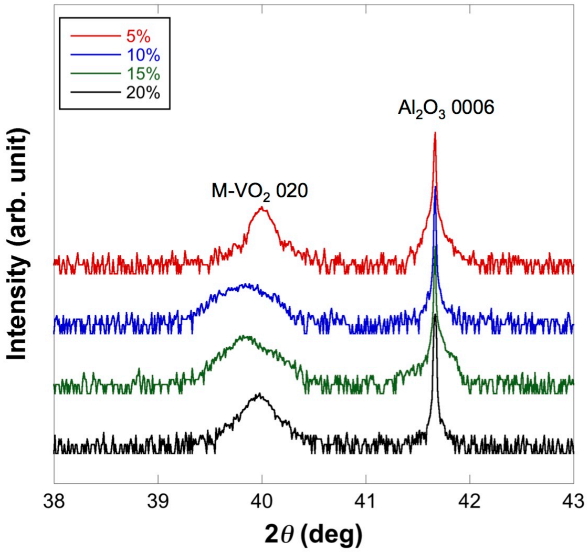

Figure 6.9 XRD of sample set D: Al-doped at 1.00 kHz showing (020) *M*-VO_2 peak coupling to the substrate peak.

XRD scans of all samples are shown in figure 6.9. The peaks shown are the only peaks detected in long range XRD scans (20-80 deg), indicating single phase VO_2. The film peak of Al-doped samples first shifts down as the % Al changes from 5 to 10%, and monotonically shifts up, due to a decrease in the lattice parameter *b*, from 10-20 % Al. The peak height seems to decrease as the peak shifts down between 5-10% doping, indicating worse crystallinity in the out-of-plane direction. The peak is also broadened. Above 10% doping, the peak height increases as the peak shifts back up and as the % Al increases, the peak is also narrower. As dopant content increases, the Al-doped samples experienced more crystallinity degradation than the Mn-doped samples, which may relate to the distortion toward triclinic (*T*) and *M2* phases of VO_2. However to confirm the *M2* phase in these samples, Raman spectroscopy is needed, since the XRD alone is not enough to reveal the phase [98].

When an Al^{3+} ion substitutes for a V^{4+} ion in the V-V pair, the single *d*-electron in the unpaired V^{4+} ion (effective ionic radius = 58 pm [97]) could be trapped by a hole in a 2p orbital of oxygen surrounding the Al^{3+} ion, resulting in the appearance of a V^{5+} ion (effective ionic radius = 54 pm [97]). The resulting smaller ionic radius of V^{5+} makes the *M1* structure of the VO_2 lattice becomes less distorted, approaching the triclinic (*T*) and *M2* phase and resulting in a higher T_{MST}. The unpaired V^{4+} donors are compensated by the trivalent acceptors, resulting in the unchanged resistivity in the semiconducting phase. With the increasing amount of Al^{3+} introduced, the contribution of holes in the transport properties would also increase. Moreover the Al^{3+} and V^{5+} will likely to create point defects in the out-of-plane direction, i.e. mosaicity (more than the effect of Mn^{4+}), due to smaller ionic radii.

It has been found that acceptor-like doping with metals such as Cr^{3+} and Al^{3+} can stabilize the *M2* and *T* phases of VO_2 at room temperature [7,39,99]. A phase diagram for free-standing Al-doped VO_2 nanostructures based on experimental results by Strelcov et al. [39] is shown in figure 6.10. According to the phase diagram, all of the samples presented in this section should have an *M2* structure at room temperature. However, the strained films may have a different phase diagram than that of the free-standing nanostructures due to substrate clamping.

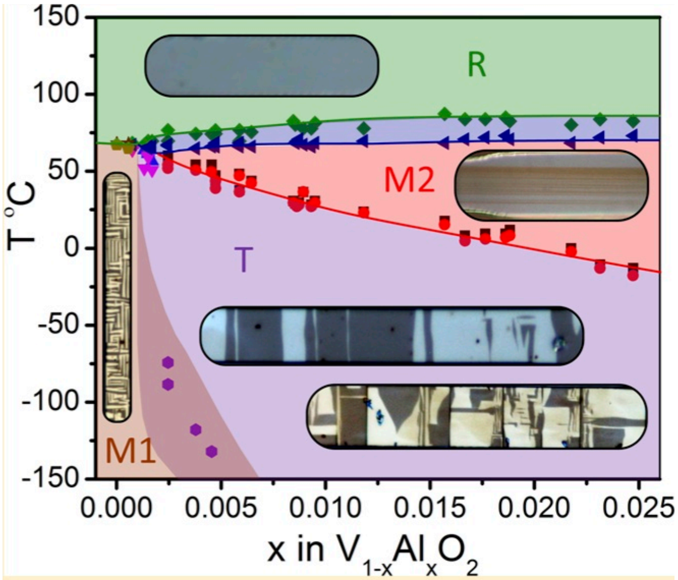

Figure 6.10 Temperature-composition phase diagram for free-standing nanostructures, with polarized optical images of each phase. [39]

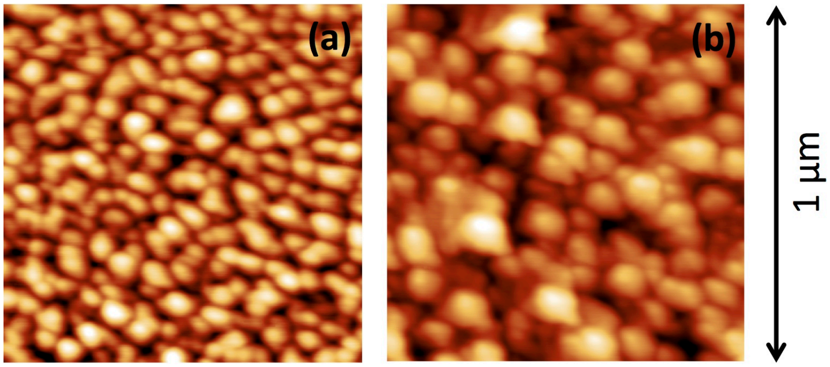

Figure 6.11 AFM images of (a) 20% Al and (b) 20% Mn samples respectively.

The AFM images over 1×1 μm^2 area of 20% Al-doped (1.1 nm rms roughness) and 20% Mn-doped (2.1 nm rms roughness) are shown in figure 6.10 (a) and (b) respectively. The grain sizes of all Al-doped samples were smaller than those of Mn-doped samples (~100 nm). The grain sizes of Al-doped samples (~50-70 nm) were also smaller than the average grain size of typical undoped VO_2 films deposited at the same conditions (~100-150 nm). The rms roughness of the Mn-doped samples was in the range of 1.6-2.8 nm, while the Al-doped samples were smoother with rms roughness of 0.5-1.1 nm which can be explained by the smaller grain sizes. The rms roughness and average grain size of Al-doped samples are summarized in table 6.7.

Table 6.7 Summary of rms roughness and average grain size for set D

% Al	RMS (nm)	Grain size (nm)
5	1.1	60
10	0.5	50
15	0.6	60
20	1.1	70

The rms roughness for both types of dopants does not depend on the % dopant as the grain size of Mn-doped films was roughly the same throughout the range of % Mn. However, as the %Al increases from 5 to 10%, the grains get smaller, and as the Al concentration increases from 10 to 20%, the grain size is monotonically increased. The trend of the grain size is similar to the trend of inhomogeneity detected in XRD. The smaller grains indicate less dislocations in the plane parallel to the substrate surface. The dislocation and point defects, arising from higher amounts of dopants, are more likely introduced in the plane perpendicular to the substrate surface, creating the inhomogeneity in the out-of-plane lattice and resulting in a degraded film peak.

6.4.2 Transport properties

(a) Metal-semiconductor transition

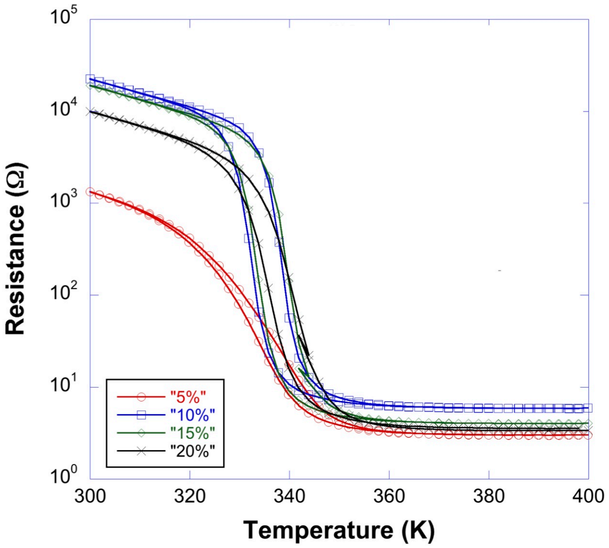

Figure 6.12 Resistance as a function of temperature for Al-doped VO_2, showing the largest improvement of MST reported in this chapter.

The temperature dependent resistance measurements are shown in Figure 6.12. Since the thicknesses of the films were roughly the same around 50 nm, the resistance measured on the same size devices can be compared without converting to resistivity. The resistance ratio (R_{300K}/R_{400K}) and T_{MST} of both Al-doped and Mn-doped samples were extracted from the R vs. T curves and plotted as a function of % dopant, as shown in figure 6.13.

Figure 6.12 shows that the resistivity in the semiconducting state first increases dramatically as the Al content increases from 5 to 10%. This is likely from a combination of the introduced point defects as Al^{3+} substitutes V^{4+}, and the hole injection from the acceptor-like doping (from interstitial Al^{3+}). Because holes have much lower mobility compared to electrons, the resistivity increases. As the Al concentration increases from 10 to 20%, the resistivity in the semiconducting state decreases monotonically, which may be from the oxygen deficiency effect. The metallic state resistivity of all samples is about the same except the 10% sample that has a higher resistivity. This sample had the smallest grains and the smoothest surface in the set, hence the higher resistivity in the metallic state is likely due to the larger amount of defects introduced in the out-of-plane direction, as seen in the XRD.

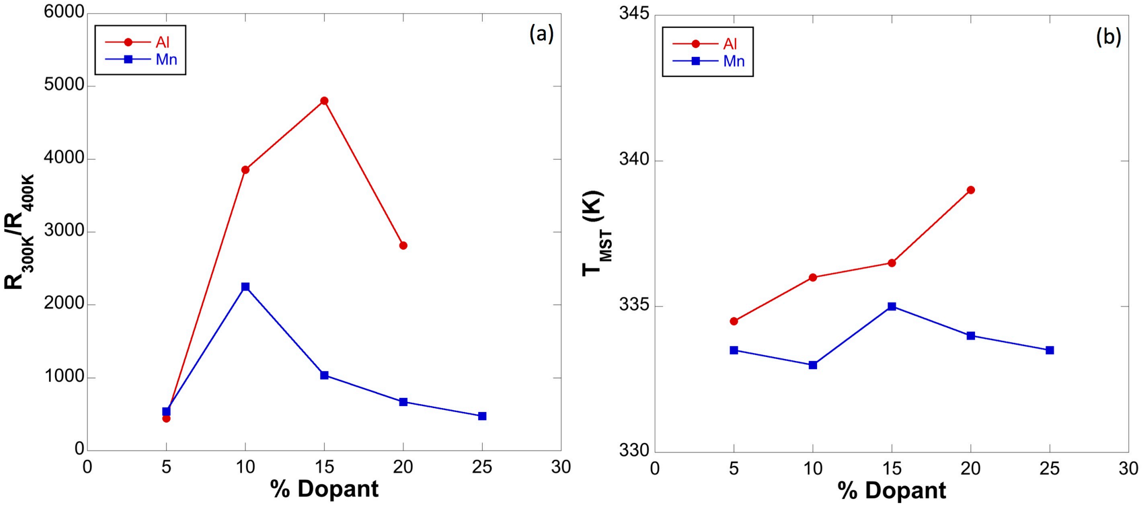

Figure 6.13 (a) Resistance ratio as a function of % dopant. The Al-doped increases the ratio by 11 times, while the Mn-doped increases the ratio by 4 times. (b) Transition temperature as a function of % dopant. The Al-doped slightly increase T_{MST}, while the T_{MST} of Mn-doped samples are fairly constant.

The resistance ratio shown in figure 6.13(a) first increases and then decreases when the % Mn > 10%. The ratio was increased up to 4 times, comparing the maximum at 10% Mn to the lowest doped 5% Mn. For Al-doped samples, the resistance ratio was increased up to 11 times, comparing the maximum at 15% Al to the 5% Al, which is much higher than the Mn-doped samples. The 5% doped Mn and 5% doped Al samples have very similar R vs T, which can be used as references. Figure 6.13(b) shows the T_{MST} for both Mn-doped and Al-doped samples. The T_{MST} of Mn-doped samples are roughly constant, fluctuating around 334 K. However, it seems like the T_{MST} slowly drops as the %Mn increases from 15-25%, which is again similar to the effect of a reduced oxygen environment. [75,100] The results of Al-doping show not only the enhanced MST but also show that the T_{MST} is monotonically shifted to higher temperatures as the % Al increases. The change of T_{MST} contradicts the oxygen-deficiency defects, but can be explained by the effects of the acceptor-like doping (equivalent to oxidization of V^{4+}) [35,36,95,101]. The increase of T_{MST} for the 10-20% doped samples may also relate to the decrease in the lattice parameter *b* (detected in the upshift of the (020) peak in XRD); as *b* decreases, c_r (a_m) may also increase, enhancing the effect of correlations for the Mott transition. [41]

The improvement of the MST in Al-doped films is due to a combination of point defects introduced by slow incorporation of dopants and hole injection from acceptor-like doping, while the enhancement of the MST in Mn-doped films is purely from the point defects. In addition XRD results show that Al-doped samples are likely to get more inhomogeneity in the out-of-plane direction than the Mn-doped samples. Hence the MST of films doped with Al^{3+} is more enhanced than those doped with Mn^{4+}.

There is always oxygen deficiency introduced from the RBTIBD technique used in this chapter for both types of dopants. The oxygen-deficiency defects suppress the transition, reducing the resistivity in the semiconducting phase as well as the $T_{MST.}$ Since an acceptor-like doping with trivalent metals (Al^{3+}) introduces holes and can compensate for oxygen deficiency, the resulting T_{MST} of Al-doped samples is higher than those of

Mn-doped samples. Moreover, it is possible that these Al-doped samples have a *M2* phase, which is a true Mott insulator. This may also explain the shift in T_{MST}.

(b) Carrier type and mobility

Hall effect measurements were conducted on a Hall bar device fabricated on the 5% Mn and the 5% Al doped samples. Using a single band model, the carrier density and Hall mobility were calculated and plotted as a function of temperature as shown in figure 6.14 (b) and (c), respectively. The MST of these two samples are similar, shown in figure 6.14 (a), however the mobility and carrier density yield different results.

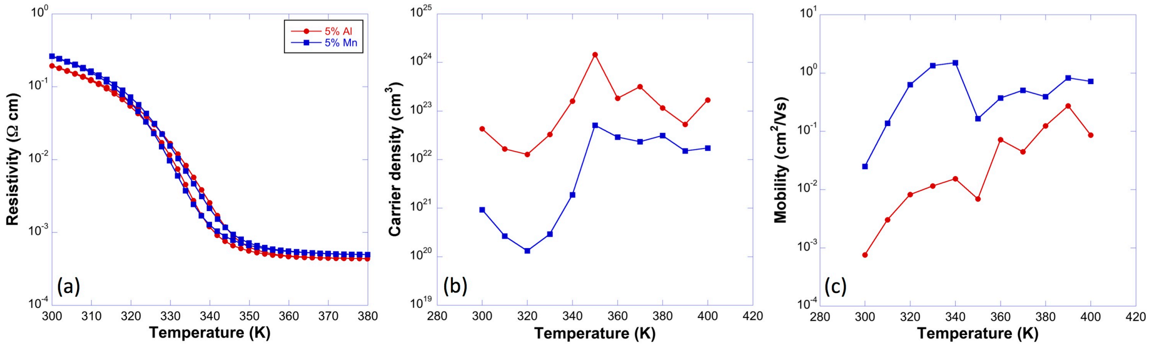

Figure 6.14 (a) Resistivity as a function of temperature of 5% Mn-doped and Al-doped samples. (b) Carrier density and (c) Hall mobility as a function of temperature extracted from Hall effect measurements.

The carrier density of these doped sample is higher than that of the typical undoped films, which is around 10^{19} cm^{-3} before the MST and about 10^{23} cm^{-3} after the MST, where the majority carriers are mostly electrons both before and after the MST. The mobility of both is lower than that of the undoped films, that is around 0.1-5 cm^{2}/Vs at room temperature, as seen in chapter 4-5 and in previous reports. [28,44]. Surprisingly for both samples, the majority carrier type was found to be electrons before the MST, and it switched to holes after the MST (350 - 400 K).

The results of Mn-doped samples agree with the fact that the doping with Mn^{4+} introduces electrons resulting in the increased electron density in the Hall effect, and that the defect related scattering of free carriers reduces the Hall mobility. Figure 6.14(c) shows that the Hall mobility of the Al-doped sample was roughly 2 orders of magnitude smaller than that of the Mn-doped sample in the semiconducting state, and about 1 order lower in the metallic state. This confirms the hypothesis of introduced holes in the lattice, due to the large difference of electron and hole mobilities, with electron mobility being almost 4 orders of magnitude larger. [102]

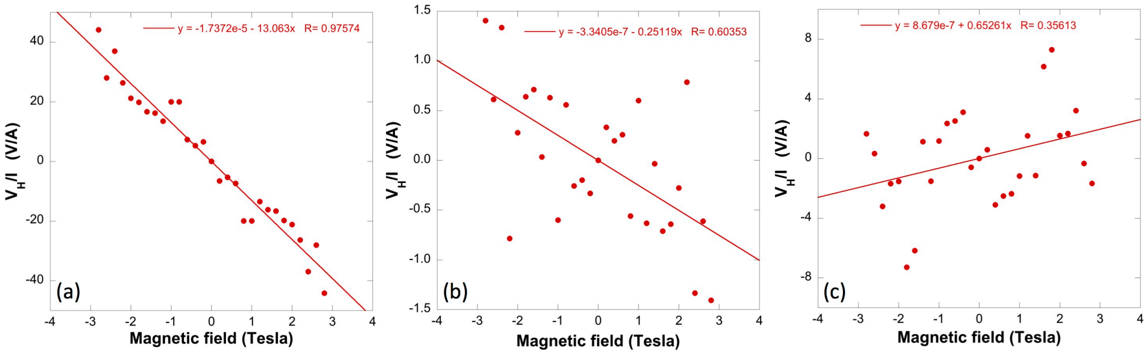

Figure 6.15 Hall resistance as a function of magnetic field at 300 K for (a) 5% Mn-doped, (b) 5% Al-doped, and (c) 10% Al-doped samples.

Figure 6.14(b) shows that the carrier density of the Al-doped sample was roughly 2 orders of magnitude higher than that of the Mn-doped sample in the semiconducting state, and about 1 order higher in the metallic state. There appears to be an abrupt jump in the carrier density around the transition for both samples. However, the resulting carrier density in the semiconducting phase of the Al-doped sample contradicts the hypothesis that the trivalent doping (acceptor-like) will introduce holes. The contradiction can be explained in the followings. Figure 6.15 shows raw data of Hall measurements of Mn-doped and Al-doped samples near room temperature, with a linear fit using the single band model. The fit for both Mn-doped and Al-doped at 5%, shown in figure 6.15 (a) and (b) respectively, has a negative slope, indicating electrons as majority carriers. However, the fit for the Al-doped sample is much worse than the Mn-doped sample; the Hall voltage largely scatters across 0V as the magnetic field increases in one direction. This phenomenon can be explained in the following discussion:

The single band model is only true when one type of carrier largely dominates the other and the other is negligible. In fact, the Hall coefficient for a semiconductor [103] can be represented by:

$$R_H = \frac{V_H d}{IB} = \frac{p\mu_h^2 - n\mu_e^2}{e(p\mu_h + n\mu_e)^2} \tag{6.2}$$

, where *I* is the excitation current, *B* – magnetic flux density directed perpendicular to the sample plane, V_H – Hall voltage (after the magneto-resistance removed), $e = 1.6 \times 10^{-19}$ coulomb, d = film thickness. If the electron is truly dominant ($n\mu_e^2 \gg p\mu_h^2$) then $R_H = -\frac{1}{ne}$; if holes are dominant ($p\mu_h^2 \gg n\mu_e^2$) then $R_H = \frac{1}{pe}$. Hence when plotting $\frac{V_H}{I}$ vs. *B*, the linear relationship is expected with the slope being inversely proportional to carrier density, where a negative slope indicates electrons are dominant and a positive slope indicates hole are dominant.

Considering a mixed carrier system, as one type is about to dominate the other, the slope will become smaller approaching zero. The linear fit will no longer hold, as both carrier types interact with magnetic field in the opposite way, the resulting Hall voltage will be more scattered. Therefore, the high carrier density extracted from a single band model needs to be interpreted in two distinct ways:

1. It is a true representation of majority carrier density, if the linear fit of Hall resistance or Hall voltage as a function of magnetic field is good;
2. It indicates mixed carrier types of holes and electrons, if the linear fit is bad (especially when the Hall voltage fluctuates across 0V as the magnetic field is applied in one direction).

Using this analogy, figure 6.15(b) shows the sign of hole doping in 5% Al-doped at room temperature compared to 5% Mn-doped [figure 6.15(a)] where the result is better fit using a single band model. The confirmation of hole doping is also shown in figure 6.15(c), where the majority type already changed to hole as the % Al increased to 10%.

6.5 Effect of dopants on the electronic band structure

As Mn^{4+} substitutes V^{4+}, the lattice parameter *b* seems to be constant. However, the electrons doping from Mn^{4+}, which do not contribute to the electronic structure, also tend to lower the d_π level [18], closing the band gap. The results for the lowest doping bias frequency agree with this picture, however as the defects are introduced from higher frequency doping, the additional electrons are trapped in the defects (reduced mobility). At higher doping frequency, there is likely to be more distortion in the out-of-plane, hence more distorted octahedral oxygen destabilize and shift up the d_π band, compensating the extra electrons.

On the other hand, the hole introduced from Al^{3+} will be localized resulting in V^{5+}. The shorter V-O bonds from the V^{5+} will narrow the d_π and tend to lift the band up

[18]. The energy increase of the d_π electrons reduces the screening of electrons in the $d_{||}$ band, thus enhancing the effect of correlations [14], opening the insulating gap, and increasing T_{MST}.

6.6 Summary

Reactive Bias Target Ion Beam deposition was used to explore the chemical doping (Al^{3+} and Mn^{4+}) of VO_2 thin films. The doping content can be tuned by the bias pulse width and frequency. The lower frequency of bias pulse resulted in better crystallinity, likely due to the slow incorporation of dopants in the monoclinic lattice of VO_2, enhancing the MST. In contrast, the high frequency doping degraded film microstructures and highly suppressed the MST.

Both type of dopants were found to enhance the MST especially when doped at low bias frequency. The MST of films doped with Al^{3+} was more enhanced than those doped with Mn^{4+} due to different valence states. Doping with Mn^{4+} did not raise the T_{MST} while doping with Al^{3+} slightly increased the T_{MST} as the Al concentration increased. Evidence of hole doping from Al^{3+} was also found in Hall effect for the first time. The increase in the resistance ratio found in this study will benefit in many applications such as switching devices, optical shutters, etc. However further study of microstructure of these doped films using Raman spectroscopy and study of valence states of these ions (V, Mn, and Al) using soft x-ray spectroscopy are needed.

CHAPTER 7. Concluding remarks

7.1 Summary of scientific observations

In summary, this thesis investigated the micro-strain, macro-strain, and doping effect on the MST of VO_2 thin films deposited by the RBTIBD technique. The effect of growth conditions (substrate temperature and O_2 flow rate) for VO_2 thin films grown on *c*-plane sapphire substrates was explored. The higher substrate temperature resulted in higher T_{MST}, with narrower hysteresis, sharper transition, and improvement of MST with a more conductive metallic state due to the improvement of crystallinity. The influence of O_2 flow rate on the microstructure, electronic structure, and transport was investigated. A small change of O_2 flow rate dramatically affected the transport behavior of VO_2 thin films, even though the valence state of V^{4+} ion was found unchanged. Thin films deposited in a reduced O_2 environment revealed the following: increased carrier density, more conductive insulating phase, and lower T_{MST} due to the micro-strain caused by defects formed in the oxygen growth environment.

The effect of macro-strain from bi-axial substrate clamping was investigated on VO_2 thin films deposited on TiO_2 (100), (001), and (011) substrates. The T_{MST} was modified in a wide range (300-430 K), using bi-axial strain variation by thickness control. The high resistance ratio between semiconducting and metallic states was found preserved as the T_{MST} shifted. Both semiconducting and metallic phases were shown to have rutile structure using Raman spectroscopy. The strained VO_2 underwent an electronic phase transition without the Peierls transition. A new phase diagram of bi-axially strained VO_2 was proposed based on experimental data collected from current and previous studies.

A very large conductivity anisotropy was discovered in the VO_2/ TiO_2 (100) films. Conductivity mappings using nanoscale infrared spectroscopy and conductive AFM of VO_2 thin films revealed the co-existence stripe states that lead to anisotropy for both optical and transport properties. The anisotropy was observed below and above the MST. It was found that the conductivity anisotropy ratio $\sigma_{[001]}/\sigma_{[010]}$ was 41.5 at 300 K, a value much larger than that of single-crystal VO_2. The conductivity along [001] in the metallic phase was unusually high $\sim 2.4\times10^5$ S/cm, and is comparable to a very good conductor.

RBTIBD was used to explore the chemical doping (Al^{3+} and Mn^{4+}) of VO_2 thin films deposited on *c*-plane sapphire. The doping content can be tuned by the bias pulse width and frequency. The lower bias pulse frequency resulted in better crystallinity, due to the slower incorporation of dopants in the monoclinic lattice of VO_2, and enhanced the MST (higher resistance ratio and sharper transition). The high frequency doping degraded film microstructures and highly suppressed the MST. Hall effect measurements also revealed that higher frequency doping reduces the carrier mobility in both semiconducting and metallic states due to the defect-related scattering of free carriers. The doping technique developed here resulted in a better crystallinity of the doped films compared to other doping methods explored.

Both type of dopants were found to enhance the MST especially when doped at low bias frequency. The MST of films doped with Al^{3+} was more enhanced than those doped with Mn^{4+} due to different valence states. Doping with Mn^{4+} did not raise the

T_{MST}, while doping with Al^{3+} slightly increased the T_{MST} as the Al concentration increased. Evidence of hole doping from Al^{3+} was also found in Hall effect for the first time. A signature of oxygen deficiency was also found in transport measurements of samples with higher dopant concentration for both types. The increase in resistance ratio found in this study will benefit in many applications such as switching devices, shutters, etc.

7.2 Suggested future work

The development of reproducible high quality VO_2 thin films for the study of correlation among film strain, defects, and transport behavior was the objective of this work. Discussed below are my recommendations and suggestions of further explorations:

Development of VO_2 thin films on other substrates

To fully utilize the benefit of VO_2 thin films, the growth on other substrates, such as silicon, quartz, etc., need to be optimized. Silicon wafers are widely used both commercially and in research due to cost efficiency and the ability to fabricate integrated circuits for microelectronic devices. While an IR transparent substrate is needed for optics application. Different kinds of substrates introduce dissimilar strain due to lattice mismatch, so a buffer layer may need to be added to stabilize and improve the growth of a crystalline film. A detailed characterization of microstructure and MST of thin films as a function of growth parameters, buffer type and thickness must be done.

Multilayer interface study

Theoretical study of quantum confinement in a 5/3 TiO_2/VO_2 super lattice predicted that it is half metallic and can be potentially used in spintronics. RBTIBD has the ability to precisely control the sputtered metal amount, however the study of interfaces between two layers is needed. Improving the interface can be achieved by the exploration of growth parameters. Additional tools such as TEM are required to explore the interface. A detailed characterization of MST as a function of VO_2 interface must be done. Other multilayer applications, such as an electrically controlled IR shutter, also require multilayer structure. Hence the study of interfaces is very important for improving VO_2 film quality and interface quality for those applications.

Exploration of other dopants

The MST varies as the dopants change. It is not only the valence state, but also the effective ionic radius of dopants that contributes in the complicated mechanism of tailoring crystal structure and the transition of the VO_2 thin film. Hence more dopants need to be explored. Nb is one of suitable candidates; it has oxidation state of +3 to +5, with various ionic radii that is larger than those of V^{4+}. Moreover NbO_2 also has the phase transition that occurs at much higher temperature (1080 K), which makes it more interesting. It is also much heavier than V, making it easier to detect the doping concentration using energy dispersive x-ray spectrometry (EDS). The valence state of V and Nb should be studied via x-ray absorption and photoemission spectroscopy. A detailed characterization of MST and microstructure of the doped film as a function of at. % Nb (with small increment in a wide range) must be done.

BIBLIOGRAPHY

[1] F. Gervais and W. Kress, Phys. Rev. B **31**, 4809 (1985).

[2] F. J. Morin, Phys. Rev. Lett. **3**, 34 (1959).

[3] S. Lysenko, V. Vikhnin, F. Fernandez, A. Rua, and H. Liu, Phys. Rev. B **75**, 075109 (2007).

[4] J. B. Goodenough and H. Y.-P. Hong, Phys. Rev. B **8**, 1323 (1973).

[5] E. Caruthers and L. Kleinman, Phys. Rev. B **7**, 3760 (1973).

[6] P. Lederer, H. Launois, J. P. Pouget, and A. Casalot, J. Phys. Chem. Solids **33**, 1969 (1972).

[7] J. P. Pouget, H. Launois, T. M. Rice, P. Dernier, and A. Gossard, Phys. Rev. B **10**, 1801 (1974).

[8] C. Chen, R. Wang, L. Shang, and C. Guo, Appl. Phys. Lett. **93**, 171101 (2008).

[9] Y. Zhou and S. Ramanathan, J. Appl. Phys. **111**, 084508 (2012).

[10] D. Ruzmetov, G. Gopalakrishnan, C. Ko, V. Narayanamurti, and S. Ramanathan, J. Appl. Phys. **107**, 114516 (2010).

[11] *Emerging Research Devices* (ITRS report, 2011), pp. 1–80.

[12] C. Berglund and A. Jayaraman, Phys. Rev. **185**, 1034 (1969).

[13] M. E. A. Warwick and R. Binions, J. Mater. Chem. A **2**, 3275 (2014).

[14] A. Zylbersztejn, Phys. Rev. B **11**, 4383 (1975).

[15] A. Cavalleri, T. Dekorsy, H. H. Chong, J.-C. Kieffer, and R. W. Schoenlein, Phys. Rev. B **70**, 161102(R) (2004).

[16] S. Shin, S. Suga, M. Taniguchi, M. Fujisawa, and H. Kanzaki, Phys. Rev. B **41**, 4993 (1990).

[17] G. A. Sawatzky and D. Post, Phys. Rev. B **20**, 1546 (1979).

[18] J. B. Goodenough, J. Solid State Chem. **3**, 490 (1971).

[19] R. M. Wentzcovitch, W. W. Schulz, and P. B. Allen, Phys. Rev. Lett. **72**, 3389 (1994).

[20] R. E. Peierls, *More Surprises in Theoretical Physics* (1991).

[21] M. Fowler, *Electrons in One Dimension- the Peierls Transition* (2007).

[22] N. F. Mott, *Metal-Insulator Transitions* (Taylor & Francis Ltd, 1974).

[23] M. Imada, A. Fujimori, and Y. Tokura, Rev. Mod. Phys. **70**, 1039 (1998).

[24] H.-T. Kim, B.-G. Chae, D.-H. Youn, S.-L. Maeng, G. Kim, K.-Y. Kang, and Y.-S. Lim, New J. Phys. **6**, 52 (2004).

[25] H.-T. Kim, Y.-W. Lee, B.-J. Kim, B.-G. Chae, S. J. Yun, K.-Y. Kang, K.-J. Han, K.-J. Yee, and Y.-S. Lim, Phys. Rev. Lett. **97**, 266401 (2006).

[26] B.-J. Kim, Y.-W. Lee, S. Choi, J.-W. Lim, S. J. Yun, H.-T. Kim, T.-J. Shin, and H.-S. Yun, Phys. Rev. B **77**, 235401 (2008).

[27] K. G. West, J. Lu, J. Yu, D. Kirkwood, W. Chen, Y. Pei, J. Claassen, and S. A. Wolf, J. Vac. Sci. Technol. A **26**, 133 (2008).

[28] D. Ruzmetov, D. Heiman, B. Claflin, V. Narayanamurti, and S. Ramanathan, Phys. Rev. B **79**, 153107 (2009).

[29] M. M. Qazilbash, K. S. Burch, D. Whisler, D. Shrekenhamer, B. G. Chae, H. T. Kim, and D. N. Basov, Phys. Rev. B **74**, 205118 (2006).

[30] M. Soltani, M. Chaker, E. Haddad, R. Kruzelecky, and J. Margot, J. Vac. Sci. Technol. A **25**, 971 (2007).

[31] M. Dragoman, A. Cismaru, H. Hartnagel, and R. Plana, Appl. Phys. Lett. **88**,

073503 (2006).

[32] M. J. Lee, Y. Park, D. S. Suh, E. H. Lee, S. Seo, D. C. Kim, R. Jung, B. S. Kang, S. E. Ahn, C. B. Lee, D. H. Seo, Y. K. Cha, I. K. Yoo, J. S. Kim, and B. H. Park, Adv. Mater. **19**, 3919 (2007).

[33] M. Rini, Z. Hao, R. W. Schoenlein, C. Giannetti, F. Parmigiani, S. Fourmaux, J. C. Kieffer, A. Fujimori, M. Onoda, S. Wall, and A. Cavalleri, Appl. Phys. Lett. **92**, 181904 (2008).

[34] Y. Zhou, X. Chen, C. Ko, Z. Yang, C. Mouli, and S. Ramanathan, IEEE Electron Device Lett. **34**, 220 (2013).

[35] I. Kitahiro and A. Watanabe, Jpn. J. Appl. Phys. **6**, 1023 (1967).

[36] F. Béteille and J. Livage, J. Sol-Gel Sci. Technol. **13**, 915 (1998).

[37] J. H. Park, J. M. Coy, T. S. Kasirga, C. Huang, Z. Fei, S. Hunter, and D. H. Cobden, Nature **500**, 431 (2013).

[38] J. M. Atkin, S. Berweger, E. K. Chavez, M. B. Raschke, J. Cao, W. Fan, and J. Wu, Phys. Rev. B **85**, 020101(R) (2012).

[39] E. Strelcov, A. Tselev, I. Ivanov, J. D. Budai, J. Zhang, J. Z. Tischler, I. Kravchenko, S. V. Kalinin, and A. Kolmakov, Nano Lett. **12**, 6198 (2012).

[40] Y. Muraoka and Z. Hiroi, Appl. Phys. Lett. **80**, 583 (2002).

[41] B. Lazarovits, K. Kim, K. Haule, and G. Kotliar, Phys. Rev. B **81**, 115117 (2010).

[42] J. Laverock, A. R. H. Preston, D. Newby, K. E. Smith, S. Sallis, L. F. J. Piper, S. Kittiwatanakul, J. W. Lu, S. A. Wolf, M. Leandersson, and T. Balasubramanian, Phys. Rev. B **86**, 195124 (2012).

[43] E. Abreu, M. Liu, J. Lu, K. G. West, S. Kittiwatanakul, W. Yin, S. A. Wolf, and R. D. Averitt, New J. Phys. **14**, 083026 (2012).

[44] S. Kittiwatanakul, J. Lu, and S. A. Wolf, Appl. Phys. Expr. **4**, 091104 (2011).

[45] M. K. Liu, M. Wagner, E. Abreu, S. Kittiwatanakul, A. McLeod, Z. Fei, M. Goldflam, S. Dai, M. M. Fogler, J. Lu, S. A. Wolf, R. D. Averitt, and D. N. Basov, Phys. Rev. Lett. **111**, 096602 (2013).

[46] F. C. Case, J. Vac. Sci. Technol. A **7**, 1194 (1989).

[47] F. C. Case, J. Vac. Sci. Technol. A **2**, 1509 (1984).

[48] J. F. De Natale, P. J. Hood, and A. B. Harker, J. Appl. Phys. **66**, 5844 (1989).

[49] E. E. Chain, J. Vac. Sci. Technol. A **4**, 432 (1986).

[50] K. D. Rogers, J. A. Coath, and M. C. Lovell, J. Appl. Phys. **70**, 1412 (1991).

[51] E. Kusano, J. Vac. Sci. Technol. A **7**, 1314 (1989).

[52] H. Jerominek, Opt. Eng **32**, 2092 (1993).

[53] C. H. Griffiths, J. Appl. Phys. **45**, 2201 (1974).

[54] D. P. Partlow, S. R. Gurkovich, K. C. Radford, and L. J. Denes, J. Appl. Phys. **70**, 443 (1991).

[55] C. B. Greenberg, Thin Solid Films **110**, 73 (1983).

[56] G. Rampelberg, M. Schaekers, K. Martens, Q. Xie, D. Deduytsche, B. De Schutter, N. Blasco, J. Kittl, and C. Detavernier, Appl. Phys. Lett. **98**, 162902 (2011).

[57] M. Borek, F. Qian, V. Nagabushnam, and R. K. Singh, Appl. Phys. Lett. **63**, 3288 (1993).

[58] D. H. Kim and H. S. Kwok, Appl. Phys. Lett. **65**, 3188 (1994).

[59] U. Schwingenschlögl and V. Eyert, Ann. Phys. **13**, 475 (2004).

[60] S. Surnev, M. G. Ramsey, and F. P. Netzer, Prog. Surf. Sci. **73**, 117 (2003).

[61] S. M. Hu, J. Appl. Phys. **69**, 7901 (1991).

[62] J. W. Matthews and A. E. Blakeslee, J. Cryst. Growth **27**, 118 (1974).

[63] J. J. Quan, X. W. Zhou, L. He, R. Hull, and H. N. G. Wadley, J. Appl. Phys. **101**, 024318 (2007).

[64] H. Wadley, X. W. Zhou, J. J. Quan, T. Hylton, and D. Baldwin, 12 (2003).

[65] V. V. Zhurin, H. R. Kaufman, J. R. Kahn, and T. L. Hylton, J. Vac. Sci. Technol. A **18**, 37 (2000).

[66] H. R. Kaufman, J. Vac. Sci. Technol. A **5**, 2081 (1987).

[67] C. Hammond, *The Basics of Crystallography and Diffraction* (Oxford University Press, 2009).

[68] J. Daillant and A. Gibaud, *X-Ray and Neutron Reflectivity* (Springer Science & Business Media, 2009).

[69] *Http://Commons.Wikimedia.org/Wiki/File:AFM_Schematic_(en).Svg* (n.d.).

[70] K. Okimura, J. Sakai, and S. Ramanathan, J. Appl. Phys. **107**, 063503 (2010).

[71] G. Andersson, Acta. Cryst. A **10**, 623 (1956).

[72] J. Laverock, L. F. J. Piper, A. R. H. Preston, B. Chen, J. McNulty, K. E. Smith, S. Kittiwatanakul, J. W. Lu, S. A. Wolf, P. A. Glans, and J. H. Guo, Phys. Rev. B **85**, 081104(R) (2012).

[73] G. Silversmit, D. Depla, H. Poelman, G. B. Marin, and R. De Gryse, J. Electron Spectrosc. **135**, 167 (2004).

[74] G. Xu, P. Jin, M. Tazawa, and K. Yoshimura, Appl. Surf. Sci. **244**, 449 (2005).

[75] A. Kaushal and D. Kaur, J. Nanopart Res **13**, 2485 (2011).

[76] C. C. Y. Kwan, Appl. Phys. Lett. **20**, 93 (1972).

[77] H. Baumgart, *Private Communication* (n.d.).

[78] N. Sepúlveda, A. Rúa, R. Cabrera, and F. Fernández, Appl. Phys. Lett. **92**, 191913 (2008).

[79] W. Fan, J. Cao, J. Seidel, Y. Gu, J. W. Yim, C. Barrett, K. M. Yu, J. Ji, R. Ramesh, L. Q. Chen, and J. Wu, Phys. Rev. B **83**, 235102 (2011).

[80] H. L. Ma, J. Y. Yang, Y. Dai, Y. B. Zhang, B. Lu, and G. H. Ma, Appl. Surf. Sci. **253**, 7497 (2007).

[81] H.-T. Kim, B.-G. Chae, D.-H. Youn, G. Kim, K.-Y. Kang, S.-J. Lee, K. Kim, and Y.-S. Lim, Appl. Phys. Lett. **86**, 242101 (2005).

[82] K. Fuchs and N. F. Mott, Proc. Cambridge Philos. Soc. **34**, 100 (1938).

[83] J. Lu, K. G. West, and S. A. Wolf, Appl. Phys. Lett. **93**, 262107 (2008).

[84] V. Eyert, Ann. Phys. (Leipzig) **11**, 650 (2002).

[85] D. Kucharczyk and T. Niklewski, J Appl Crystallogr **12**, 370 (1979).

[86] P. F. Bongers, Solid State Commun. **3**, 275 (1965).

[87] A. S. Barker Jr, H. W. Verleur, and H. J. Guggenheim, Phys. Rev. Lett. (1966).

[88] C. R. Everhart, J. Appl. Phys. **39**, 2872 (1968).

[89] K. Kosuge, J. Phys. Soc. Jpn. **22**, 551 (1967).

[90] W. H. Rosevear and W. Paul, Phys. Rev. B **7**, 2109 (1973).

[91] D. E. Farrell, C. J. Allen, R. C. Haddon, and S. V. Chichester, Phys. Rev. B **42**, 8694(R) (1990).

[92] T. A. Friedmann, M. W. Rabin, J. Giapintzakis, J. P. Rice, and D. M. Ginsberg,

Phys. Rev. B **42**, 6217 (1990).

[93] K. Saeki, T. Wakita, Y. Muraoka, M. Hirai, T. Yokoya, R. Eguchi, and S. Shin, Phys. Rev. B **80**, 125406 (2009).

[94] M. Liu, M. Wagner, J. Zhang, A. McLeod, S. Kittiwatanakul, Z. Fei, E. Abreu, M. Goldflam, A. J. Sternbach, S. Dai, K. G. West, J. Lu, S. A. Wolf, R. D. Averitt, and D. N. Basov, Appl. Phys. Lett. **104**, 121905 (2014).

[95] S.-J. Liu, H.-W. Fang, Y.-T. Su, and J.-H. Hsieh, Jpn. J. Appl. Phys. **53**, 063201 (2014).

[96] B. Chen, D. Yang, P. A. Charpentier, and M. Zeman, Sol. Energ. Mat. Sol. C. **93**, 1550 (2009).

[97] R. D. Shannon, Acta. Cryst. A **32**, 751 (1976).

[98] Y. Ji, Y. Zhang, M. Gao, Z. Yuan, Y. Xia, C. Jin, B. Tao, C. Chen, Q. Jia, and Y. Lin, Sci. Rep. **4**, (2014).

[99] M. Marezio, D. McWhan, J. Remeika, and P. Dernier, Phys. Rev. B **5**, 2541 (1972).

[100] S. Kittiwatanakul, J. Laverock, D. Newby, K. E. Smith, S. A. Wolf, and J. Lu, J. Appl. Phys. **114**, 053703 (2013).

[101] W. Brückner, U. Gerlach, H. P. Brückner, W. Moldenhauer, and H. Oppermann, Phys. Stat. Sol. (a) **42**, 295 (1977).

[102] W. Brückner and W. Moldenhauer, Phys. Stat. Sol. (a) **38**, K17 (1976).

[103] S. O. Kasap, *Hall Effect in Semiconductors* (2001).